Fast Algorithms to simulate extremely polydisperse media

Von der Fakultät Mathematik und Physik der Universität Stuttgart
zur Erlangung der Würde eines Doktors der
Naturwissenschaften (Dr. rer. nat.) genehmigte Abhandlung

vorgelegt von

Martin Wackenhut

aus Böblingen

Hauptberichter:	Prof. Dr. Hans J. Herrmann
Mitberichter:	Prof. Dr. Hans-Rainer Trebin
Tag der mündlichen Prüfung:	28. April 2006

Institut für Computerphysik der Universität Stuttgart

2006

Contents

List of Symbols

Symbol	Meaning throughout the thesis
a	Prefactor in the power law
b	Exponent of the power law
P	Polydispersity
$\vec{F_n}$	Normal force in a contact
$\vec{F_t}$	Tangential force in a contact
$\vec{n}$	Normal vector in a contact
δ_n	Normal deformation
δ'_n	Maximal normal deformation w/o repulsive force
δ_t	Tangential deformation
μ	Friction coefficient
d_s	Saturation dilatancy
Ψ	Angle of dilatancy
α	Scaling factor for the force law
ρ_i	Initial volume fraction of the soft-particle
a_n, b_n, c_n	Fit parameter for the normal force law
$F_{t_{max}}$	Maximal tangential force
s, a_t, b_t	Fit parameter for the tangential force law
R	Size ratio of interacting particles
R_{ij}	Reduced radius between particle i and j
r_{min}	Minimal radius
r_{max}	Maximal radius
g	Factor defining the binning in the self-consistent model
q	Number of iterations in the self-consistent model

1

Zusammenfassung

Granulare Medien gehören zu den verbreitetsten Materialien in unserem täglichen Leben, und Sand ist wahrscheinlich das am meisten wahrgenommene Beispiel. Aus ihm bestehen z.B. die großen Dünenfelder in Marokko [1–5] oder aber der allseits beliebte Strand am Meer.

Trockenes Granulat besteht aus einzelnen Teilchen, deren Wechselwirkung mittels Newtons zweites Gesetz ($F = ma$) und die Coulombreibung ($F_C = \mu F_n$) beschrieben werden kann. Abhängig von der kinetischen Energie verhalten sich granulare Medien wie Feststoffe, Flüssigkeiten oder Gase. Der vakuumverpackte Kaffee z.B. ist steinhart, öffnet man aber die Packung lässt er sich leicht ausgießen. Diese Vielfalt hat drei wichtige Ursachen:

- Die Haftreibung zwischen den Teilchen
- Die einzelnen Teilchen sind keiner thermischen Bewegung unterworfen
- Die Energiedissipation während der Kollision zweier Teilchen

1.1 Polydisperse granulare Medien

Bei granularen Medien wie Weizen oder Erdnüssen sind die einzelnen Teilchen ungefähr von gleicher Größe. Anders verhält es sich für Hochleistungsbeton oder moderne Keramiken. Hier erstreckt sich die Größenverteilung typischerweise über mehrere Größenordnungen.

Das Ziel dieser Arbeit ist die Entwicklung schneller Algorithmen zur Simulation extrem polydisperser Medien. Solche Algorithmen sind von grundlegendem Interesse, um das Verhalten moderner Arbeitsmaterialien besser berechnen zu können. Beim Hochleistungsbeton z.B. ist eines der Hauptziele die Erhöhung der Packungsdichte. Hierdurch wird die Menge an Bindemittel reduziert und die Schrumpfung des Betons während des Aushärtens vermindert. Gleichzeitig reduziert sich die Wahrscheinlichkeit der Rissbildung, und der Beton wird stabiler.

Wie wichtig polydisperse Medien beim Erzeugen dichter Packungen sind, zeigt der Vergleich mit einem monodispersen Material. Füllt man einen Behälter mit gleich großen Stahlkugeln und vibriert ihn über längere Zeit, erhält man eine Dichte von 0.637 [6]. Die maximal mögliche Packungsdichte von $\pi/\sqrt{18} \approx 0.7405$ [7] erreicht man mit der kubisch flächenzentrierten Packung. Eine Packungsdichte größer als 0.74 wird also nur durch die Mischung großer und kleiner Teilchen möglich.

Eine Packungsdichte von eins erhält man z.B. mit raumfüllenden Lagern [8–10] oder der Apollonischen Packung [11]. In diesen Packungen, wie auch beim Hochleistungsbeton, ist die Teilchenverteilung durch ein abgeschnittenes Potenzgesetz gegeben:

$$p(r) = ar^{-b}; \qquad r_{min} < r < r_{max} \tag{1.1}$$

Hierbei ist r_{min} der Radius des kleinsten und r_{max} der Radius des größten Teilchens und die Polydispersität ist definiert als $P = \frac{r_{max}}{r_{min}}$. Der Vorfaktor a ist so gewählt, dass $\int_{r_{min}}^{r_{max}} p(r) = 1$ und der Exponent b ist über $b = d_f + 1$ mit der fraktalen Dimension d_f des Materials verbunden.

1.2 Übersicht

Für die Simulationen in dieser Arbeit wurde sowohl die Kontaktdynamik [12–17] als auch die Molekulardynamik [18–22] verwendet. Diese beiden Methoden unterscheiden sich in folgenden Punkten: Die Kontaktdynamik arbeitet mit unendlich harten Teilchen und einem relativ großen

Zeitschritt. Im Gegenzug sind die auf die Teilchen wirkenden Kräfte nicht kontinuierlich. Die Molekulardynamik hingegen ist eine kontinuierliche Methode und arbeitet mit elastischen Teilchen, bei denen die rücktreibende Kraft mittels des Überlappes beschrieben wird. Der Zeitschritt ist umgekehrt proportional zur Steifigkeit der Teilchen, womit die Simulation sehr harter Teilchen sehr zeitaufwendig wird.

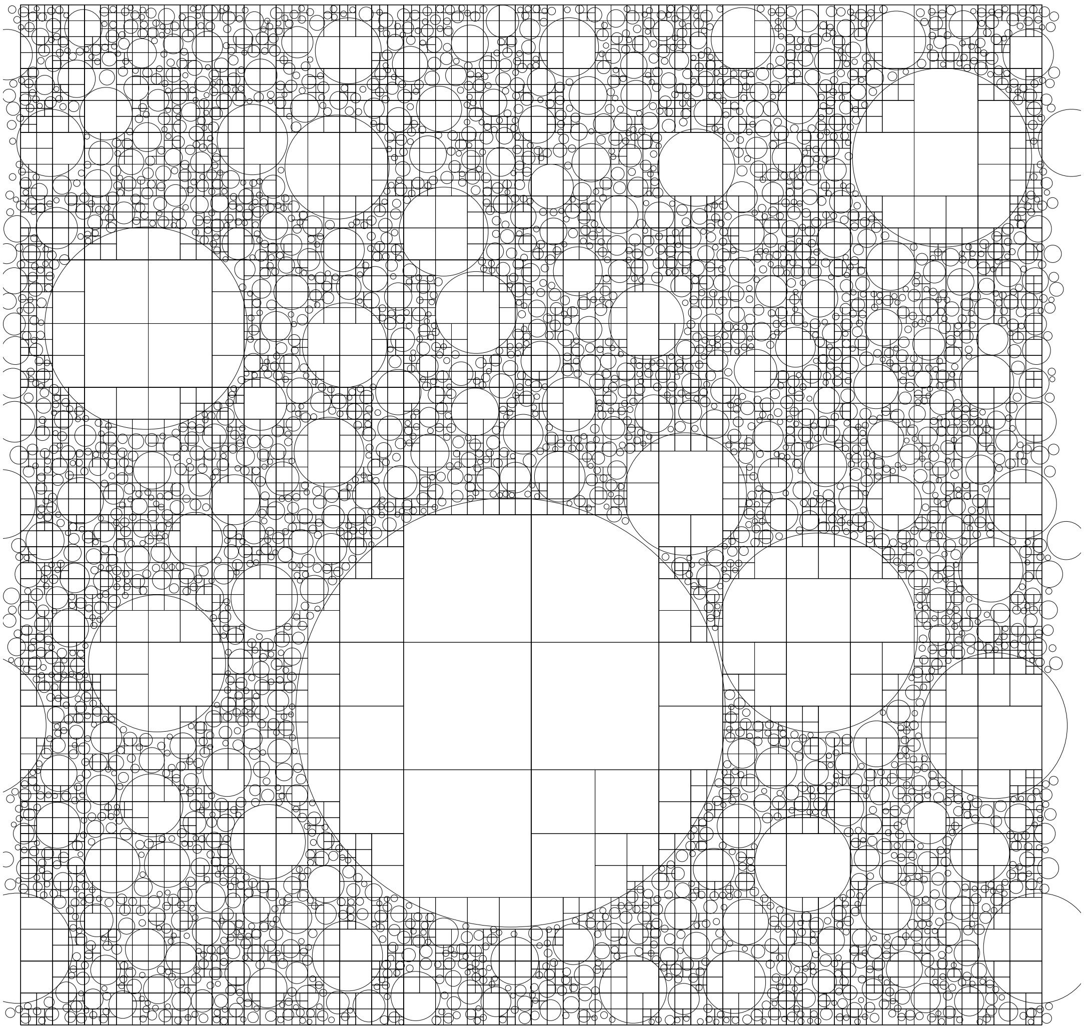

Fig. 1.1: Mittels des Quad-trees erzeugtes Gitter welches in Gebieten mit vielen kleinen Teilchen engmaschiger wird während es um große Teilchen grobmaschig bleibt.

Zur Bestimmung überlappender Kontakte wurde statt des Linked-Cell Algorithmus der Quad-tree (Abbildung 1.1) benutzt. Bei diesem wird das zu simulierende Volumen mit einem adaptiven Gitter überzogen, welches in Regionen mit vielen kleinen Teilchen engmaschiger wird, während es im Bereich großer Teilchen grobmaschig ist. Hierdurch wird die Anzahl der zu überprüfenden Kontakte stark vermindert.

1.3 Das Scherverhalten polydisperser Medien

Während des Transportes und der Verarbeitung granularer Medien gehen geschätzte 40% Energie verloren [23, 24]. Daher ist die Industrie sehr daran interessiert, ihr Wissen über das Verhalten dieser Materialien unter unterschiedlichsten Bedingungen zu erweitern.

Sehr interessant ist hierbei das Scherverhalten, da die Kraftketten, welche die externe Last tragen, aufbrechen und sich das Material zur Umlagerung ausdehnen muss, so dass Dilatanz [25] zu beobachten ist. Die Viskosität hängt hierbei sehr stark von der Größenverteilung ab. Bei bidispersen Systemen mit gegebener Packungsdichte nimmt die Viskosität in dem Maße ab, in dem das Verhältnis des großen zum kleinen Radius zunimmt [26, 27]. Ab einem Verhältnis größer als 10:1 ist kaum noch ein Einfluss einer weiteren Änderung des Verhältnisses zu beobachten. In kolloidalen bidispersen Systemen erreicht die Viskosität ein Optimum für Größenverhältnisse von zwei bis vier [28]. Eine der grundlegenden Theorien zur Beschreibung der Viskosität multimodaler Suspensionen wurde von Farris [29] entwickelt und später durch Sengun und Probstein [30] ausgebaut.

In enger Zusammenarbeit mit Herrn Dr. Distler von BASF wurde ein Modell zur Untersuchung des Einflusses von Schmiermittel auf das Scherverhalten polydisperser Materialien entwickelt. Ein Material, das ähnliche Eigenschaften zeigt wie das zu beschreibende polydisperse Material, kann durch Auflösen von Stärke in Wasser hergestellt werden. Bei hoher Stärkekonzentration verhält sich diese Mischung unter Schlag wie ein Festkörper, dreht man die Schüssel auf den Kopf, fließt die Mischung langsam heraus.

Das Schmiermittel wird durch masselose Punktteilchen beschrieben, die auf Teilchen näher als d_r eine abstoßende Kraft

$$F_r(d) = -\frac{\partial U}{\partial d} = \begin{cases} k\hat{d}^{-1}e^{-\alpha\hat{d}}(\hat{d}^{-1}+\alpha) - F_0 & 0 < \hat{d} < 1 \\ 0 & \hat{d} \geq 1 \end{cases} \tag{1.2}$$

ausüben.

Die durchgeführten Scherexperimente zeigen, dass bei gleicher Packungsdichte polydisperse Mischungen eine stärkere Dilatanz und einen größeren Scherwiderstand aufzeigen als bidisperse Systeme. Allerdings sind höhere Packungsdichten für bidisperse Systeme leichter zu erreichen. Für sehr dichte bidisperse Systeme ist das Scherverhalten vergleichbar mit dem polydisperser Systeme geringerer Packungsdichte. Die Scherkraft fällt jedoch deutlich geringer aus.

Die Zugabe von Punktteilchen beeinflusst den Scherwinkel und die Dilatanz kaum, während die Scherkraft abnimmt. Die Anzahl der Punktteilchen hat allerdings durchaus einen Einfluss, denn bei Zugabe sehr vieler Punktteilchen ist eine größere Dilatanz zu beobachten. Wird die Zahl der Punktteilchen zu groß, bilden diese ein Netzwerk, welches den Großteil der Last trägt und nach der Initialisierung zu einer starken Dilatanz führt.

1.4 Das Konzept der weichen Teilchen

Die grundlegende Schwierigkeit bei der numerischen Untersuchung polydisperser Systeme ist die nichtlineare Abhängigkeit der Rechenzeit von der Polydispersität.

Um die Anzahl der Teilchen bei der Simulation polydisperser Medien zu reduzieren, wurde das Konzept der weichen Teilchen eingeführt. Hierbei werden viele kleine Teilchen, die sich in einer polydispersen Packung zwischen den größeren befinden, durch eine makroskopische Beschreibung ersetzt. Hierdurch wird die Rechenzeit stark verringert, da nur eine kleine Anzahl weicher Teilchen anstelle der vielen kleinen Teilchen in der Simulation berücksichtigt werden muss.

Ein weiches Teilchen besteht aus einer kugelförmigen Hülle, in welcher sich eine polydisperse Packung befindet. Die Initialisierung erfolgt mittels eines hierarchischen Algorithmus, so dass die erzeugte Packung einem abgeschnittenen Potenzgesetz (Gleichung 1.1) mit dem Exponenten $b = 3.5$ gehorcht. Dies ist der selbe Wert wie für Hochleistungsbeton. Die eingefügten Teilchen werden im Folgenden als „Körner" bezeichnet.

Um diese Teilchen in einer Molekulardynamik verwenden zu können, wird mittels der in Abbildung 1.2 dargestellten Messmethode deren konstitutives Gesetz bestimmt.

Das linke Bild zeigt die Interaktion eines weichen Teilchens mit einem Teilchen gleicher Größe, welches durch das Hertzsche Gesetz beschrieben wird. Im Folgenden wird so ein Teilchen als „solide" bezeichnet. Im mittleren Teil ist die Wechselwirkung zweier weichen Teilchen dargestellt. Wie im rechten Teil gezeigt, wird für die Normalmessung eine vorgegebene Normalverformung δ_n verursacht, und nachdem das System relaxiert ist, wird die rücktreibende Kraft F_n gemessen. Bei der Tangen-

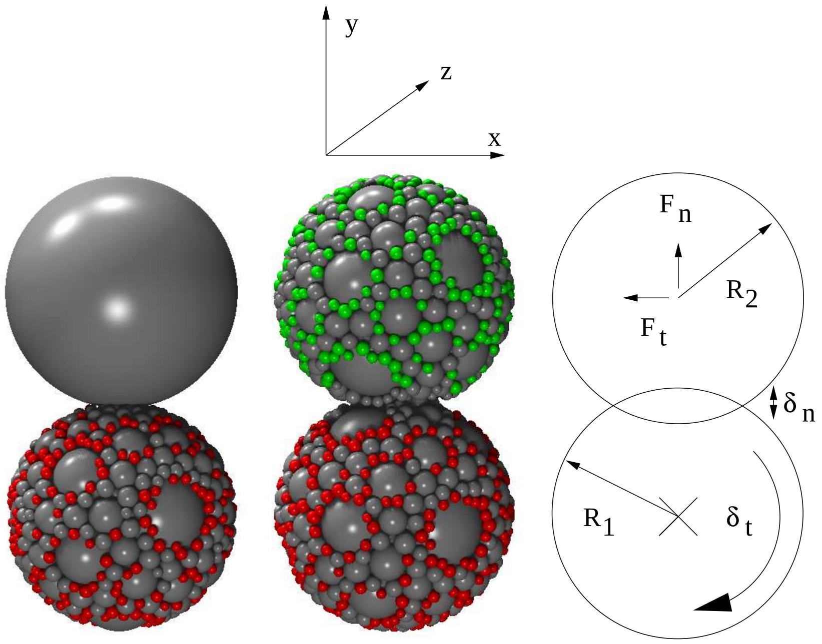

Fig. 1.2: Messung des konstitutiven Gesetzes der weichen Teilchen. Links die Messung für ein weiches Teilchen mit einem soliden Teilchen gleicher Größe und rechts die Wechselwirkung zweier weicher Teilchen. Zur Messung des tangentialen Gesetzes werden die roten Teilchen um den Kugelmittelpunkt gedreht. Die grünen Teilchen hingegen verhindern ein ungewolltes Rotieren der Körner im zweiten weichen Teilchen.

tialmessung wird eine Tangentialdeformation $\delta_t = R_1\gamma$ durch die Rotation der kleinsten äußeren Körner um den Winkel γ um den Teilchenmittelpunkt hervorgerufen und nach der Relaxation die Tangentialkraft gemessen.

Das gemessene Kraftgesetz in Normalrichtung wird beschrieben durch

$$F(\delta_n) = \begin{cases} 0, & 0 < \delta_n < \delta_n' \\ \alpha(a_n \delta_n^{b_n} + c_n), & \delta_n \geq \delta_n' \end{cases} . \tag{1.3}$$

Die Normalverformung ist durch δ_n gegeben, δ_n' ist die Verformung bis zu der man keine rücktreibende Kraft misst und a_n, b_n und c_n sind Fitparameter, die für beide Kontakte unterschiedlich sind. Der Vorfaktor

$$\alpha = \left(\frac{R_{12}'}{R_{12}} \right) \tag{1.4}$$

skaliert das Kraftgesetz vom gemessenen System in ein System beliebiger Größe. $R_{12} = \frac{R_1 R_2}{R_1 + R_2}$ beschreibt den reduzierten Radius während der Messung und R_{12}' denjenigen des skalierten Systems.

Das tangentiale Kraftgesetz

$$F_t(\delta_n, \delta_t) = F_{t_{max}}(\delta_n) \cdot \tanh(s\delta_t) \tag{1.5}$$

hängt sowohl von der Normalverformung δ_n als auch von der Tangentialverformung δ_t ab. Der Parameter s ist eine Konstante und

$$F_{t_{max}}(\delta_n) = \begin{cases} 0, & 0 < \delta_n < \delta'_n \\ \alpha(a_t\delta_n^{b_t} + a_t\delta_n'^{b_t}), & \delta_n \geq \delta'_n \end{cases} \tag{1.6}$$

beschreibt die maximale Tangentialkraft, bei welcher der Kontakt gerade nicht gleitet. Die Steigung $F_{t_{max}}s$ um den Nullpunkt beschreibt die Steifigkeit der Tangentialfeder.

Ein dreidimensionales Scherexperiment mit normalen und weichen Teilchen zeigt, dass durch dieses Konzept die Polydispersität um den Faktor 10 erweitert werden kann. Mittels der weichen Teilchen wird die zu simulierende Teilchenanzahl um den Faktor 28 reduziert und gleichzeitig kann ein fünf mal größerer Zeitschritt gewählt werden. Somit reduziert sich der Rechenaufwand um mehr als den Faktor 100.

1.5 Das selbstkonsistente Modell

Mit dem Modell der weichen Teilchen kann die Rechenzeit für die Simulation eines polydispersen Systems zwar reduziert werden, allerdings bleibt die Abhängigkeit der Rechenzeit von der Polydispersität erhalten. Durch die Erweiterung des Konzepts der weichen Teilchen zu einem selbstkonsistenten Modell wird es möglich, die Rechenzeit von der Polydispersität abzukoppeln.

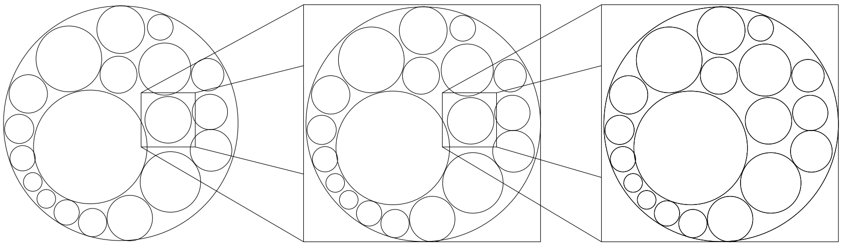

Fig. 1.3: Schematische Darstellung des selbstkonsistenten Modells. Das weiche Teilchen ist mit Körnern und weichen Teilchen gefüllt. Vergrößert man ein solches weiches Teilchen, so findet man eine ähnliche Konfiguration aus Körnern und weichen Teilchen vor.

Abbildung 1.3 zeigt eine schematische Darstellung des selbstkonsistenten Modells, welches die fraktale Natur polydisperser Medien nutzt. Vergrößert man eine lokale Packung in einem polydispersen System, so findet man in dieser wiederum kleinere lokale Packungen. Das selbstkonsistente weiche Teilchen ist mit Körnern und zusätzlich mit kleinen weichen Teilchen gefüllt. Vergrößert man ein solches kleines weiches Teilchen, findet man eine ähnliche Konfiguration aus Körnern und kleinen weichen Teilchen vor.

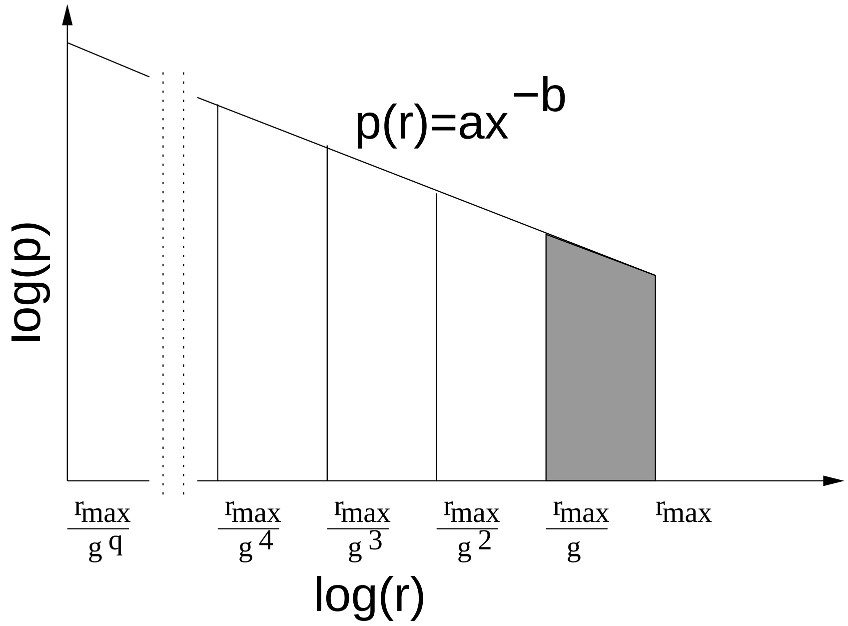

Fig. 1.4: Die Teilchenverteilung des selbstkonsistenten weichen Teilchens nach q Iterationen gehorcht einem abgeschnittenen Potenzgesetz. Der Faktor g definiert die Aufteilung des Potenzgesetzes und durch jede Iteration wird die Teilchenverteilung, die von dem gemessenen Kraftgesetz beschrieben wird, um einen Abschnitt erweitert.

Die Bestimmung des Kraftgetzes erfolgt in einem iterativen Prozess aus q Schritten. Die Teilchengrößenverteilung des so bestimmten Kraftgesetzes ist in Abbildung 1.4 dargestellt und erstreckt sich von r_{max}/g^q bis r_{max} und die Polydispersität ist durch $P = g^g$ gegeben. Der Faktor g bestimmt, wie sehr die beschriebene Teilchenverteilung bei einer Iteration erweitert wird. Außerdem ist die Anzahl der eingefügten kleinen weichen Teilchen unabhängig von der Polydispersität. Dadurch ist es möglich, Systeme unterschiedlicher Polydispersität mit derselben Anzahl Teilchen zu beschreiben.

Für die Implementierung dieses Modells muss das Kraftgesetz unabhängig von der Dichte der weichen Teilchen sein. Dies wird erreicht, wenn man selbiges in Abhängigkeit des Interaktionsvolumens beschreibt. Mit dieser Darstellung zeigt sich, dass die rücktreibende Kraft unabhängig von der Geometrie ist. Man ist also nicht auf eine kugelförmige Implementierung der selbstkonsistenten weichen Teilchen angewiesen. Zur Bestimmung der aktuellen Dichte und des Interaktionsvolumens wurde ein Algorithmus ähnlich dem iterativen Algorithmus in der Kontaktdynamik entwickelt.

1.6 Ausblick

In dieser Arbeit wurden verschiedene Algorithmen zur Simulation extrem polydisperser Systeme entwickelt, bei denen die Teilchenverteilung durch ein abgeschnittenes Potenzgesetz beschrieben wird. Die grundlegende Schwierigkeit bei der Simulation solcher Systeme liegt darin begründet, dass die Rechenzeit nichtlinear von der Polydispersität abhängt. Dies wird zum einen durch den enormen Teilchenzuwachs im Vergleich mit einem monodispersen System gleichen Volumens verursacht, aber auch durch die lineare Abhängigkeit des Zeitschrittes von der Größe des kleinsten Teilchens.

Zur Bestimmung überlappender Kontakte wurde statt des Linked-Cell Algorithmus der sogenannte Quad-tree verwendet, welcher mit einer variablen Zellgröße arbeitet. Für polydisperse Systeme wird somit die Anzahl der zu überprüfenden Kontakte stark reduziert.

Zusätzlich konnte durch das Modell der selbstkonsistenten weichen Teilchen die Anzahl der zu simulierenden Teilchen von der Polydispersität abgekoppelt werden. Mit diesem Modell ist es also möglich Systeme unterschiedlicher Polydispersität mit einer gleichbleibenden Anzahl Teilchen zu beschreiben. Außerdem ist die Darstellung des Kraftgesetzes in Abhängigkeit vom Interaktionsvolumen unabhängig von der Geometrie des Kontaktes und der Form der weichen Teilchen.

Die entwickelten Algorithmen sind ein wichtiger Schritt zu einem besseren Verständnis extrem polydisperser Medien und deren Anwendungen. Von grosser Bedeutung ist die Möglichkeit ein System beliebiger Polydispersität mit einer endlichen Anzahl von Teilchen zu simulieren. Dies erlaubt z.B. die Untersuchung unterschiedlicher Mischtechniken, um eine höhere Packungsdichte bei der Herstellung von Hochleistungsbeton zu ermöglichen.

2

Introduction

Granular media are among the most abundant materials in our life. The probably most perceived example is sand which is found on beautiful beaches or in large dune fields [1–5] like in Morocco.

Dry granular materials are composed of individual particles whose interaction can be described with Newton's second law ($F = ma$) and the Coulomb friction ($F_C = \mu F_n$). Their behavior can be described as a solid, liquid or gas. This is caused by three important conditions:

- The existence of static friction
- The particles are not subject to thermal induced motion
- The damping between colliding particles

Despite their seeming simplicity, granular media are very complex and present a wide variety of interesting physical phenomena which have been of interest for more than a century. They attracted scientists like Coulomb, who proposed the idea of static friction [31–33] or Reynolds who introduced the concept of dilatancy [25]. The effect of dilatancy can easily be observed when walking on the wet beach. Due to the pressure exerted by our feet the sand expands and the water flows into the created voids which causes the sand around our feet to become dry. In the following, a short overview over the wide variety of observable phenomena for granular materials is given. A more detailed description can be found in the literature [34–36].

Granular materials under strong vertical vibration are referred to as granular gas [37,38]. Contrary to the behaviour of a normal gas, one observes the formation of clusters [39,40], a non-Gaussian nature of the velocity distribution [41,42] and standing wave patterns [43,44]. Another common phenomenon in a granular medium under vibration is the segregation of different particle sizes [45–47]. This can be useful when separating materials but needs to be suppressed when a homogeneous mixture of granular media, for example in the pharmaceutical industry, is desired.

A good example for the solid state is vacuum sealed coffee which is hard as a brick. In this state force chains, carrying most of the external load, form and the particles neighbored to these force chains might feel almost no force. These force chains play an important role for granular media in a silo. Due to the static friction the particles at the wall support themselves and the height-dependent pressure head, typical for fluids, is absent. Therefore the pressure at the base of the silo approaches a finite value as described by Janssen [48] and, in principal, silos of arbitrary height can be build.

The outflow of material at the bottom of a silo is similar to the behavior of sand in an hourglass. Here, two glass bowls are connected by a narrow orifice and the fine sand contained in the upper bowl flows into the lower one. The Janssen-effect keeps the flow rate almost constant which allows the measurement of elapsed time. Unlike a fluid, the down falling sand does not uniformly cover the floor but forms a heap with a slope smaller than the angle of repose θ_r as for angles greater than θ_r the top layers of sand freely flow downhill [49–53].

The industry relying on the processing of granular materials is very interested in improving the understanding of these materials under different conditions. Even a small improvement can significantly decrease the cost for processing as can be seen for the transport of granular media. Here very different methods like conveyor belts or plug-flow [54–56] are used and problems related to the energy loss and momentum transfer during the particle interaction or the contact with the boundaries lead to an estimated 40% waste of energy [23,24].

2.1 Polydisperse granular media

In this work we focus on extremely polydisperse media where the size distribution can cover several orders of magnitude.

One example for these materials is the so-called high performance concrete. Here people are mainly interested in the creation of a denser packing of the material. This reduces the consumption of filler and thus shrinkage of the concrete during the drying process is minimized. As a consequence the probability for crack building is reduced and, compared with standard concrete, the material can withstand more stress. The importance of polydispersity for the generation of a dense packing shows the comparison with a monodisperse system. Pouring ball bearings in a container and vibrating the system for a sufficient long time, one obtains a random close packing with an approximate volume fraction of 0.637 [6]. The maximum possible volume fraction of $\pi/\sqrt{18} \approx 0.7405$ [7] is achieved with the face centered cubic packing. Therefore, a volume fraction higher than 0.74 can only be achieved with a mixture of large and small particles.

In two dimensions Herrmann et al. completely filled space with space-filling bearings [8–10] which were introduced as a simple model for the seismic gaps of geological faults [57–59]. These faults do not experience any large thrust over long periods of time and it is assumed that the space between the tectonic plates is filled with more or less round particles which, as the plates move, may roll on each other resulting in the spontaneous formation of local bearings and reducing the amount of friction and dissipation of energy. The medium which fills the gap between the plates is referred to as gauge and the spontaneous formation of bearings has been shown to be possible in simulations of shear bands [60]. How to completely fill three dimensional space was studied by Peickert [11] and Mahmoodi et al. [61–66] while the latter also proved the existence of a three dimensional space-filling bearing.

The size distribution of space-filling bearings, Apollonian packings, seismic gaps and high performance concrete follows a power law where the exponent b is related to the fractal dimension d_f via $b = d_f + 1$.

2.2 Simulating polydisperse granular media

Unlike in an experiment it is relatively easy to trace particles in a computer model where the material is simulated on the individual grain level. For every point in time, position and velocity of every particle is given which allows the study of velocity distributions or force chains. Well known numerical methods are the molecular dynamics [18–22], contact dynamics [12–17] and the event driven [18, 19, 67, 68] method. Other methods are Monte Carlo simulations like the random sequential adsorption (RSA) [69–77]. Using the reversible polydisperse parking lot model [78, 79] we analyzed the dynamic behaviour of one dimensional polydisperse systems where we could show that the density of the system depends on the exponent in the power law.

The biggest constraint for the numerical study of polydisperse systems is the nonlinear dependence of the computing time on the polydispersity which is discussed in more detail in chapter 3. The goal of this work is to develop fast algorithms for the simulation of extremely polydisperse media which decouple the computing time from the polydispersity.

2.3 Overview

The present work is organized in the following way: In chapter 3, a detailed overview over the effects of the polydispersity on numerical methods is given while chapter 4 describes the molecular dynamics and contact dynamics we used for our simulations. In chapter 5, a two dimensional shear experiment with polydisperse media is explained. This work was done in close collaboration with Dr. Distler from BASF.

The concept of soft-particles, which macroscopically describe the be–haviour of a polydisperse packing is introduced in chapter 6. Using this model in the shear experiment of chapter 7, we were able to reduce the computation time by more than a factor 100. In chapter 8 this idea is extended to the model of the self-consistent soft-particles which allows the simulation of granular media of any polydispersity. Using the fractal nature of polydisperse media the macroscopic description is determined in an iterative process. We close with a conclusion and outlook in chapter 9.

3

Polydispersity

In this chapter we investigate polydisperse materials in more detail. First some basic definitions and examples for polydisperse media are given. In the second part the influence of the polydispersity on the simulation of these materials is discussed.

3.1 Definitions and examples

Ideal examples of polydisperse media are so-called space-filling bearings [8–10]. Here the packing completely fills the two or three dimensional space and the particles in the packing can roll without frustration. Another example is the Apollonian packing, named after Apollonius of Perga, which is shown in Figure 3.1. In two dimensions one places three circles of the same radius such that each one is tangent to the other two. There exist two non intersecting circles touching these three. One encloses the three circles, the other one fits between them. Recursively filling the remaining voids completely covers space if the size of the smallest particle goes to zero.

Clearly this mathematical problem of completely filling space is different from the practical problem of packing. A volume fraction of unity is not achieved in reality where the smaller particles cannot be placed

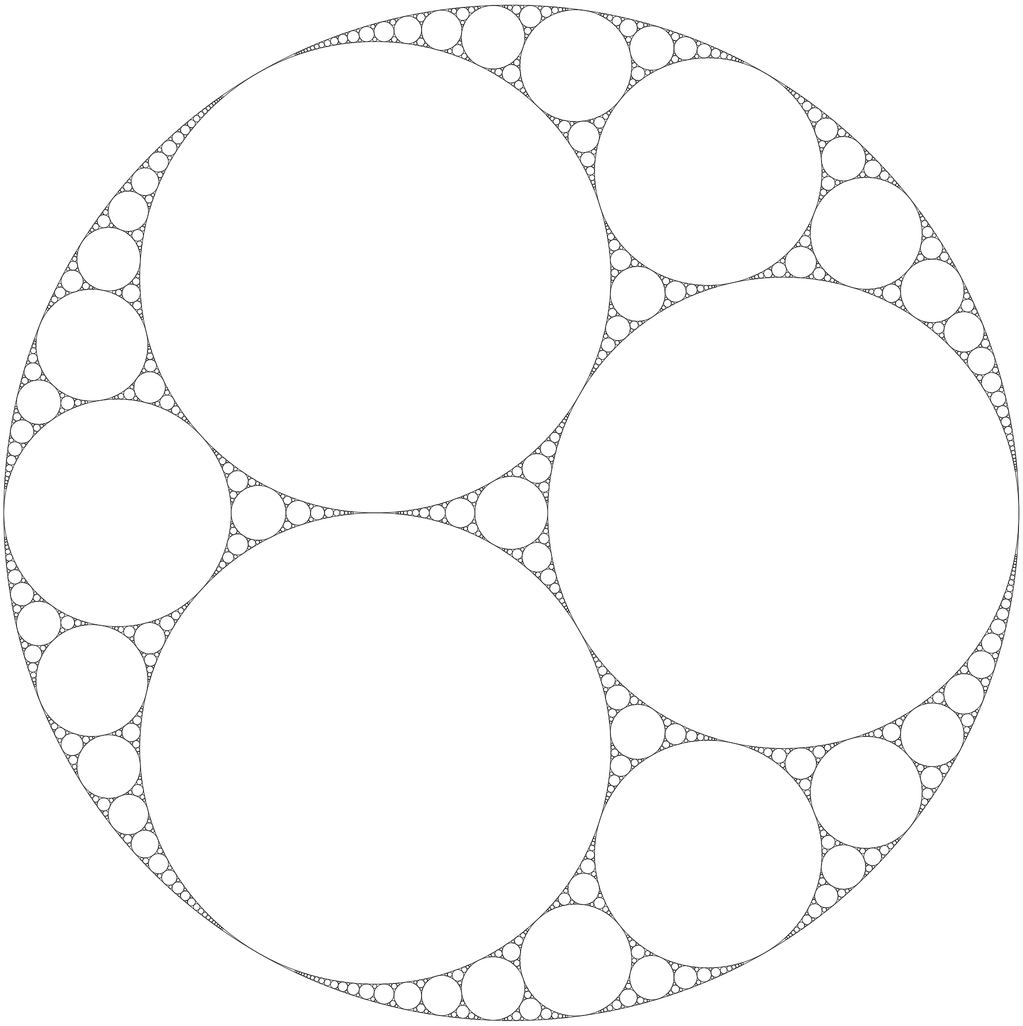

Fig. 3.1: Apollonian packing in two dimensions which reaches a volume fraction of unity if the size of the smallest particle goes to zero.

in the voids of a three dimensional packing without moving some particles and destroying the existing configuration. Nevertheless polydisperse materials are of great practical importance. One example is the so-called high performance concrete (HPC). Here people are interested to produce three dimensional packings of highest density which will reduce shrinking and crack appearance during the hardening and increase the strength of the concrete.

Figure 3.2 schematically displays the size distribution of HPC. Shown are the individual size distributions of the different components, from gravel down to silica fume. The overall distribution ranges over four magnitudes and can, as for space-filling bearings, be described by a truncated power law

$$p(r) = ar^{-b}, \qquad r_{min} < r < r_{max}. \tag{3.1}$$

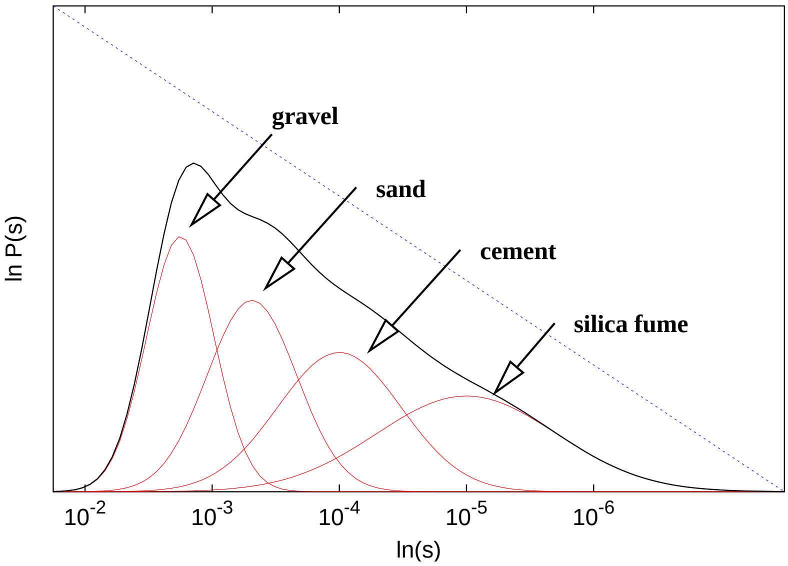

Fig. 3.2: Schematic plot of the size distribution in HPC. Shown are the individual size distributions of the different components ranging from gravel down to silica fume. The distribution ranges over four magnitudes and can be described by the truncated power law in equation 3.1, which is displayed as a straight line. The exponent b, like for space-filling bearings, is approximately 3.5.

Here r is the particle radius ranging from the smallest radius r_{min} to the largest one r_{max}. In the case of the space-filling bearings r_{min} goes to zero. The prefactor a is chosen such that $\int_{r_{min}}^{r_{max}} p(r) = 1$ and the exponent b is related to the fractal dimension d_f by $b = d_f + 1$. For the three dimensional packings shown in [8, 11] the exponent is $b \approx 3.5$, as for HPC.

Thus polydisperse media are materials with a quasi-continuous size distribution and the polydispersity

$$P = \frac{r_{max}}{r_{min}} \tag{3.2}$$

is defined as the ratio between the largest r_{max} and the smallest r_{min} particle.

3.2 Influence onto the computing time in the discrete element method

In this section we show that the computing time for the simulation of extremely polydisperse media rises proportional to P^b. We will also show that compared with a monodisperse system, a polydispersity of 10 increases the computing time by about a factor 1000.

The polydispersity has two main effects on the simulation: the increase in the particle number and the decrease of the time step. To quantify these effects a polydisperse system with r_{min} and r_{max} is compared with a monodisperse one where all particles have the same size r_{max}.

To investigate the increase in the particle number the particle volume

$$V = \sum_{i=0}^{n} \frac{4}{3}\pi r_i^3 \tag{3.3}$$

is defined and set to be equal for both systems. Here n is the number of simulated particles and r_i the radius of the ith particle.

Using this volume, the number of particles N_m in the monodisperse system is given by

$$N_m = \frac{V}{\frac{4}{3}\pi r_{max}^3}. \tag{3.4}$$

For the polydisperse system the sum in equation 3.3 becomes the integral over the product of particle radius and the number of particles of that size. This is given by a power law where the prefactor a is chosen such that $N_p = \int_{r_{min}}^{r_{max}} ar^{-b}$ where N_p is the total number of particles. Thus one can write

$$V = \int_{r_{min}}^{r_{max}} ar^{-b} \quad \frac{4}{3}\pi r^3 \quad dr. \tag{3.5}$$

Using $r_{min} = \frac{r_{max}}{P}$ one gets

$$a = \frac{(4-b)V}{\frac{4}{3}\pi {r_{max}}^{4-b}(1-P^{b-4})}, \qquad b \neq 4, \tag{3.6}$$

and the number of particles in the polydisperse system is given by

$$N_p = a \int_{r_{min}}^{r_{max}} r^{-b} dr = \frac{a}{1-b} {r_{max}}^{1-b}(1-P^{b-1}), \qquad b \neq 4. \tag{3.7}$$

Inserting a from above one gets

$$N_p = \frac{(4-b)V(1-P^{b-1})}{(1-b)\frac{4}{3}\pi {r_{max}}^3(1-P^{b-4})}, \qquad b \neq 1,4 \tag{3.8}$$

and comparing the number of particles of both systems one gets:

$$\frac{N_p}{N_m} = \frac{4-b}{1-b}\,\frac{1-P^{b-1}}{1-P^{b-4}} \qquad b \neq 1,4; P > 1 \tag{3.9}$$

The second effect is the decrease of the time step. As shown in chapter 4, the time step Δt for the Hook-law as well as the Hertz-law is proportional to the size of the smallest particle and the ratio between the time step Δt_p of a polydisperse and Δt_m of a monodisperse system is

$$\frac{\Delta t_p}{\Delta t_m} \sim \frac{r_{min}}{r_{max}} = \frac{1}{P}. \tag{3.10}$$

Combining the increase of the number of particles and the decrease of the time step for large polydispersities ($P \gg 1$) the relative increase in computing time is

$$\frac{t_p}{t_m} = \frac{N_p}{N_m} * \frac{\Delta t_m}{\Delta t_p} \approx \frac{4-b}{b-1} P^b. \tag{3.11}$$

Here t_p is the computation time for the polydisperse system and t_m for the monodisperse one. Care has to be taken with the second term as the computing time is inverse proportional to the time step. This formula is only valid for a polydispersity P greater than unity as for $P = 1$ the particle volume in equation 3.5 becomes zero. Additionally b must not be larger than 4 as the fractal dimension of a three dimensional packing would become larger than the real dimension. An exponent $b \leq 1$ would mean that in the polydisperse system one would have more large particles than small ones. This would make it impossible to densely fill space. Thus all the special cases omitted during integration and for which the derived formula is incorrect are of no interest for our considerations.

In Figure 3.3 the ratios $\frac{N_p}{N_m}$ and $\frac{t_p}{t_m}$ are plotted as a function of the polydispersity P. The exponent in the power law was set to $b = 3.5$ and even a relatively small polydispersity of $P = 10$ increases the computing time by roughly a factor of 1000.

In general the increase in computing time might be even worse as the increase of contacts in the linked-cell algorithm for a polydisperse system was not considered. A solution is given by the quad-tree presented in chapter 4.

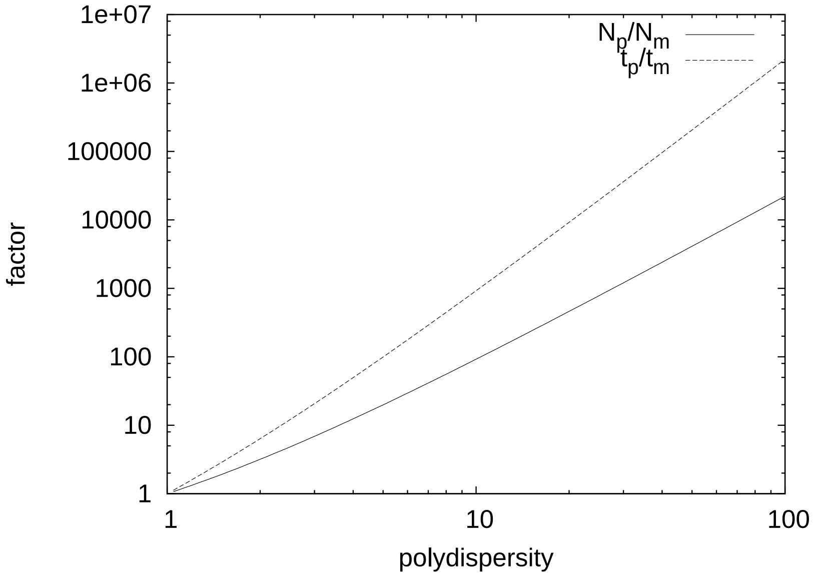

Fig. 3.3: The effects of polydispersity in discrete element methods. Plotted is the relative increase of particles N_p/N_m and the relative increase of computing time t_p/t_m as a function of the polydispersity. Increasing the polydispersity by a factor of 10 results in a 1000 times larger computing time.

3.2.1 Summary

As a summary we can say that compared with a monodisperse system occupying the same volume, the computing time for a polydisperse system rises proportional to P^b. The main reason is the increase of the number of particles but the linear dependence of the time step onto the polydispersity needs also to be taken into account.

4

Simulation method

Granular media show a wide variety of behavior. They can be described as a solid, a fluid or even a gas. The sand we walk on can be describe as a solid while a debris avalanche is behaving like a fluid. Before the invention of the computer the behavior of granular media was described by continuum mechanics where the, in general heterogeneous, micro structure of the material is ignored. Thus the method does not give any information about the forces, position or velocity of the individual particle, making it impossible to study force networks and velocity distributions. Here the discrete element method is filling the gap. This numerical method computes the trajectory of every single particle by calculating the interaction between colliding particles and solving Newton's equation for the individual particle. There exist three well known models, the event driven method [18,19,67,68], molecular dynamics [18–22] and contact dynamics [12–17].

In this work we used the latter two, and in the following the principles of both methods and our adaptions to simulate very polydisperse systems are explained.

In general one has to solve Newton's equation

$$\vec{F}_i = m_i \ddot{\vec{x}}_i; \qquad \vec{M}_i = \left(\frac{d(\bar{J}_i \dot{\vec{\phi}}_i)}{dt}\right)_b + \dot{\vec{\phi}}_i \times \bar{J}_i \dot{\vec{\phi}}_i = \left(\frac{d(\bar{J}_i \dot{\vec{\phi}}_i)}{dt}\right)_s \overbrace{= \bar{J}_i \ddot{\vec{\phi}}_i}^{\text{spherical}} . \tag{4.1}$$

Here m_i is the mass of the ith particle, $\ddot{\vec{x}}_i$ its acceleration, $\bar{J}_i$ its inertial tensor, $\dot{\vec{\phi}}_i$ the angular velocity and $\ddot{\vec{\phi}}_i$ the angular acceleration. In the second equation the term with the subscript b describes the rotational motion in the body frame while the term with the subscript s describes it in the space frame. For homogeneous spherical particles the intertial tensor stays constant and its time derivative becomes zero.

In a granular assembly the force $\vec{F}_i$ felt by a single particle can be split up into external forces and the interaction forces between the particle and its nearest neighbors

$$\vec{F}_i = m\ddot{\vec{x}}_i = \sum_j \vec{F}_{ij} + \vec{F}_{ext}. \tag{4.2}$$

Here $\vec{F}_{ij}$ describes the interaction force between particle i and particle j, while $\vec{F}_{ext}$ depicts any external force, like gravity, acting onto the individual particle. For a dry and non-cohesive granular medium composed of grains of a macroscopic size the grain-grain interaction can be described through repulsion (the normal force), friction (tangential force) and damping,

$$\vec{F}_{ij} = \vec{F}_n + \vec{F}_t + \vec{F}_d. \tag{4.3}$$

The tangential component $\vec{F}_t$ of the interaction force gives rise to a torque $M_{ij} = \vec{r}_i \times \vec{F}_t$ where the vector $\vec{r}_i$ points from the center of particle i to the contact point at which the frictional force is applied. Therefore the second part of equation 4.1 can be written as

$$\vec{M}_i = \sum_j \vec{M}_{ij} = \sum_j \vec{r}_i \times \vec{F}_t, \tag{4.4}$$

with the individual moments $\vec{M}_{ij}$ exerted onto particle i through the contact with particle j.

4.1 Molecular Dynamics

Molecular Dynamics (MD) is the oldest of the three discrete element methods mentioned above. The interacting forces between the particles are described by an interacting potential where the overlap between two particles is interpreted as deformation which results in a repulsive force.

4.1.1 The particle-particle contact

The interacting forces are calculated by determining the forces present at the two particle contacts. A general picture of such a contact between particle i and j is shown in Figure 4.1.

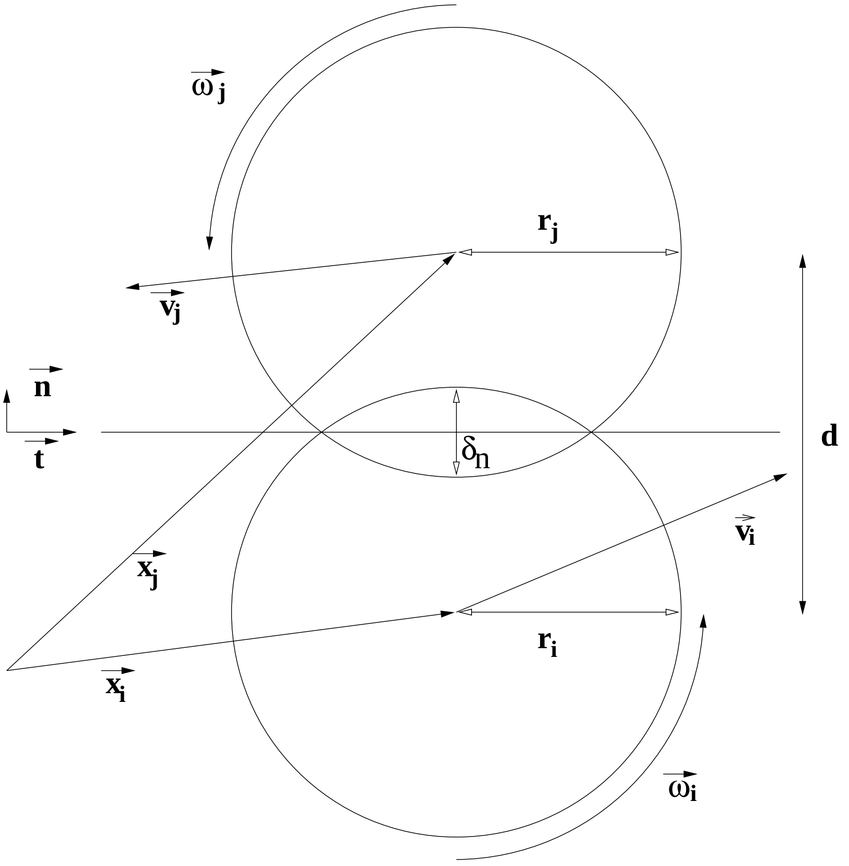

Fig. 4.1: Schematic picture of the particle-particle contact of particle i and j.

Before dealing with the details of MD the different variables of the particle-particle contact shown in Figure 4.1 are defined.

- The normal vector $\vec{n}$:

The normal vector points from the center of particle i to the center of particle j and is given by

$$\vec{n} = \frac{\vec{x}_j - \vec{x}_i}{|\vec{x}_j - \vec{x}_i|}. \tag{4.5}$$

- The relative velocity $\vec{v}_{rel}$:

  This velocity describes how particle j moves in respect to particle i and is given by

  $$\vec{v}_{rel} = \vec{v_j} - \vec{v_i}. \tag{4.6}$$

- The relative surface velocity $\vec{v}_s$:

  This is the velocity of the surface of particle j relative to the surface of particle i. It consists of the tangential part of the relative velocity and the movement due to rotation.

  $$\vec{v}_s = \vec{v}_{rel} - (\vec{v}_{rel} \cdot \vec{n})\vec{n} - \vec{n} \times (r_i\vec{\omega_i} + r_j\vec{\omega_j}) \tag{4.7}$$

- The tangential vector $\vec{t}$:

  This vector of unit length points in the direction of the relative surface velocity and lies in the plane perpendicular to the normal vector.

- The overlap or normal deformation δ_n:

  In molecular dynamics the deformation during the particle contact is modeled by the overlap

  $$\delta_n = r_i + r_j - |\vec{x_j} - \vec{x_i}| = r_i + r_j - d, \tag{4.8}$$

  which can be considered as the elongation of a spring connected between the interacting particles.

- The reduced mass m_{ij} :

  $$m_{ij} = \frac{m_i m_j}{m_i + m_j} \tag{4.9}$$

- The reduced radius R_{ij}:

  $$R_{ij} = \frac{R_i R_j}{R_i + R_j} \tag{4.10}$$

  Note that a wall can be described as a sphere with an infinite radius. Therefore the reduced radius of a particle wall contact becomes $R_{i,wall} = \lim_{R_j \to \infty} \frac{R_i R_j}{R_i + R_j} = R_i$.

4.1.2 Modeling the normal force

The repulsive normal force $\vec{F}_n$ between interacting particles depends on the spring constant k_n and the normal deformation δ_n and is given by

$$\vec{F}_n = -k_n \delta_n \vec{n}. \tag{4.11}$$

The spring constant k_n depends on the radius and the material properties of the two interacting particles. In the Hook-law the spring constant is given by $k_n = \frac{2R_{ij}}{D_n}$ with the material dependent constant

$$D_n = \frac{3}{4}(\frac{1-\nu_i^2}{E_i} + \frac{1-\nu_j^2}{E_j}). \tag{4.12}$$

Here ν is the Poisson-ratio and E is the elastic modulus of the particle as described in continuum mechanics. For spherical particles the repulsive force in general is not linear as the contact area increases nonlinear with the normal deformation as described by H. Hertz [80, 81]. In the Hertz-law the spring constant becomes $k_n = \sqrt{R_{ij}\delta_n}/D_n$, the repulsive force is given by

$$\vec{F}_n = -\frac{\sqrt{R_{ij}}\delta^{3/2}}{D_n}\vec{n} \tag{4.13}$$

and the potential energy U stored in such a contact is

$$U = \frac{2\delta_n^{5/2}}{5D_n}\sqrt{R_{ij}}. \tag{4.14}$$

In a more general form, the Hook-law and the Hertz-law can be written as

$$\vec{F}_n = \frac{2R_{ij}}{D_n}\left(\frac{\delta_n}{4R_{ij}}\right)^{1+\theta}\vec{n}. \tag{4.15}$$

For $\theta = 0$ one gets the Hook-law, for $\theta = 0.5$ the Hertz-law. A more detailed discussion is given by Stefan Luding [82].

4.1.2.1 Dissipation of energy

During the collision of two particles a certain fraction of the kinetic energy will be dissipated due to the transformation into heat. This behavior is modeled by the introduction of a velocity dependent damping force $\vec{F}_d$ for which the normal part is given by

$$\vec{F}_{d_n} = \eta_n(\vec{v}_{rel} \cdot \vec{n})\vec{n}. \tag{4.16}$$

This force is proportional to the normal part of the relative velocity and points into the opposite direction of the repulsive normal force. Thus it slows down the two interacting particles. For a fast relaxation in the simulation the damping coefficient is calculated with

$$\eta_n = 2\sqrt{m_{ij}k_n}, \tag{4.17}$$

as proposed by Cundall and Strack [21]. This corresponds to the critical damping of an harmonic oscillator with the mass m_{ij} and the spring constant k_n. Tsuji et al. [83] relate the damping coefficient to the restitution coefficient e which is the ratio between the velocity after and before the collision and can be measured in a simple experiment. They get

$$\eta_n = \theta\sqrt{m_{ij}k_n}\delta_n^{1/4} \tag{4.18}$$

where the constant θ is an empirical constant related to the restitution coefficient e as described in [83].

For particles separating with high velocities the viscous damping force inverts the repulsive force. This leads to an attractive instead of a repulsive force between the two particles. In such a case the acting force is set to zero.

4.1.3 Modeling the tangential force

The tangential part of the interaction force is a result of the inter particle friction and can be described by the Coulomb law

$$|\vec{F}_t| = -\mu|\vec{F}_n|\vec{t}. \tag{4.19}$$

The friction coefficient μ takes different values depending on the type of friction.

$$|\vec{F}_s| \leq \mu_s|\vec{F}_n| \qquad v_s = 0 \tag{4.20}$$

$$|\vec{F}_d| = \mu_d|\vec{F}_n| \qquad v_s \neq 0 \tag{4.21}$$

Here v_s is the value of the relative surface velocity while μ_s and μ_d are the coefficients of static and dynamic friction which in many publications are assumed to be equal. In the simplest implementation the frictional force is described as a viscous force

$$\vec{F}_t = -\mu_d |\vec{F}_n| \vec{v}_s. \tag{4.22}$$

This force reduces the relative surface velocity over time. But due to the discrete time step, it will, when the surface velocity is close enough to zero, cause a nonzero surface velocity pointing in the opposite direction as before. As a result the relative surface velocity oscillates around zero. To prevent this behavior the tangential force, for surface velocities close to zero, needs to be smaller than $\mu|\vec{F}_n|$. This is achieved by adding a viscous term

$$\vec{F}_{vis} = -\gamma \vec{v}_s. \tag{4.23}$$

The resulting tangential force is then given by the smallest of the two forces and the factor γ needs to be chosen large enough so that mainly the frictional force is applied. Taking the minimum of both forces as the actual tangential force is a widely used method which gives satisfactory results.

$$\vec{F}_t = -\mathrm{min}(\gamma \vec{v}_t, \mu|\vec{F}_n|\vec{v}_s) \tag{4.24}$$

As a drawback the contacts can bear no load for $|\vec{v}_s| = 0$ which is no problem in a collision-dominated system. On the other hand this force law is useless if one is interested in static frictional forces. As a solution Cundall and Strack [21] introduced a virtual spring at the contact. Denoting the tangential spring constant with k_t one can write

$$\vec{F}_t = -k_t \delta_t \vec{t}. \tag{4.25}$$

During the contact, starting at the time t_0 and ending at t_c, the length δ_t of this virtual tangential spring is calculated through

$$\delta_t = \int_{t_0}^{t_c} \vec{v}_s(t') \cdot \vec{t}(t') dt'. \tag{4.26}$$

According to the theory of Mindlin and Deresievicz [84, 85], the force-displacement relation depends on the normal deformation δ_n and following the calculation of Tsuji [83] one gets

$$k_t = 4 \frac{\sqrt{R_{ij}\delta_n}}{D_t}. \tag{4.27}$$

Here D_t is a material constant similar to D_n and given by

$$D_t = \frac{(2-\nu_i)(1+\nu_i)}{E_i} + \frac{(2-\nu_j)(1+\nu_j)}{E_j}. \tag{4.28}$$

With this model the force calculated from the spring length can be larger than $\mu|\vec{F}_n|$ given by the Coulomb. If this is the case, the spring length is reset such that the resulting force is equal to $-\mu|\vec{F}_n|\vec{t}$.

$$\vec{F}_t = \begin{cases} -k_t\delta_t\vec{t}; & \delta_t \leq \frac{\mu|\vec{F}_n|}{k_t} \\ -\mu|\vec{F}_n|\vec{t}; & \delta_t > \frac{\mu|\vec{F}_n|}{k_t} \end{cases} \tag{4.29}$$

During the discussion above it was assumed that in equation 4.26 the vector representing the tangential spring length always lies in the tangential plane of the contact. For long lasting contacts this assumption may be wrong. Therefore the spring with the length calculated in the previous time step has to be remapped into the new tangential plane.

$$\vec{\delta}_{t_{\text{remap}}} = \delta_t - \vec{n}(\vec{n}\delta_t) \tag{4.30}$$

In general the length of the vector needs to be preserved. But for a small enough time step the error produced by the cosine in the scalar product can be neglected.

4.1.3.1 Dissipation of energy

As for the damping in normal direction a viscous damping force

$$\vec{F}_{d_t} = \eta_t\vec{v}_s \tag{4.31}$$

to model the energy dissipation is introduced. The damping coefficient is set to

$$\eta_t = 2\sqrt{k_t m_{ij}}. \tag{4.32}$$

4.1.3.2 Summary

The normal force is given by $\vec{F}_n = -k_{ij}\delta\vec{n} + \eta_n(\vec{v}_{rel}\vec{n})\vec{n}$ while the tangential force follows $\vec{F}_t = -k_t\delta_t\vec{t} + \eta_t\vec{v}_s$.

4.1.4 The rotation of particles

As shown in equation 4.4 the tangential force acting on the individual particle gives rise to a torque $\vec{M}_i = \vec{r}_i \times \vec{F}_t$ which lets the particles rotate. When implementing this equation one needs to take into account the reduction of the lever arm $\vec{r}_i$ due to the normal deformation δ_n to conserve angular momentum. Therefore, for each particle, the length of the lever arm reduces by the height of its spherical cap which one gets when cutting the particle with the tangential plane of the contact. Thus the two torques $\vec{M}_i$ and $\vec{M}_j$ in a contact are given by

$$\vec{M}_i = (r_i - c_i)\vec{n} \times \vec{F}_t, \tag{4.33}$$

$$\vec{M}_j = -(r_j - c_j)\vec{n} \times \vec{F}_t. \tag{4.34}$$

The two constants c_i and c_j are the heights of the spherical caps and can be calculated through

$$c_i = (r_j - r_i + d)(r_j + r_i - d)/2d, \tag{4.35}$$

$$c_j = (r_i - r_j + d)(r_i + r_j - d)/2d. \tag{4.36}$$

Here d is the distance between the two particle centers as shown in Figure 4.1.

4.1.5 The linked-cell algorithm

Using a discrete element method to calculate the motion of every particle in the system one has to determine the interacting particles. For long range forces these are all possible particle pairs and in a system consisting of n particles this results in a $O(n^2)$ loop. When only short range forces apply the performance can be increased using the linked-cell algorithm with which the number of computations increases linearly $O(n)$.

Figure 4.2 explains how the linked-cell algorithm helps to find those pairs of particles which are overlapping. One subdivides the system into cells of the length l_c and each particle is assigned to the cell where its center lies in. Instead of checking every possible particle pair it is sufficient to consider the particle pairs between particles in a specific cell and the particles in the neighbor cells. To prevent double calculations only half of the neighboring cells have to be investigated. Thus every time step one sweeps over the system and when calculating the contacts inside a

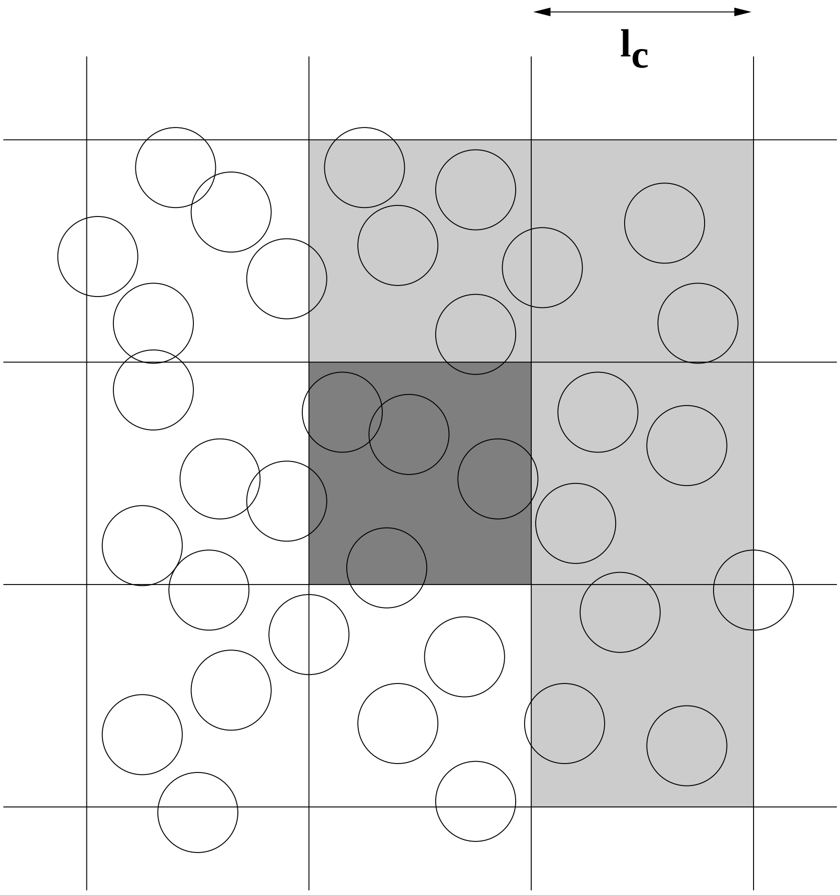

Fig. 4.2: Example of the linked-cell algorithm in two dimensions. The system is segmented into cells of equal length l_c and each particle is assigned to the cell where its center lies in. Sweeping over all cells the actual cell is shaded dark grey and the contacts for this cell are given by the particle pairs between all particles in the four grey shaded cells.

specific cell (dark grey in the picture) the contacts of the particles inside this cell and half of its neighboring cells (light grey) are also calculated.

The possible particle pairs determined in the linked-cell algorithm contain all pairs with overlapping particles if, starting from the last sweep, no particle traveled further than a given distance

$$d_s = (l_c - 2r_{max})/2. \tag{4.37}$$

Thus a further improvement can be achieved if this pair list is stored in a Verlet-list which is updated only if a particle traveled further than d_s.

Note that, when static friction is implemented, the length of the tangential springs in the contacts need to be remembered when updating the Verlet-list. Therefore, whenever the contact list is rebuild the spring lengths of the still existing contacts of the old list are copied to the new list.

4.1.6 The quad-tree

The previously discussed linked-cell algorithm is suitable for monodisperse or slightly polydisperse ($P = 0.5$) systems. As the cell size l_c must be larger than the biggest particle the Verlet-list contains many unnecessary contacts in a polydisperse system because each cell will, additionally to the large particles, contain many small particles.

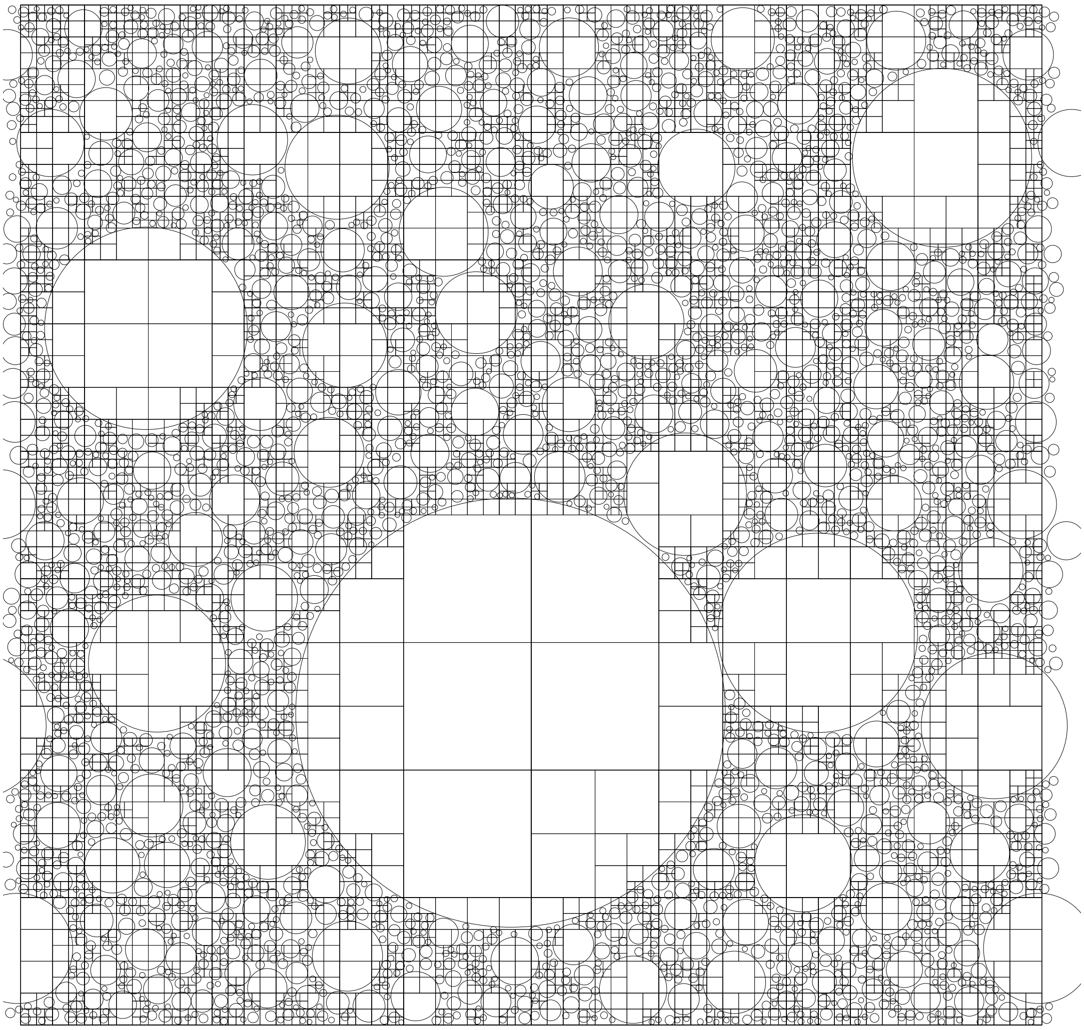

Fig. 4.3: Grid of variable cell size generated by the quad-tree. The grid is finer in regions with many small particles while it is coarse around big particles.

An alternative is the quad-tree shown in Figure 4.3. Here a grid with variable cell size is generated which is finer in regions with many small particles while it is coarse around big particles. The creation of the grid starts with the root cell, which contains the whole system and uses the following rule: If a cell contains more than one particle, it is subdivided into n smaller cells and each particle is transferred into that new cell where its center lies. We continue for the new cells if they contain more than one particle. The number of new cells n depends on the dimension D and is given by $n = 2^D$, which is four in two dimensions, giving the quad-tree its name.

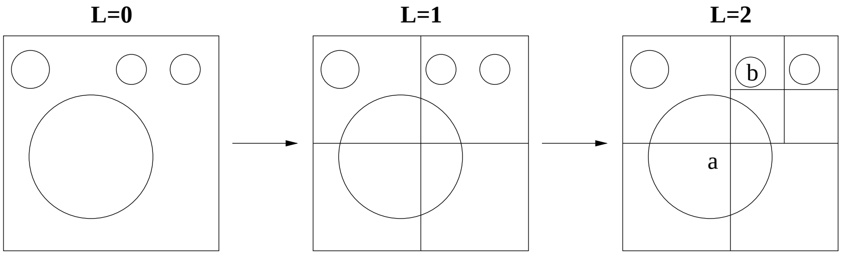

Fig. 4.4: Generating a quad-tree in two dimensions. Starting from the root cell on level $L = 0$, the space is divided into $n = 4$ sub cells which are then on level $L = 1$. As there are two particles in the upper right corner, this cell is again divided into 4 cells.

Figure 4.4 shows an example in two dimensions. Starting from the root cell on level $L = 0$, the space is subdivided into $n = 4$ sub cells which are then on level $L = 1$. As there are two particles in the upper right cell, this cell is again divided into 4 cells. For practical reasons a maximum depth level L_{max} is defined at which the subdividing is stopped even if it contains more than one particle. With $d_s = \frac{l}{2^{L_{max}+1}}$, which is half the size of the smallest cell, a large L_{max} results in a smaller Verlet-list but it needs to be updated more often as d_s becomes smaller.

To determine the contacts added to the Verlet-list, the following lists are needed for each cell:

- list $\mathbb{A}$: particles belonging to the cell
- list $\mathbb{B}$: particles overlapping the cell
- list $\mathbb{N}$: neighboring cells

If following the linked-cell algorithm one creates the Verlet-list simply by checking for contacts in the actual cell and its neighbors. However, due to the polydispersity several contacts would be missed. For instance, in

Figure 4.4, the contact between the big particle a, whose center lies in the lower left cell, and the small particle b. This is solved by checking the list $\mathbb{B}$ of the neighboring cells as well.

4.1.7 Integration scheme

In this section we discuss well known algorithms to solve equation 4.1. The easiest approach is the Euler-Algorithm where the change of velocity $\Delta\vec{v}_i$ for particle i at position $\vec{x}_i$ is calculated with

$$\Delta\vec{v}_i = \frac{\vec{F}_i(\vec{x}_i(t))}{m_i}\Delta t. \tag{4.38}$$

$\vec{F}_i$ is the force acting onto the particle with mass m_i and with the time step Δt the new position can be calculated via

$$\vec{x}_i(t+\Delta t) = \vec{x}_i(t) + \vec{v}_i(t)\Delta t. \tag{4.39}$$

Despite its speed, this algorithm is unsuitable for precise calculations as it has an error of the order $O(\Delta t^2)$. A better method is the Verlet-Algorithm which uses the third order tailor-expansion of $\vec{x}(t \pm \Delta t)$.

$$\vec{x}(t \pm \Delta t) = \vec{x}(t) \pm \vec{v}\Delta t + \frac{1}{2}\vec{a}(t)\Delta t^2 \tag{4.40}$$

Adding up these two equations gives the position in the next time step

$$\vec{x}(t+\Delta t) = 2\vec{x}(t) - \vec{x}(t-\Delta t) + \vec{a}(t)\Delta t^2 \tag{4.41}$$

while the velocity is given by

$$\vec{v}(t) = \frac{\vec{x}(t+\Delta t) - \vec{x}(t-\Delta t)}{2\Delta t}. \tag{4.42}$$

In this integration the error for the position is of the order $O(\Delta t^4)$ but the error for the calculation of the velocity is still of the order $O(\Delta t^2)$. Among others the Velocity-Verlet algorithm [86] overcomes this problem.

$$\vec{x}(t+\Delta t) = \vec{x}(t) + \vec{v}\Delta t + \frac{1}{2}\vec{a}(t)\Delta t^2 \tag{4.43}$$

$$\vec{v}(t+\Delta t) = \vec{v}(t) + \frac{1}{2}(\vec{a}(t) + \vec{a}(t+\Delta t))\Delta t \tag{4.44}$$

Here the error is only of the order of $O(\Delta t^5)$.

4.1.8 The time step

Choosing the right time step is a crucial process as more time for the simulation is needed if a small time step is chosen. On the other hand, a time step chosen too large results in an unphysical gain of energy and/or energy fluctuations. The underlying property with which the time step can be determined, is the time t_c two particles are in contact. For the Hook-model, this time can be calculated from the equation for a damped harmonic oscillator.

$$t_c = \frac{\pi}{\omega} = \frac{\pi}{\sqrt{\omega_0^2 - \eta_n^2}} \tag{4.45}$$

Here $\omega_0 = \sqrt{k_n/m_{ij}}$ is the resonance frequency of the oscillator and the viscosity is given by $\eta_n = \gamma/(2m_{ij})$. Due to the damping in normal direction, the interaction can end before the particles totally separate. Therefore the shorter time period

$$t_c^f = \frac{1}{\omega}(\pi - 2atan\frac{\eta_n}{\omega}) \tag{4.46}$$

from the beginning of the interaction to the point in time where F_n becomes attractive and thus is set to zero, is a better measure.

For the arbitrary force law of equation 4.15 one has to neglect the damping term ($\eta_n = 0$) and following the calculation documented in [82] one gets

$$t_c = J(\theta)(1 + \frac{\theta}{2})^{1/(2+\theta)}(\frac{2Dm_{ij}}{(4R_{ij})}^{1-\theta} v_0^{-\theta/(2+\theta)}). \tag{4.47}$$

Here v_0 is the velocity before the contact and for $J(\theta)$ one gets $J(0) = \pi$ and $J(1/2) = 2.94$. Finally, for the Hertz-law, one can write:

$$t_c = 4.54\frac{m_1 2D_n^{2/5}}{\sqrt{R_{ij}}} v_0^{-1/5} \tag{4.48}$$

The time step Δt itself is then a fraction of the contact time. To have a good resolution of the contact $\Delta t = t_c/50$ was chosen.

4.1.9 Rolling particles in polydisperse systems

In this section we describe an interesting artefact in almost non-moving polydisperse systems where static friction is implemented as previously

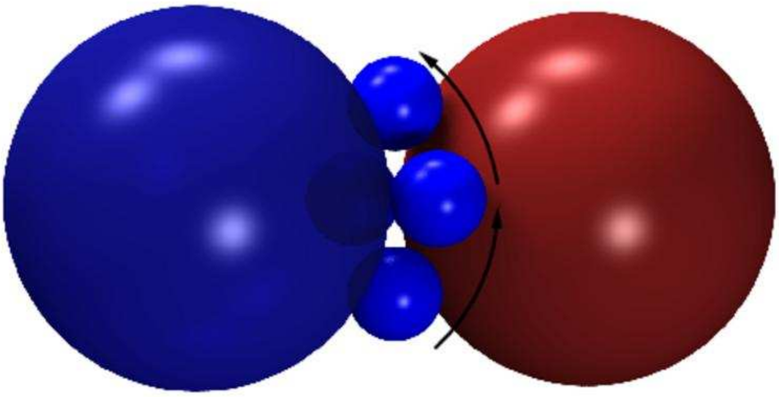

Fig. 4.5: In an extremely polydisperse system one encounters situations where a smaller particle is trapped between larger ones. The four small particles in the picture show the same particle at different points in time. Without rolling friction this particle rolls forever on the surface of the two larger spheres as the frictional force, exerted from the virtual tangential springs, is strong enough to cancel the normal force.

described. Figure 4.5 shows a typical situation that can emerge during the relaxation of such a system. A smaller sphere is clamped between two large spheres. The four smaller spheres in the picture are the same particle only at different points in time. In such a situation, the virtual springs modeling the static friction might prevent a small and slowly moving particle in contact with the larger two to detach. Here the major part of the normal, and thus repulsive, forces between large and small particles cancel and the frictional force is strong enough to prevent a separation of the particles. Without rolling friction the small particle will roll on the surface of the larger ones forever. Its circular path is schematically shown by the four small spheres.

In a compactified monodisperse system one never finds such a situation as a reasonably dense packing does not allow for such a configuration and it can be neglected in a non static system. But performing the measurement described in chapter 6 it will cause an oscillation in the measured repulsive force. Instead of a computational costly implementation of rolling friction the rolling is stopped by setting, from time to time, all translational and rotational velocities in the system to zero.

4.2 Contact Dynamics

In the previous section the molecular dynamics, which is a smooth integration method, was explained. Using it to simulate extremely rigid particles is very time consuming as the time step depends on the elasticity of the particles. Contact dynamics (CD) on the other hand [15–17,87] works with perfectly rigid particles interacting via point contacts. This means, when two particles are in contact, the repulsive force $\vec{F}_n$ can take any value necessary to prevent an overlap of the interacting particles as shown in Figure 4.6. As a consequence the changes in the forces onto the particles are not smooth anymore but have jumps. This comes from the underlying concept that the motion of the particle has to fulfill certain constraints. One constraint is the prevention of particle interpenetration also referred to as volume exclusion. The other constraint is the absence of sliding due to static friction.

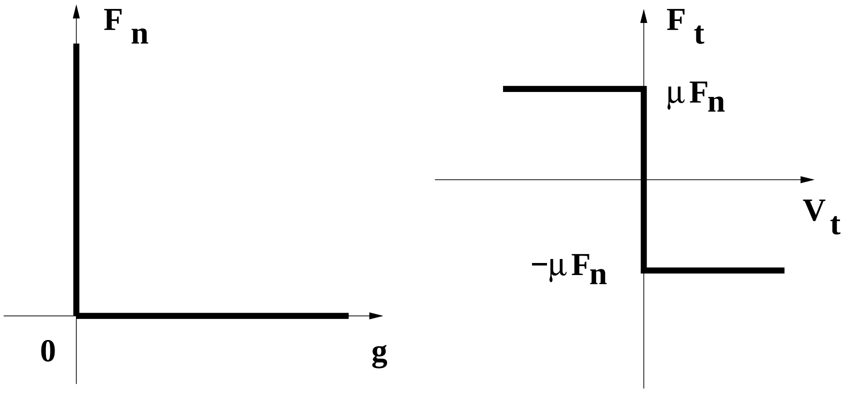

Fig. 4.6: The left picture shows the signorini graph with the surface distance g between two particles. For particles not in contact the repulsive force F_n is zero. When in contact it can take any value necessary to prevent an overlap of the interacting particles. The right picture shows the tangential force as a function of the tangential velocity. Its maximum value is given by the Coulomb law.

4.2.1 Two particle contact

In the contact dynamics the interacting particles are touching but not overlapping as the particles are infinitely rigid. For a two particle contact the normal vector $\vec{n}$ points from particle i to particle j and the relative velocity $\vec{V}'$ is given by

$$\vec{V}' = \vec{v_j} - \vec{v_i} - (r_i\vec{\omega}_i + r_j\vec{\omega}_j) \times \vec{n}. \tag{4.49}$$

Note that this relative velocity is different from the one defined for the molecular dynamics in equation 4.7. If the particles approach each other and get in contact, contact dynamics tries to eliminate this velocity.

Reducing the above velocity to zero will set the particles to rest such that they are touching but not overlapping. This corresponds to a zero restitution coefficient $e = 0$. In general the particles have a finite velocity after the collision and thus the necessary change in velocity is greater than $\vec{V}'$. This velocity $\vec{V}$ is given by

$$\vec{V} = -(1 + e_n)(\vec{V}' \cdot \vec{n})\vec{n} - (1 + e_t)(\vec{V}' - (\vec{V}' \cdot \vec{n})\vec{n}). \tag{4.50}$$

Here the restitution coefficient is split into a normal part e_n and a tangential part e_t.

To eliminate the relative velocity a normal force $\vec{F}_n$ and a tangential force $\vec{F}_t$ is applied which results in the velocity change

$$\Delta\vec{V} = (\frac{\vec{F}_n}{m_{ij}} + \frac{\vec{F}_t}{m_t})\Delta t. \tag{4.51}$$

Here m_{ij} is the reduced mass in the contact and m_t is given by

$$m_t = (\frac{1}{m_n} + \frac{\vec{l}_i^2}{I_i} + \frac{\vec{l}_j^2}{I_j}). \tag{4.52}$$

Thus the normal and tangential force acting on the particles can be written as

$$\vec{F}_n = -m_n(1 + e_n)(\vec{v}_j - \vec{v}_i\vec{n}), \tag{4.53}$$

$$\vec{F}_t = -m_t(1 + e_t)[(\vec{v}_j - \vec{v}_i) - (\vec{v}_j - \vec{v}_i)\vec{n} - (r_i\vec{\omega}_i + r_j\vec{\omega}_j) \times \vec{n}]. \tag{4.54}$$

As in the molecular dynamics, the maximum tangential force is $\mu|\vec{F}_n|$ and if the force calculated in equation 4.54 is larger it is reset to this value.

As the contact dynamics is an implicit algorithm an implicit Euler algorithm is used to calculate the new positions and velocities of the particles.

$$\vec{r}_i(t + \Delta t) = \vec{r}_i(t) + \vec{v}_i(t + \Delta t)\Delta t \tag{4.55}$$

$$\vec{v}_i(t + \Delta t) = \vec{v}_i(t) + \frac{1}{m_i}\vec{F}_i(t + \Delta t)\Delta t \tag{4.56}$$

4.2.2 Multiple Contacts

In the discussion above it was omitted that each particle is also influenced by external forces $\vec{F}_{ext}$ and in general is in contact with more than one particle. Due to the forces from the adjacent contacts the particle-particle contact cannot be solved locally. Instead an iterative solver is used.

For each particle the actual velocity $\vec{v}_i$, calculated in the previous time step, and the change in velocity $\delta\vec{v}_i$, resulting from the forces acting during the actual time step, is given. Taking into account this velocity change equation 4.49 can be rewritten to

$$\vec{V}' = \vec{v}_j + \delta\vec{v}_j - (\vec{v}_i + \delta\vec{v}_i) - (r_i\vec{\omega}_i + r_j\vec{\omega}_j) \times \vec{n}. \tag{4.57}$$

The iterative solver determines the velocity change $\delta\vec{v}_i$ in the following way:

1. At the beginning of each time step the velocity change $\delta\vec{v}_i$ of all particles is set to zero.
2. In the second step external forces are taken into account. For every particle the velocity change $\delta\vec{v}_{i_{ext}}$ due to these forces is calculated.

   $$\delta\vec{v}_{i_{ext}} = \frac{\vec{F}_{ext}}{m_i}\Delta t \tag{4.58}$$

   The velocity change $\delta\vec{v}_i$ is then set to $\delta\vec{v}_{i_{ext}}$.
3. In the third step a particle contact is randomly picked and the necessary forces $\vec{F}_t$ and $\vec{F}_n$ to eliminate the relative velocity $\vec{V}$ are calculated. The resulting velocity change for particle i and j in the contact is added to $\delta\vec{v}_i$ and δv_j respectively. Note that constant forces from other contacts of particle i and j are assumed while calculating the velocity change.

Step three is repeated until the results are accurate enough or a given number of iterations was performed. For the convergence criteria we chose

$$|\delta\vec{F}_{n/t}| \leq \epsilon|\vec{F}_{n/t}|; \qquad \epsilon < 1 \tag{4.59}$$

Thus the iteration process stops if for all contacts the change in force is smaller than $\epsilon\vec{F}$ or if a certain number of sweeps N is exceeded.

The calculating of each contact in a random order prevents a bias of information spreading. The random sweep differs from the random sequential update as for the latter one a contact could be chosen more than once in a single sweep.

4.3 Comparison of molecular and contact dynamics

The main differences between the two methods described above are the following: Contact dynamics simulates infinitely rigid particles and allows for a relatively large time step but the forces applied to the individual particle are non continuous. In the molecular dynamics the particles are elastic and the repulsive force is calculated from the overlap of interacting particles. This results in a small time step when simulating very stiff particles.

5

Shearing with lubricants

As stated in the introduction an estimated 40% of energy is wasted during the transport and handling of granular material. Thus for the industry it is of great importance to extend the knowledge about these materials under the various conditions of processing.

Very interesting is the shear behavior of granular media. Here, the internal force chains, carrying the external stress, break up and besides stress fluctuations [88, 89], dilatancy can be observed. Dilatancy is one of the fundamental properties of granular media and first studies where done by Reynolds in 1885 [25]. Additionally the viscosity of such a sheared system strongly depends on its size distribution and extensive studies have been mainly conducted on bidisperse suspensions. For a given total solid volume fraction, the viscosity decreases, as the ratio r_1/r_2 between the radius r_1 of the large particle and the radius r_2 of the small particle increases [26,27]. Above a ratio of 10:1 the viscosity is relatively unaffected by further ratio changes. Using colloidal bidisperse systems, optima in viscosity occur for a size ratio of two to four as ultimately, viscosity increases with a larger size ratio [28]. One of the fundamental theories describing the viscosity for multimodal suspensions was developed by Farris [29] and later on extended by Sengun and Probstein [30].

In this chapter we describe numerical studies performed in collaboration with BASF in Ludwigshafen, Germany. The polydisperse material of interest consists of spherical particles immersed in water and shows a non-Newtonian behavior. A similar material can easily be prepared in the kitchen when starch is dissolved in cold water. At a high enough concentration the mixture behaves like a solid when impacted sharply but slowly flows out of the bowl if it is turned upside down. For Dr. Distler from BASF, it was of great interest to study the change in the shear behavior when a lubricant is added. Thus we developed the following two dimensional model where so-called repulsive point-like particles which model the behavior of the added lubricant are introduced [90]. First the shear behavior of bi- and polydisperse systems is compared and then the change of the shear properties of the polydisperse system due to the addition of point-like particles is discussed.

5.1 The model

First different size distributions used in the model are defined. Then the concept of point-like particlesïs introduced. Afterwards an overview over the simulation method, including the procedure used to initialize the system, is given. Finally compaction and shearing of the system are explained.

5.1.1 Used size distributions

In the simulations bidisperse and a polydisperse size distribution are used. The bidisperse distribution contains particles of two different sizes. The radius of the large particles is r_{max} while the radius of the small particles is r_{min}. To fully define this distribution the ratio

$$\tau = \frac{N(r_{max})}{N(r_{min})} \tag{5.1}$$

between the number of big particles and the number of small particles is defined. Here $N(r)$ is the number of particles of a given size r.

On the other hand the polydisperse distribution is given by the truncated power law

$$p(r) = ar^{-b}, \qquad r_{min} < r < r_{max} \tag{5.2}$$

introduced in chapter 3. The interaction between the individual grains is resolved with contact dynamics which was described in section 4.2.

In the simulation the restitution coefficient was set to $r_c = 0.2$ and the friction coefficient was set to $\mu = 0.3$.

5.1.2 The concept of point-like particles

To simulate the added lubricant, so called point-like particles are introduced. They have zero mass and a potential U which gives rise to a repulsive force F_r on every particle closer than the distance d_r. As they have no mass and occupy no volume they do not contribute to the volume fraction of the system and might experience infinite accelerations. Therefore we use a different iteration scheme in the contact dynamics for calculating their motion. At the beginning of every time step, each point-like particle is moved to a position where the net force on it vanishes. Then the forces exerted by the point-like particles on the other particles are computed, and the contact dynamics time steps proceeds normally. The potential of the point-like particles is given by

$$U(d) = \begin{cases} k\hat{d}^{-1}e^{-\gamma\hat{d}} + F_0\hat{d} + U_0, & 0 < \hat{d} < 1 \\ 0, & \hat{d} \geq 1 \end{cases} . \tag{5.3}$$

Here d_r is the interaction radius which corresponds to the radius of a solid particle and d is the separation between the surfaces of two interacting particles which defines the dimensionless surface distance $\hat{d} = d/d_r$.

The first term in equation 5.3 is a screened long-range potential where k determines the strength of the potential while γ fixes how fast it decays with the distance. The constants F_0 and U_0 in the second and third term are chosen such that potential and force are continuous at $d = d_r$.

The repulsive force F_r is the gradient of the potential:

$$F_r(d) = -\frac{\partial U}{\partial d} = \begin{cases} k\hat{d}^{-1}e^{-\gamma\hat{d}}(\hat{d}^{-1} + \gamma) - F_0 & 0 < \hat{d} < 1 \\ 0 & \hat{d} \geq 1 \end{cases} \tag{5.4}$$

To distinguish between the point-like particles and "normal" particles the latter ones will be called "grains".

5.1.3 Simulation Method

In this section the setup of the simulation is explained. After filling the shear cell with an initial configuration of particles it is compactified and in the last stage the system is sheared.

5.1.3.1 The shear cell

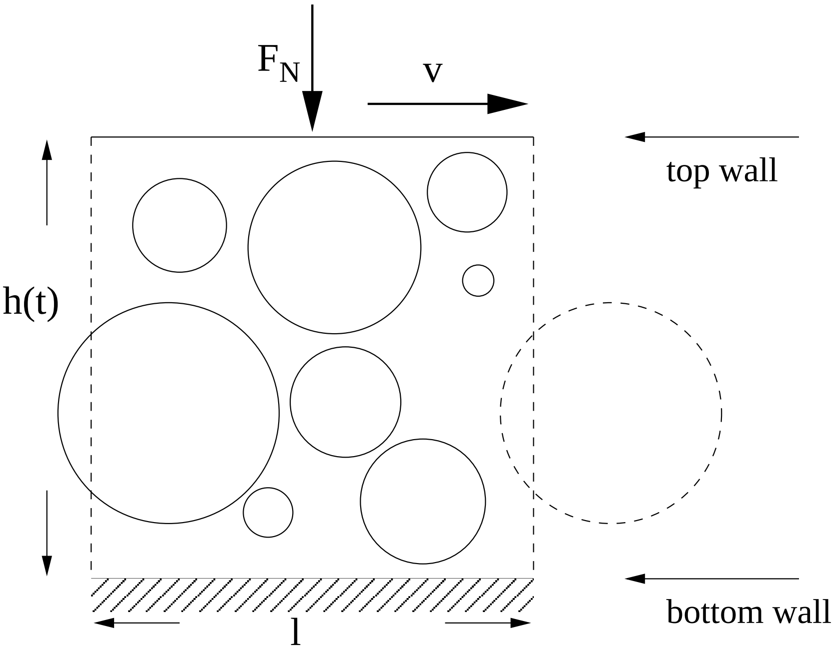

Fig. 5.1: The shear cell with periodic boundaries. The length of the cell is l and the actual height of the lid is given by $h(t)$. While the lid is sheared with the velocity v the normal force F_N is exerted onto the lid.

Figure 5.1 shows the two dimensional shear cell. Periodic boundary conditions are applied such that particles leaving the cell to the left will reenter on the right and vice versa. The length of the system is $l = 10cm$, the area V_C of the shear cell is given by $V_C = l^2$ and the density of the particles is $\rho = 10^3 kg/m^3$. The bottom wall is assigned an infinite mass which will fix its position while the top wall is allowed to move up and down. In all simulations the top wall or lidïs subject to a normal force $F_N = 100N$ and its position is given by its height $h(t)$. Its mass is set to 10^{-5} kg which is roughly twice the mass of the largest particle in the system. For all simulations gravity was turned off.

5.1.3.2 Initialization

For the generation of a random packing several algorithms like random packing under gravity (RPG) [91,92], growing of spheres [93–95] and random sequential adsorption (RSA) [96] have been proposed and Zhang et al. [97] showed that the RSA algorithm is the most random method. This algorithm picks a grain from a reservoir and inserts it at a random position into the system if it does not overlap with already inserted grains. The distribution of grains in the reservoir can be set to any desired distribution and in general desorption may also be possible.

For polydisperse packings, Tomaso Aste [98] introduced an hierarchical RSA-algorithm. He starts with a given radius r and adsorbs as many grains of this radius as possible. When no space for grains of this size is left the radius is divided by a given factor and the adsorption continuous. We adapted this algorithm such that instead of the discrete size distribution we are able to use a quasi-continuous one.

First a separate reservoir is filled with grains where the volume V_R of all grains in the reservoir is given by

$$V_R = \sum_i^n \pi r_i^2. \tag{5.5}$$

Here n is the number of grains in the reservoir and r_i is the radius of the ith grain. When simulating bidisperse systems, for every large grain, $1/\tau$ small grains are inserted. For the polydisperse systems the grains are randomly generated from the truncated power law. In both cases the filling of the reservoir is stopped when $V_R > \beta V_C$. and the factor β is set to $\beta = 0.7$.

In the next step the indices of the n grains in the reservoir are changed such that $r_1 > r_2 > ... > r_n$. In other words, the reservoir is sorted by size, such that the largest grain comes first. Starting with the first and largest one, each grain gets $I = 1000$ trials to find a random position where it does not overlap with any already present grain. In general a grain is discarded after I trials but with the chosen values for β and I it was possible to insert all particles in the reservoir into the shear cell.

If point-like particles are used in the simulation they are put in next. We take N_p point-like particles and give them I_p trials for adsorption. As $r = 0$ all N_p point-like particles can be put into the system for a large enough I_p.

When averaging over several simulations the same n grains and the same number N_p of point-like particles in the reservoir was used but a different seed for the random number generator, choosing the positions of the particles, was selected. Thus the distribution of particle sizes remains exactly the same, only the initial configurations are different.

5.1.3.3 Compaction

As all particles in the reservoir were inserted into the shear cell the actual volume fraction Φ of the system is given by

$$\Phi(t) = \frac{V_R}{lh(t)}. \tag{5.6}$$

To reach a specific volume fraction Φ_0 at which the shearing starts, a fixed normal force F_N is exerted onto the lid and, in certain time intervals, the grains feel a random force in a random direction. Due to the force F_N the system is compressed while the random forces break up arches and thus allow for better compaction. Additionally friction is turned off ($\mu = 0$) and the strength of the potential is set to $k_i = 10^{-3}N$. As soon as the volume fraction Φ reaches the desired value Φ_0 the compaction is stopped, friction is turned on ($\mu = 0.3$), k is set to a value greater or equal to k_i and the shearing is started.

5.1.3.4 Shearing

After compaction the granular material is sheared by moving the lid with the constant velocity v.

Before the shearing all grains with a radius smaller than $2r_{min}$ and a distance smaller then $r_{min}/2$ away from the top and bottom wall are fixed to these walls to simulate a rough surface. These grains do not experience the grain-wall interaction anymore and all forces such a grain feels from its contacts with other grains or point-like particles is applied directly to the wall. Thus the grains fixed to the bottom do not move anymore as the mass of the bottom wall is set to infinity and the particles fixed to the lid move with the constant velocity v.

The position of the lid at the moment the shearing starts is the reference height h_0. As the lid is sheared with a constant velocity v, the position h of the lid and the force F, needed to keep v constant, is measured. Shearing is done for at least 0.1 seconds in all simulations. For the slowest shear velocity the lid moves at least a distance $l/2$ in horizontal direction.

5.2 Method of analysis

The shearing is characterized by three parameters, the angle of dilatancy Ψ and the saturation dilatancy d_s which characterize the movement of the lid and the force F_s needed to maintain the shear motion.

5.2.1 Dilatancy

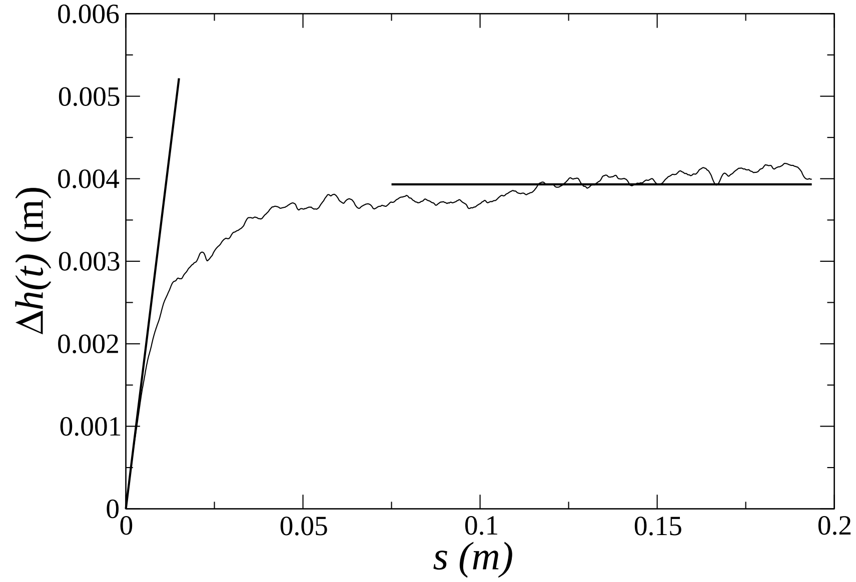

Fig. 5.2: Expansion Δh versus the shear distance s for the polydisperse system. For small values of s, Δh increases almost linearly. For larger values Δh fluctuates around a saturation value h_s. The straight lines show the fit used to obtain Ψ and h_s.

Figure 5.2 shows the change in the height h of the lid as a function of the shear distance $s = vt$. When the shearing starts, the lid almost linearly moves upwards and its position can be described by

$$h(t) = h_0 + s \tan \Psi = h_0 + \Delta h. \tag{5.7}$$

Here s is the distance the lid was moved, Ψ is the angel of dilatancy and h_0 is the height of the lid before the shearing. Ψ is given by the slope of a straight line fitted to $h(t)$ for small s.

After a large enough shear distance the position of the lid fluctuates about the saturation height h_s. This is determined from the saturation dilatancy

$$d_s = h_s / h_0 - 1 \tag{5.8}$$

which is a measure of how much a medium expands when subject to shear. It is determined by fitting a straight line to the measurements as shown in Figure 5.2.

5.2.2 Shear force

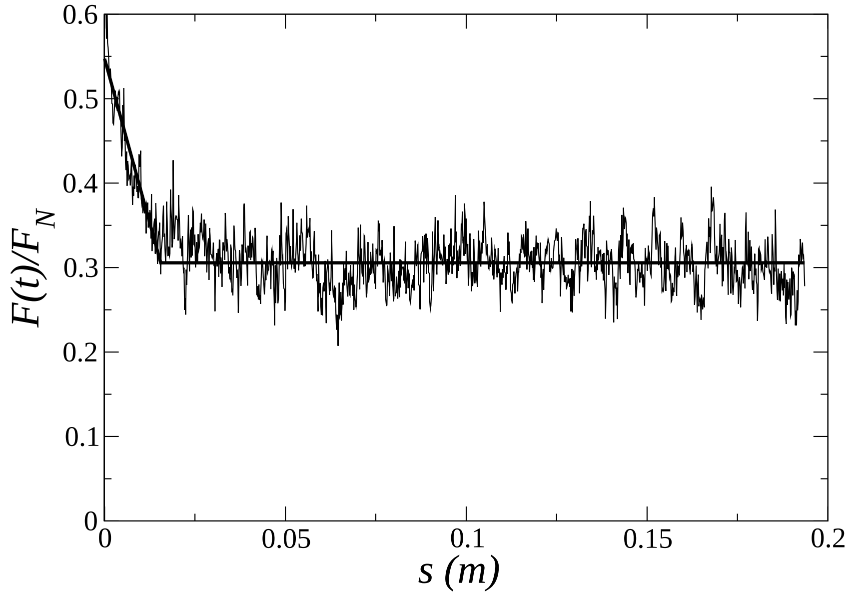

Fig. 5.3: The force exerted onto the lid as a function of the shear distance s, for the simulations shown in Figure 5.2.

Figure 5.3 shows the shear force exerted onto the lid as a function of the shear distance s, for the simulation shown in Figure 5.2. The force is large when the shearing starts but decreases over time until it fluctuates around a saturation force F_s. This force is called the shear force and can be determined by fitting a constant value to the measurement for large shear distances.

5.3 Results

Three variants of a two-dimensional system with circular grains were simulated. A bidisperse mixture, a polydisperse one and a polydisperse one with point like particles.

We first compare the shear behavior of bidisperse and polydisperse mixtures and in the second part we investigate how the shear behavior is influenced by the point-like particles.

5.3.1 Bidisperse and polydisperse mixtures

Two bidisperse mixtures and a polydisperse one were investigated. In the polydisperse mixture, the sizes are distributed according to equation 5.2 with $b = 3.5$. For the bidisperse mixtures the size ratio was set to $\tau = 1/45$ and $\tau = 1/60$ [see equation 5.1]. In both bidisperse mixtures the polydispersity was $P = 10$ ($r_{min} = 0.1$cm, $r_{max} = 1$cm) and the simulations were done with either 575 (polydisperse), 690 ($\tau = 1/45$), or 732 ($\tau = 1/60$) grains.

Each mixture was studied at two or three initial volume fractions. All mixtures were studied at $\Phi = 0.887$ and 0.876. In addition the bidisperse mixtures were examined at $\Phi = 0.911$. For each configuration ten different samples were prepared and the shear velocity was set to three different values $v = 0.5, 1.5, 4.5$m/s. For each group the time series of ten simulations were averaged over to obtain the shear parameters.

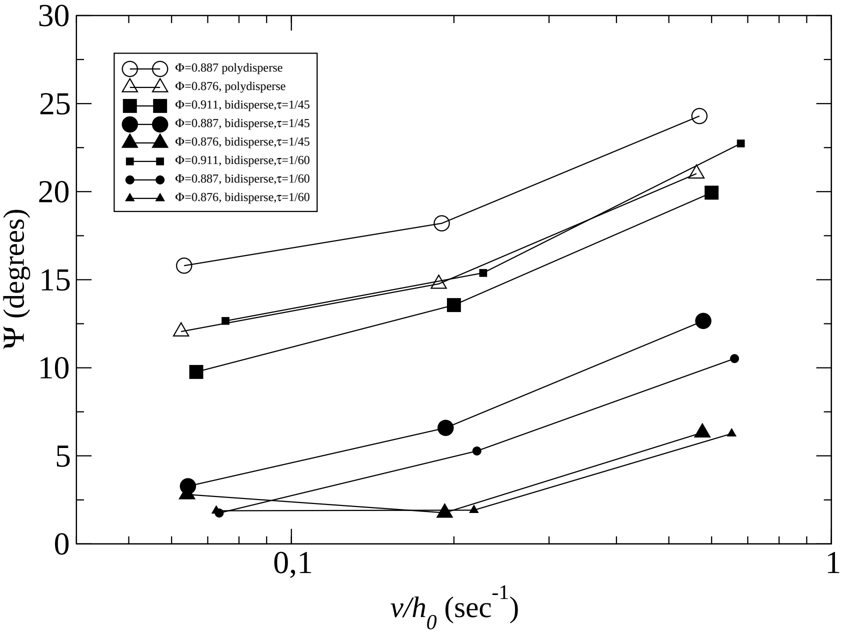

Fig. 5.4: Dilatancy angles Ψ for bidisperse and polydisperse mixtures, as a function of the initial shear rate v/h_0 . The highest volume fraction ($\Phi_0 = 0.911$) could only be obtained with the bidisperse mixtures. The angle of dilatancy increases with shear velocity and volume fraction but is roughly three times smaller for bidisperse mixtures than for polydisperse ones.

Figure 5.4 shows the angle of dilatancy Ψ as a function of the initial shear rate v/h_0 for the different simulations. Here the angle of dilatancy increases with shear velocity and volume fraction but is roughly three times smaller for bidisperse mixtures than for polydisperse ones. On the other hand, at the maximum volume fraction ($\Phi_0 = 0.911$), the bidisperse mixture's angle approaches those of the polydisperse mixture. Note that this volume fraction could not be obtained for the polydisperse mixture.

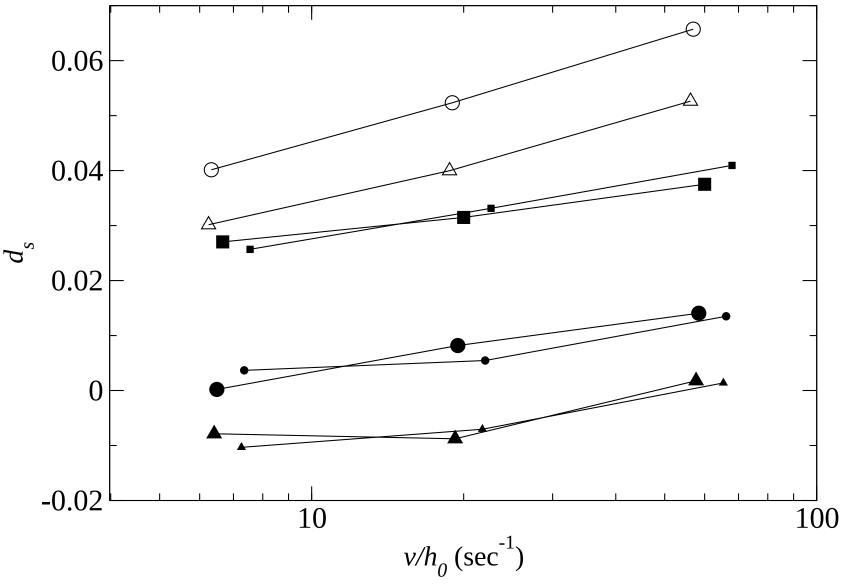

Fig. 5.5: Saturation dilatancy d_s for polydisperse and bidisperse systems. The symbols are the same as those used in Figure 5.4. As for the angle of dilatancy the saturation dilatancy increases with velocity and volume fraction and is for polydisperse mixtures greater than for bidisperse mixtures. Note the negative dilation for the bidisperse system depicted by the large filled triangles.

The saturation dilatancy for the studied systems is shown in Figure 5.5 where d_s is plotted as a function of the initial shear rate. As for the angle of dilatancy, the saturation dilatancy increases with velocity and volume fraction and is for polydisperse mixtures greater than for bidisperse mixtures. An important difference is the fact that for the lowest initial volume fraction only bidisperse mixtures exhibit negative dilation. This means that the height h_s at the end of the shearing is lower than h_0 at the beginning. This occurs because the small grains do not fill all the spaces between the large grains during the preparation of the sample. When the shearing starts, there can be large voids between the big grains. As the shearing proceeds, the large grains move relative to one another, the voids are opened up, and quickly filled with small grains. The voids never reform, leading to a permanent decrease in the height of the lid.

Figure 5.6 shows the shear force F_s divided by F_N versus the initial shear

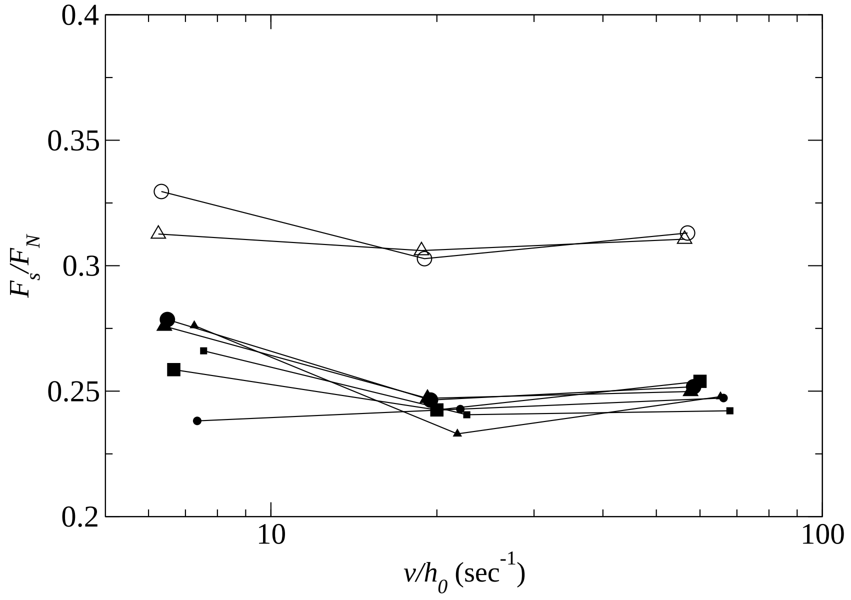

Fig. 5.6: The saturation value of the shear force, divided by the imposed normal force F_N, versus the initial shear rate for polydisperse and bidisperse grains. The symbols are the same as those used in Figure 5.4. Note that all values are close to the friction coefficient $\mu = 0.3$ used in the simulations. The force measured for the polydisperse systems is about 30% higher than for the bidisperse ones and is roughly independent of the initial volume fraction. Surprisingly, it decreases slightly with velocity, at least between $v = 0.05$ and $v = 0.15$.

rate for the different series of simulations. The force measured for the polydisperse systems is about 30% higher than for the bidisperse ones and is roughly independent of the initial volume fraction. Surprisingly, it decreases slightly with velocity, at least between $v = 0.5\mathrm{m/s}$ and $v = 1.5\mathrm{m/s}$. This differs from other cases, where the force is always observed to increase with shear velocity [99]. However, that work concerns flow of approximately monodisperse polygons, whereas we have studied disks. The decrease in F_s can be understood as a consequence of dilatancy. At higher velocities, dilatancy increases and thus making it easier to shear.

5.3.2 Influence of the point-like particles

In this section the influence of the point-like particles onto the shear behavior of a polydisperse mixture is studied. Again, the size distribution in the polydisperse mixture follows equation 5.2 with an exponent $b = 3.5$. For the point-like particles four parameters can be changed.

The strength k and the range d_r of the potential as well as the parameter γ determine how fast the potential decays with the distance. The fourth parameter $A = \frac{N(\text{point-like})}{N(\text{grains})}$ gives the number of point-like particles, divided by the number of grains. The parameters were set to the following values: $k = 2, 5, 10 \times 10^{-3}N$, $d_r = \frac{1}{5}r_{max}, \frac{2}{5}r_{max}$, $\gamma = 3$ and $A = 1, 2$. For all simulations the volume fraction was set to $\Phi = 0.882$ and the shear velocity to $v = 1.5$m/s. In both mixtures the polydispersity is $P = 10$ and $r_{min} = 0.11$cm, $r_{max} = 1.1$cm. For each set of these three parameters ten simulations with different initial configurations were averaged together. For some systems the strength of the potential was set to $k = 20, 50, 100 \times 10^{-3}N$.

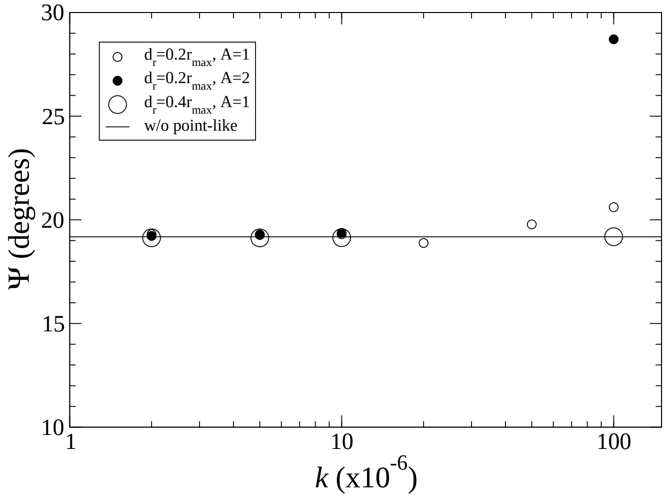

Fig. 5.7: Dilatancy angles Ψ for polydisperse mixtures with and without point-like particles, versus the strength k of the repulsive potential. In all cases, the volume fraction is 0.882 and the shear velocity is 1.5m/s. The addition of point-like particles does not cause much change. The observed angles vary by about one degree from the value found without point-like particles which is depicted by the horizontal line.

Figure 5.7 shows Ψ as a function of k for the different types and numbers of point-like particles. One data point stands out from the rest: ($\Psi \approx 29^\circ$, $k = 100 \times 10^{-3}N$, $A = 2$). For the moment, we exclude it from the discussion and treat it separately in section 5.3.2.1. Except for this one series of simulations, the addition of point-like particles does not cause much change. The observed angles vary by about one degree from the value found without point-like particles. Thus Ψ is much less sensitive to a change in k than to a change in shear velocity or initial volume fraction.

A very surprising feature of the shear behavior extracted from Figure 5.7 is that point-like particles with a large distance of interaction cause less change than particles with a small distance. (Compare the large and small empty circle at $k = 100 \times 10^{-3}N$.)

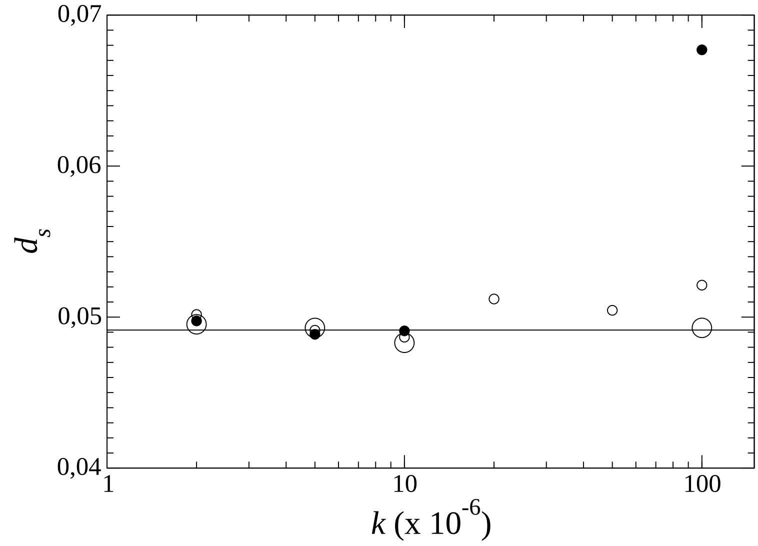

Fig. 5.8: Saturation dilatancy d_s for mixtures with different concentrations of point-like particles. The symbols are the same as those used in Figure 5.7. The presence of point-like particles changes the behavior of the mixture very little.

The saturation dilatancy d_s as a function of k for the simulated systems is shown in Figure 5.8. The data are very similar to those discussed above. The simulations with $k = 100 \times 10^{-3}N$ and $A = 2$ are widely separated from all the others. Except for this one data point, the presence of point-like particles changes the behavior very little. When point-like particles are added, the dilatancy changes by at most 0.003. The changes due to the change in volume fraction or shear rate, observed in the previous section were seven times larger.

Figure 5.9 shows the shear force F_s as a function of F_N when the lid fluctuates about its saturation height h_s for the different series of simulations. This time, the point-like particles change the behavior of the mixture. When short-range point-like particles are added (with $d_r = r_{\max}/5$, the small circles in the figure), the force decreases substantially. At large k,

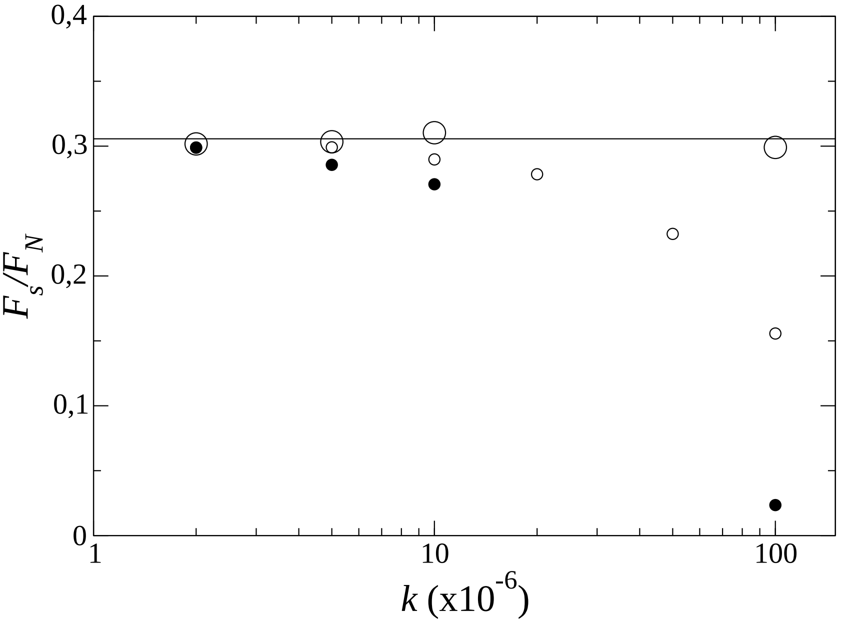

Fig. 5.9: The saturation value of the force F_s, divided by the imposed normal force F_N, for systems with different concentrations of point-like particles. The symbols are the same as those used in Figure 5.7. Note that $F/F_N \approx \mu$ when k is small. When short-range point-like particles are added to the polydisperse mixture (with $d_r = r_{\max}/5$, the small circles in the figure), the force decreases substantially. At large k, the force is reduced to half of its original value, or very nearly removed, depending on how many point-like particles are added.

the force is reduced to half of its original value, or very nearly removed, depending on how many point-like particles are added.

Surprisingly, adding the long-range particles does not reduce the force at all. This continues the general trend observed in the previous discussion, where we saw that the particles with a large interaction distance did not have much effect. One possible reason for this is that when d_r is small, the grains feel only those point-like particles that occupy the neighboring pore spaces. The force exerted on the grains is thus tightly connected to the geometry of the surrounding particles, and this force is such that it reduces the friction between the grains. When d_r is large, grains interact with point-like particles in many different regions, and the resulting forces are no longer so closely related to the geometry of the neighboring particles.

5.3.2.1 Behavior at large k and A

In Figure 5.7, one observes for large k and A a very high angle of dilatancy (nearly $30°$ compared with all the other points near $20°$), and in Figure 5.8 a very high saturation dilatancy (roughly 40% more than any other point). In addition, the force needed to shear this mixture is very low - only 10% of the mixture without point-like particles. This last result suggests that the point-like particles carry a significant fraction of the weight of the lid. This would explain the very high dilatancy. Note that all the samples are prepared by compressing mixtures with $k = 10^{-3}N$. When the shearing starts, k is set to its final value. If k is very large and the point-like particles are numerous, the mixture will expand not due to shearing, but simply because the point-like particles push against each other with enough force to lift up the lid.

This explanation has been confirmed by simulations of unsheared systems. The system is prepared as before, but is not sheared. When $k = 100 \times 10^{-3}N$ and $A = 2$, one observes a substantial dilation ($d_s \approx 0.28$) due only to the repulsive potential of the point-like particle. On the other hand, when $k = 100 \times 10^{-3}N$ and $A = 1$, no such dilation is observed. Therefore one can conclude, that the point at $k = 100 \times 10^{-3}N$ and $A = 2$ is in a different regime from the other points.

5.3.2.2 Dependence on polydispersity

All of the above results were obtained with a polydisperse mixture described by a power law exponent $b = 3.5$ [see (equation 5.2)]. Mixtures with $b = 1.3$ were also tried. Point-like particles with $d_r = 0.022$ and $2 \times 10^{-3}N \leq k \leq 100 \times 10^{-3}N$ were added. No significant change in the dilatancy or force is observed, even for the largest values of k. This may be because there are fewer small grains, and the pore spaces are much larger. The point-like particles can then stay in the middle of this pore spaces and interact only weakly with the grains.

5.4 Conclusion

The findings of this study can be summarized by saying that the polydisperse mixtures show stronger dilatancy and a greater resistance to shear than the bidisperse mixtures. At constant volume fraction, the angle of dilatancy, the saturation dilatancy, and the force needed to maintain the shearing were all greater for polydisperse particles. However, this simple conclusion is complicated by the fact that higher volume fractions were easier to obtain with bidisperse mixtures. When bidisperse mixtures are very dense, their angle of dilatancy and saturation dilatancy is similar to polydisperse systems at lower volume fractions (although the shear force remains significantly smaller).

Adding repulsive particles to a sheared polydisperse mixture of grains changes the kinematic behavior of the mixture very little, but the dynamic behavior shows a reduction in the forces. "Kinematic" refers to those properties that concern the movement of the mixture - the angle of dilatancy and the saturation dilatancy. "Dynamic" behavior refers to the force necessary to maintain a fixed shear velocity. This finding is complicated by two additional observations. First, particles with a large interaction distance cause little change, in spite of exerting larger forces. The second observation is that it is possible to get dramatic changes in the kinematic behavior when there are many point-like particles with strong repulsive forces.

In general one can say that the point-like particles lead to a lubrication effect which reduces the force necessary to shear the system. But one has to be careful not to add too many point-like particles. If the number of point-like particles becomes too large, they build a network that carries most of the load and leads to a strong dilation after the initialization.

6

The concept of soft-particles

As shown in chapter 3, the computing time increases non-linearly with the polydispersity P when simulating extremely polydisperse systems. In this chapter we introduce the concept of soft-particles to reduce the computational costs for polydisperse systems. These meta-particles macroscopically describe the behavior of a polydisperse packing and thus allow to reduce the number of particles in the simulation.

To allow the implementation of these particles into a molecular dynamics, the necessary force law is measured through the interaction of the soft-particle with another soft-particle or a particle described by the Hertz-law.

6.1 The Model

Figure 3.1 shows a two dimensional Apollonian packing with the size distribution following a power law. Between larger particles many smaller particles are arranged in polydisperse packings. The goal of our model is to replace all particles within these local packings with so-called ”soft-particles”. Then, instead of calculating the motion of many small particles, only a much smaller number of soft-particles needs to be considered.

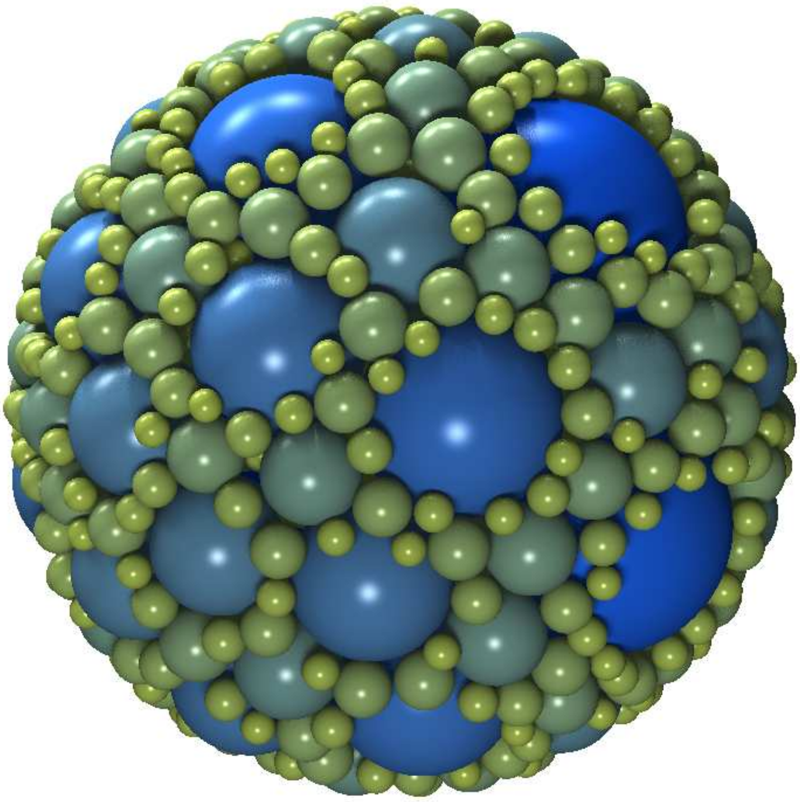

Fig. 6.1: A soft-particle of radius $R_1 = 1.6$cm consisting of a random polydisperse packing with polydispersity $P = 10$.

Figure 6.1 shows a soft-particle consisting of a spherical shell with radius $R_1 = 1.6$cm and the volume $V_S = \frac{4}{3}\pi R_1^3$. It is filled with a polydisperse packing which represents the small particles in a local packing.

The macroscopic behavior is determined by applying an external deformation to the soft-particle and measuring the resistance given by the confined particles. This way, the constitutive law which is needed for the implementation into a molecular dynamics is determined. In the following the inserted particles are referred to as ″grains″ while particles interacting with a soft-particle and which are described by the Hertz-law will be called ßolidparticles.

6.1.1 Generation of the random packing

To create a random polydisperse packing of high volume fraction inside the soft-particle, which follows a truncated power law with an exponent b, a three dimensional version of the hierarchical initialization in section 5.1.3.2 is used.

A separate reservoir is filled with grains generated from the truncated power law. In three dimensions, the volume V_R of all grains in the reservoir is given by

$$V_R = \sum_{i=1}^{n} \frac{4}{3}\pi r_i^3, \tag{6.1}$$

where n is the number of grains in the reservoir and r_i is the radius of the ith grain. The filling stops when $V_R > \beta V_S$. Afterwards the particles in the reservoir are sorted by size and, starting with largest one, each particle gets I trials to find a random spot in the system where it does not overlap with already inserted particles. For the initialization the parameters shown in Table 6.1 are used.

After the insertion of the grains the largest adsorbed grain is chosen and its radius is increased such that it touches its nearest neighbor particle. Doing this for all grains the initial volume fraction increases and a simple contact network is created.

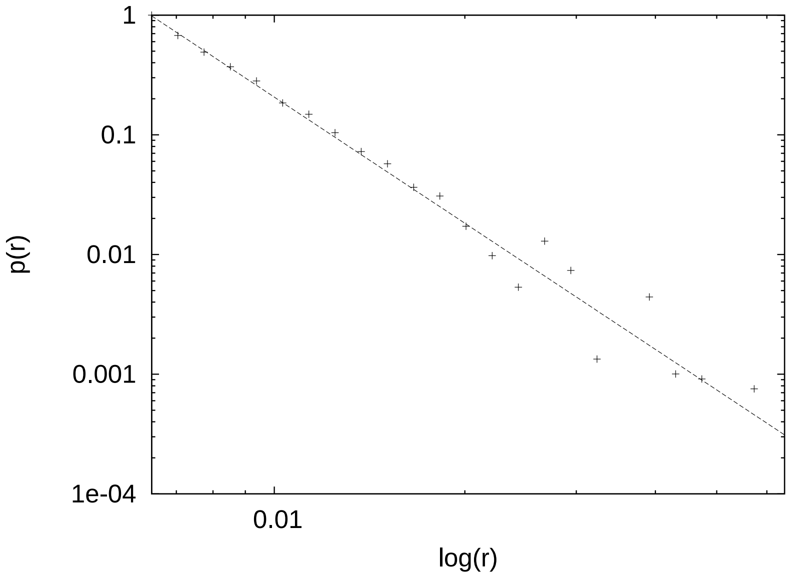

Fig. 6.2: Size distribution for the soft-particle shown in Figure 6.1. The straight line shows the power law with an exponent $b = 3.5$.

Figure 6.1 shows such a randomly generated polydisperse packing for a polydispersity $P = 10$ while in Figure 6.2 the size distribution for the soft-particle is shown. The data can be fitted by a power law with the exponent $b = 3.5$ which is the same exponent as in many real polydisperse systems.

Table 6.1: Parameters for the initialization

Exponent b	3.5
Polydispersity P	10
Maximum radius r_{max}	0.64cm
Minimum radius r_{min}	0.064cm
Soft-particle radius R_1	1.6cm
Filling factor β	1000
Trials I	1000

6.2 Measuring the force law

To calculate the motion of the individual grains in the soft-particle a molecular dynamics is used. The Hertz-law [80]

$$F_n = \frac{\sqrt{R_{12}}\delta_n^{\frac{3}{2}}}{D} \tag{6.2}$$

determines the contact forces in normal direction, while static friction is implemented using the model of Tsuji et al. [83].

$$F_t = \sqrt{R_{12}h}D_t\delta_t; \qquad F_t \leq \mu F_n \tag{6.3}$$

The parameters used in the molecular dynamics are shown in Table 6.2.

Table 6.2: Parameters for the MD

Elastic modulus E	$5 \cdot 10^5 N/m^2$
Poisson ratio ν	0.3
normal constant D	$2.73 \cdot 10^{-6} m^2/N$
tangential constant D_t	$8.84 \cdot 10^{-6} m^2/N$
Friction coefficient μ	0.3

To implement the soft-particles in a molecular dynamics one needs to know the analogs of the two equations above for the soft-particles. This means one needs to know the normal and tangential forces as a function of the normal and tangential deformation. As soft-particles might also interact with themselves one has to determine the constitutive laws for two cases: The interaction of a soft-particle with another soft-particle and the interaction of a soft-particle with a solid particle.

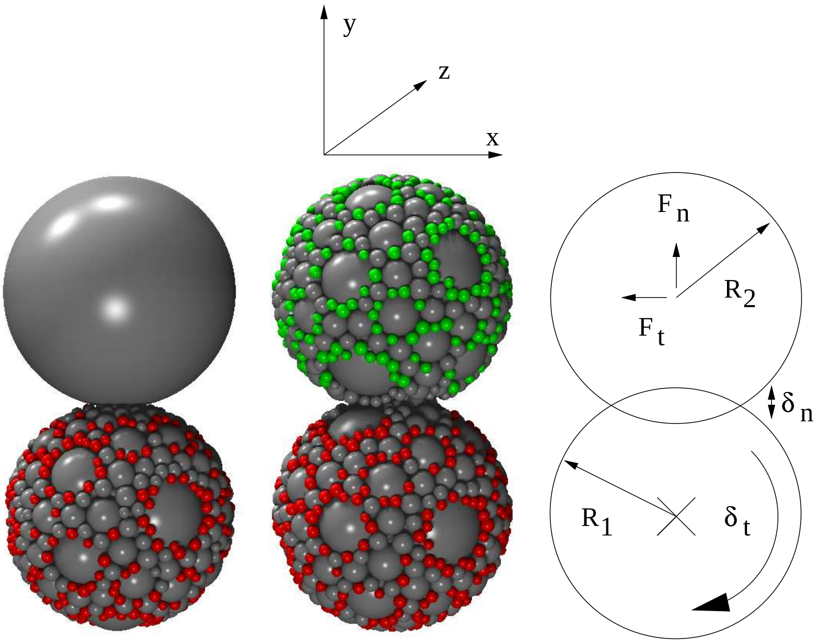

Fig. 6.3: Snapshot of the measurement of the constitutive law. The left picture shows the solid-soft measurement and the middle picture the soft-soft measurement. The red grains are those grains used for the tangential deformation δ_t while the green grains in the soft-soft interaction are used for counterbalance during the tangential measurement.

For the measurement the setup shown in Figure 6.3 is used. On the left side the interaction of a soft-particle with a solid particle of the same size is shown. The middle picture shows the interaction of two soft-particles where for simplicity the second soft-particle is a copy of the first one. Depending on the measurement a soft- or solid particle is placed above the lower soft-particle such that both particles touch but do not overlap. The position of the lower particle is fixed and the upper particle is moved into the lower one with a constant velocity $v = 1$mm/s until the normal deformation δ_n reaches a given value. Now the system relaxes until all grains are at rest and the repulsive force F_n exerted onto the upper particle is measured. As the tangential force law depends on the normal deformation each state used to measure $F_n(\delta_n)$ is reloaded for the tangential measurement. Here all grains in the lower soft-particle with a radius smaller than $1.5r_{min}$ and touching the shell are forced to rotate a certain angle γ. The rotation axis is parallel to the z-axis and goes through the center of the soft-particle. The so enforced tangential deformation δ_t is given by

$$\delta_t = R_1\gamma. \tag{6.4}$$

The grains forced to rotate are colored red in Figure 6.3. As a counter balance in the solid-soft interaction the solid particle is fixed in place and does not rotate. The counter balance in the soft-soft interaction is achieved by fixing the position of the grains in the upper soft-particle which are smaller than $1.5r_{min}$ and touch the shell. These grains are colored green in Figure 6.3. After relaxing the system the tangential force F_t, exerted onto the top particle, is measured. Throughout this chapter, the radius of the lower particle, which always is the smallest of the two, is given by R_1 while the radius of the upper particle is R_2.

For the grains inside the soft-particle, the shell is an impenetrable wall of the same material with no frictional force as it only keeps the grains in a defined volume. Figure 6.4 explains the implementation of the soft-soft interaction. When the two soft-particles move into each other the individual grains inside the two spheres can move freely in the combined space. The boundary is the surface of the two overlapping soft-particles and the normal vector for grains interacting with the boundary is perpendicular to the shell and points to the particle center. This is not well defined when grains interact in the region where the two shells intersect. Here the normal vector points from the shell intersection to the center of the grain.

The most time consuming part during the measurement is the relaxation process. After a short time, most grains are at rest but a few are still moving very slowly making it impossible to conduct a precise measurement. As there exists no rolling friction in the simulation especially small grains rolling on the surfaces of larger ones as described in section 4.1.9 produce an oscillation in the measured force. To speed up the relaxation and to eliminate the rolling of small grains, from time to time, the translational and angular velocity of every grain is set to zero. The time interval between each of these stoppings has to be chosen according to the actual configuration of the system.

6.3 Results

In general the constitutive law of a soft-particle depends on the size ratio $\frac{R_1}{R_2}$ of the interacting particles. Therefore the simulations described

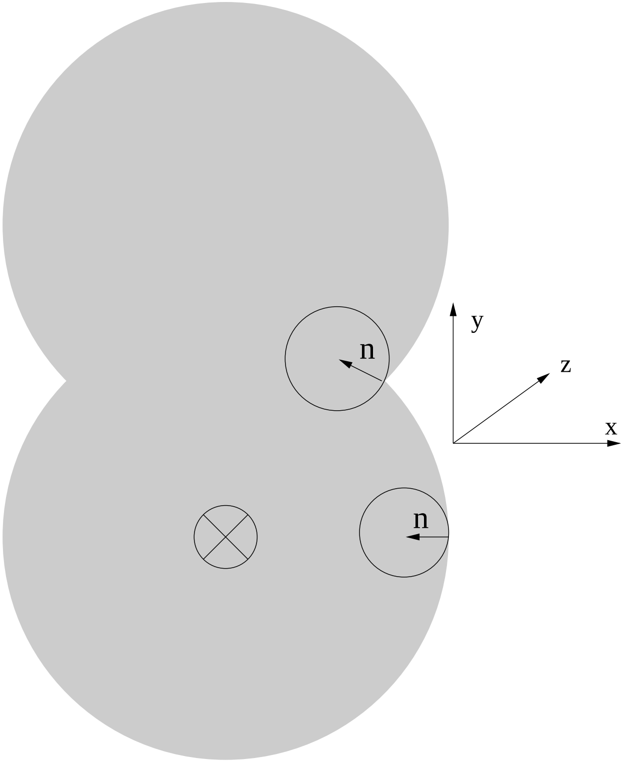

Fig. 6.4: Schematic picture of the soft-soft interaction where the individual grains can move freely inside the combined space of the interacting particles. In general the normal vector for grains interacting with the boundary is perpendicular to the shell and points to the particle center. This is not well defined when grains interact in the region where the two shells intersect. Here the normal vector points from the shell intersection to the center of the grain. The cross in the center of the lower particle depicts the axis around which the red colored grains are rotated to exert a tangential deformation.

above was performed for different radii R_2 while the radius $R_1 = 1.6$cm of the first particle is kept constant. For the solid-soft interaction the radius of the second particle is set to the following three values: $R_2 = 1.6cm, 3.2cm, 16cm$ which corresponds to $\frac{R_1}{R_2} = \frac{1}{1}; \frac{1}{2}; \frac{1}{10}$. For the soft-soft interaction the radius of the second particle is chosen such that $\frac{R_1}{R_2} = \frac{1}{1}; \frac{1}{2}$. In principal any size ratio can be chosen for the soft-soft interaction but the idea is to reduce the number of particles used in a molecular dynamics. When describing a packing of polydispersity $P = 102$, the minimal ratio $\frac{1}{2}$ above is a good compromise as it reduces the number of particles by a factor of 28 while keeping a small polydispersity even for the soft-particles.

During the relaxation process the system was always at rest after three stoppings where the time interval during which the particles move freely was set to $0.3s$. To be sure the system is really relaxed it is stopped six times and after the last stopping we wait at least another 0.3 seconds before conducting any measurement. Ten different simulations where averaged together and for each simulation a different distribution of grains was used and the average initial volume fraction was $\rho_i = 0.761$ which is calculated by

$$\rho_i = \frac{M}{V_S}. \tag{6.5}$$

Here M is the volume of all particles inserted into the soft-particle and V_S is the volume of the soft-particle itself. In the following sections we analyse these measurements and derive a force law which can be used in a combined simulation of solid and soft-particles.

During the measurement the normal deformation for the individual grains inside the soft-particles must not be too large as the Hertz-law itself is only valid for small overlaps. Measurements showed that, for the used parameters, this is guaranteed when $\delta_n < 0.4R_1$. As stated above R_1 is always the smaller radius.

6.3.1 The normal force law

Figure 6.5 shows the repulsive normal force F_n as a function of the normal deformation δ_n for the solid-soft and the soft-soft interaction. In both cases the radii of the interacting spheres are $R_1 = R_2 = 1.6cm$ The upper curve shows the constitutive law for the solid-soft interaction which is stiffer than the soft-soft-interaction shown by the lower curve. Very important is the behavior for small normal deformations. Unlike in the Hertz-law, for normal deformations δ_n smaller then a threshold δ_n', there exist no repulsive force as the soft-particle can still be compactified.

6.3.1.1 Solid-soft interaction

The measurements for the solid-soft interaction are shown in Figure 6.6. Here the normal force F_n is plotted as a function of the normal deformation δ_n for the size ratios $\frac{1}{10}; \frac{1}{2}; \frac{1}{1}$. While the threshold δ_n' stays almost the same (the small change is not visible in the plot) the constitutive law becomes stiffer the larger the interacting solid particle. The reason is that the larger the second particle is, the larger the compression for the same normal deformation which leads to a stronger repulsive force.

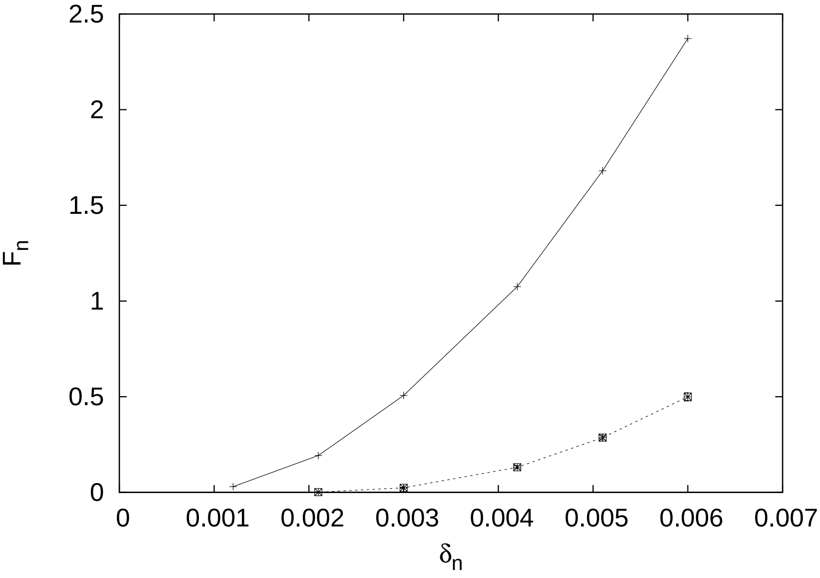

Fig. 6.5: Comparison of the measured constitutive laws in normal direction. The upper curve shows the average constitutive law for the solid-soft interaction while the lower curve shows the soft-soft interaction. In both cases the two interacting particles have the same radius $R_1 = R_2 = 1.6cm$.

When dividing the measurements shown in Figure 6.6 by the reduced radius $R_{12} = \frac{R_1 * R_2}{R_1 + R_2}$ of the contact the data collapse shown in Figure 6.7 is obtained. The resulting curve can be fitted with the following equation:

$$F(\delta_n) = \begin{cases} 0, & 0 < \delta n < \delta'_n \\ a_n \delta_n^{b_n} + c_n, & \delta n \geq \delta'_n \end{cases} \tag{6.6}$$

Here δ'_n is the overlap to which the soft-particle can be compressed without exerting a repulsive force. It is calculated from the fit parameters $a_n = 3.209 \cdot 10^7 N/m$, $b_n = 2.243$ and $c_n = -5.315N$ to $\delta'_n = \frac{-c}{a}^{1/b} =$ 0.947mm.

6.3.1.2 Soft-soft interaction

Figure 6.8 shows the normal force for the soft-soft interaction with the size ratios $\frac{1}{2}$ and $\frac{1}{1}$. When comparing this measurement with the solid-soft interaction two important changes can be seen. First, the threshold δ'_n moves to the right for larger size ratios. Second, the interaction is stiffer for larger size ratios which is contrary to the hard-soft interaction. Both changes can be explained with the void space in the soft particle. As

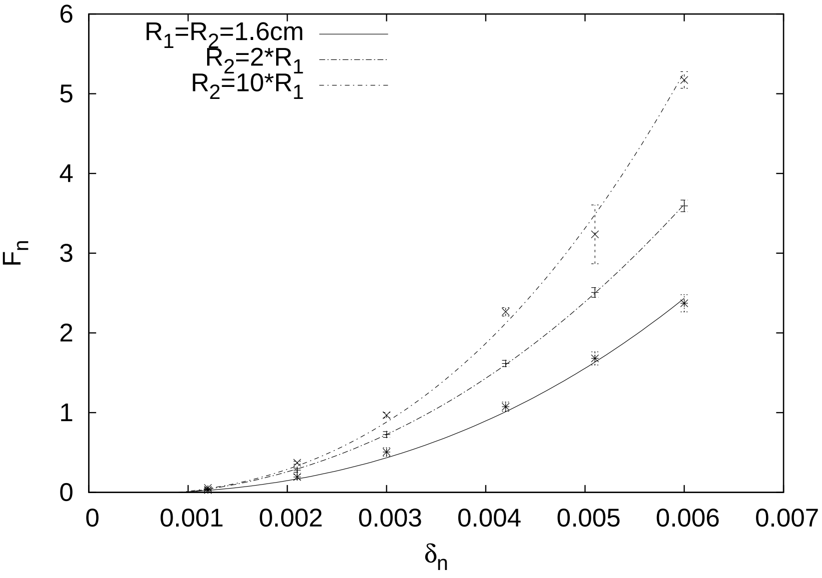

Fig. 6.6: The normal force F_n as a function of the normal deformation δ_n for different size ratios in the solid-soft contact. From top down the size ratios are: $\frac{1}{10}$; $\frac{1}{2}$; $\frac{1}{1}$ with $R_1 = 1.6cm$.

mentioned above the second particle is a copy of the first one scaled to the desired radius R_2. When its radius is set to be twice as large as R_1 the void space is multiplied by a factor 8. Therefore, compared with a contact where both particles have the same radius $R_1 = R_2$, the grains in the first particle have larger voids they can move into and the compression is lower for the same normal deformation. As a consequence the threshold δ'_n increases and the repulsive force decreases.

Again both curves can be fitted by equation 6.6 and for the size ratio $\frac{1}{1}$ one gets: $a_n = 19,613{\cdot}10^6$N/m, $b_n = 3.41$ and $c_n = -0.019$N which gives $\delta'_n = 2.275$mm. For the size ratio $\frac{1}{2}$: $a_n = 1,238 \cdot 10^9$N/m, $b_n = 4.456$ and $c_n = -0.00284$N which gives $\delta'_n = 2.444$mm. The force laws for two interacting particles with a size ratio between 0.5 and 1 are obtained by interpolating between these two curves.

6.3.2 The tangential force law

The tangential force F_t shown in Figure 6.3 in lies in the x-z-plane which is perpendicular to the normal force F_n. Figure 6.9 and Figure 6.10 show the x- and z-component of the tangential force as a function of the tangential deformation δ_t for the solid-soft and the soft-soft interaction. As the tangential force depends on the normal deformation it is plotted for

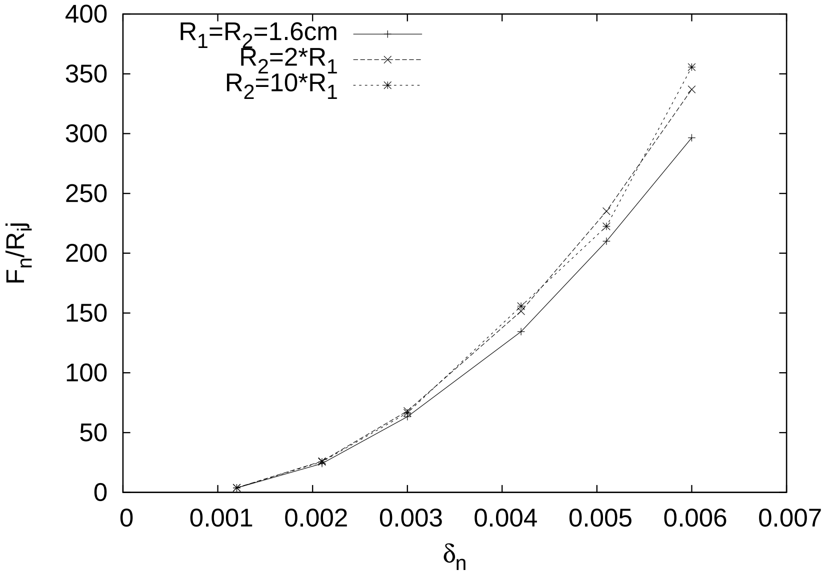

Fig. 6.7: Data collapse of the measurements shown in Figure 6.6. The normal force was divided by the reduced radius $R_{12} = \frac{R_1 * R_2}{R_1 + R_2}$.

different normal deformations. The left plot shows the component in direction of the tangential deformation, the right one shows the perpendicular component.

The x-component increases with a larger normal deformation as it is directly coupled with the tangential deformation. The z-component, which is perpendicular to the direction of deformation, averages out to zero. Thus in the following we refer to the x-component when the tangential force F_t is mentioned.

To implement the measured tangential force law the tangential spring constant and the maximum tangential force the contact can sustain is needed. These two quantities are obtained when fitting the measured tangential force law with the following equation:

$$F_t(\delta_t) = F_{t_{max}} \tanh(s\delta_t) \tag{6.7}$$

Here $F_{t_{max}}$ is the maximum tangential force in the contact and corresponds to the Coulomb force. The tangential spring constant k_t is given by the slope around zero deformation which is

$$\frac{\partial F_t(0)}{\partial \delta_t} = F_{t_{max}} s(1 - \tanh^2(0)) = F_{t_{max}} s. \tag{6.8}$$

In the following the dependence of the parameters $F_{t_{max}}$ and s on the

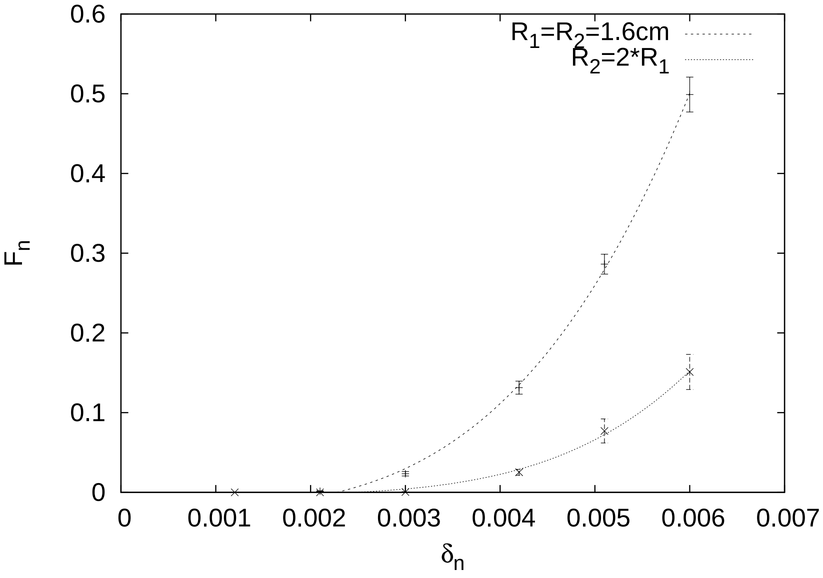

Fig. 6.8: The normal force for the soft-soft interaction. The upper curve shows the size ration $\frac{1}{2}$ the lower curve shows the ratio $\frac{1}{1}$. Here the threshold δ'_n moves to the right for larger size ratios and the interaction is stiffer for larger size ratios which is contrary to the hard-soft interaction.

normal deformation δ_n is determined. For small overlaps fitting the $\tanh$ results in large error bars, therefore these points are omitted.

6.3.2.1 Solid-soft interaction

Figure 6.11 shows the maximum tangential force given by the prefactor Ft_{max} in equation 6.7 as a function of the normal deformation δ_n for the solid-soft interaction. Shown are the measurements for the size ratios $\frac{1}{1}$ and $\frac{1}{10}$. As the values of the measurement fall together the parameter Ft_{max} is set to be equal for all size ratios and the data is fit by the following equation:

$$Ft_{max}(\delta n) = \begin{cases} 0, & 0 < \delta n < \delta'_n \\ a_t \delta_n^{b_t} + c_t, & \delta_n \geq \delta'_n \end{cases} \tag{6.9}$$

As there exists no tangential force without a non-zero normal force, δ'_n is the same threshold as in equation 6.6. From this condition follows

$$c_t = a_t \delta_n'^{b_t}. \tag{6.10}$$

The fit gives the following parameters: $a_t = 1407\text{N/m}$, $b_t = 1.532$ and $c_t = -0.03\text{N}$ while $\delta'_n = 0.947\text{mm}$ as for the normal force law.

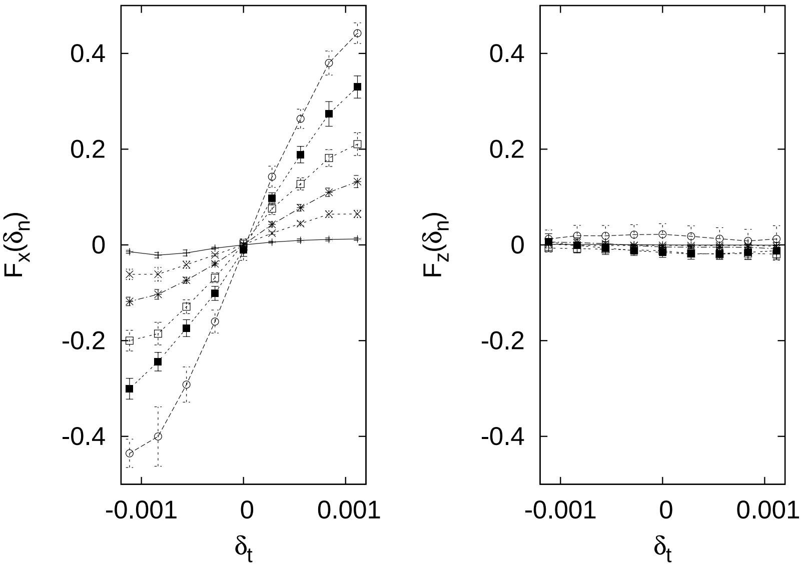

Fig. 6.9: Tangential force in the solid-soft contact as a function of the tangential deformation for different normal deformations. The left plot shows the tangential force in the direction of the tangential deformation which increases with a larger normal deformation. The right plot shows the tangential force in the perpendicular direction, which on average is zero and unaffected by the normal deformation.

Figure 6.12 shows the parameter s for the solid-soft interaction as a function of the normal deformation δ_n. As in Figure 6.11 the measurements for the size ratios $\frac{1}{1}$ and $\frac{1}{10}$ are shown. The parameter s was fit by a constant value, which gives the two horizontal lines in the plot. The fitting values are: $s = 990$ for the size ratio $\frac{1}{1}$ and $s = 1140$ for the size ratio $\frac{1}{10}$. The values for other ratios can be determined by interpolation.

6.3.2.2 Soft-soft interaction

As for the normal measurement the tangential force law for the soft-soft interaction differs from the solid-soft interaction. Figure 6.13 shows the parameter $F_{t_{max}}$ for the soft-soft interaction as a function of the normal deformation δ_n for the size ratios $\frac{1}{1}$ and $\frac{1}{2}$. Unlike in the solid-soft interaction, the measurements are not identical for the different size ratios. Fitting the plot with equation 6.9 gives the following values: $a_t = 1208\text{N/m}$, $b_t = 1.719$, $c_t = -0.034\text{N}$ and $\delta'_n = 2.25\text{mm}$ for the size ratio $\frac{1}{2}$ and $a_t = 15.131\text{kN/m}$, $b_t = 2.409$, $c_t = -0.008\text{N}$ and $\delta'_n = 2.48$ for the size ratio $\frac{1}{1}$ As for the measurement of the normal force the ac-

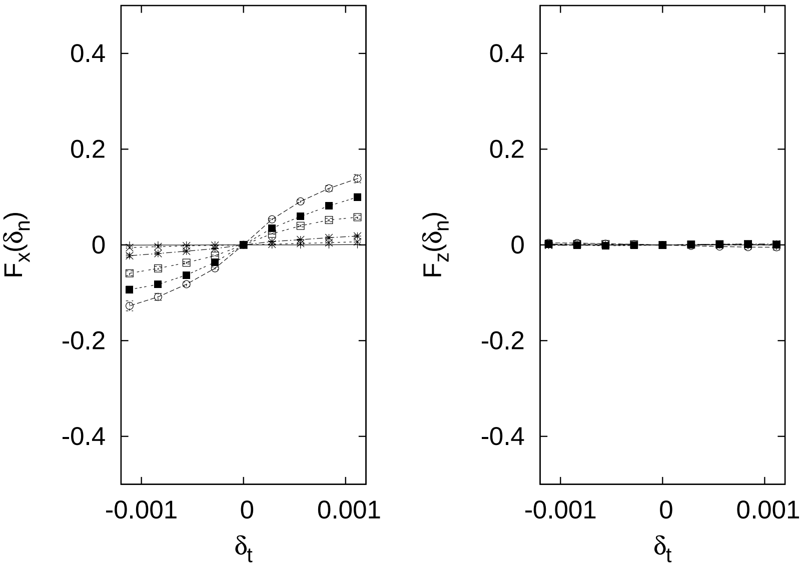

Fig. 6.10: Tangential force in the soft-soft contact as a function of the tangential deformation as shown in Figure 6.9.

tual parameter $F_{t_{max}}$ is determined via interpolation between these two curves.

Figure 6.14 shows the parameter s for the soft-soft interaction versus the normal deformation δ_n for the size ratios $\frac{1}{1}$ and $\frac{1}{2}$. A constant value was used to fit s, which is shown by the horizontal lines. The fitting values are: $s = 1269$ for the size ratio $\frac{1}{2}$ and $s = 1134$ for the size ratio $\frac{1}{1}$.

6.4 Scaling the force law

In the previous sections the constitutive law for the solid-soft and soft-soft interaction of the soft-particles was measured. In all these measurements the radius R_1 of the first particle had the same value $R_1 = 1.6cm$. The radius R_2 of the second particle was adjusted such that one obtains the desired size ratio $\frac{R_1}{R_2} < 1$. To use the measured force laws in a general molecular dynamics one needs to understand how it changes when the size ratio of the particles is increased by the factor α defined by

$$r' = \alpha r. \tag{6.11}$$

Here r describes the radius of a particle in the measurement and r' is the radius of the same particle after scaling it by the factor α. Applying this

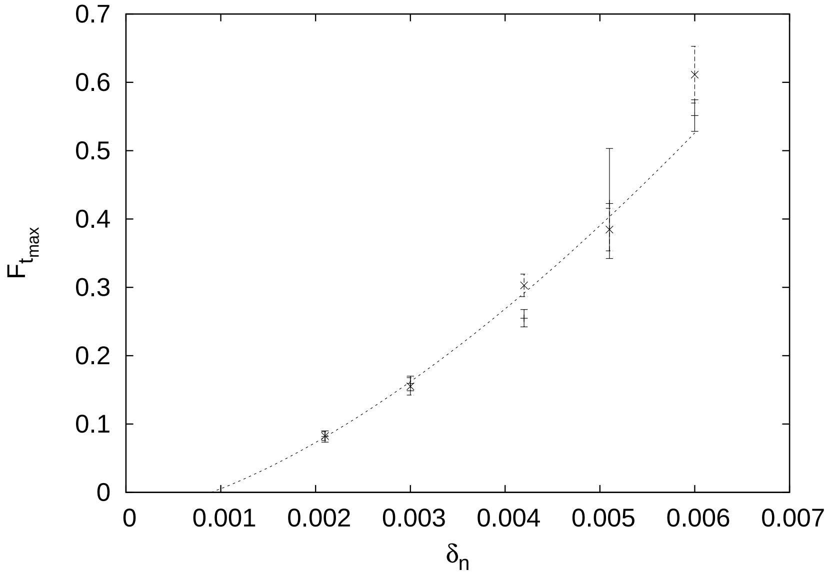

Fig. 6.11: The maximum tangential force given by the prefactor $F_{t_{max}}$ in equation 6.7 as a function of the normal deformation δ_n for the solid-soft interaction. Shown are the measurements for the size ratios $\frac{1}{1}$ and $\frac{1}{10}$. The data was fit by equation 6.9.

equation to all the grains and the shell, in the setup shown in Figure 6.4 changes the volume of the whole system by a factor α^3.

The Hertz-law in equation 4.13, describing the interaction of the individual grains in the polydisperse packing, helps to understand how the measured force law scales with α. Rewriting this equation in terms of the relative normal deformation $\Delta n = \delta_n / R_{12}$ the normal interaction between two arbitrary particles becomes

$$F_n(\Delta n) = \frac{R_{12}^2 \Delta n^{3/2}}{D}. \tag{6.12}$$

Scaling both particles by the factor α does not change the relative normal deformation but a new reduced radius

$$R'_{12} = \alpha R_{12} \tag{6.13}$$

is obtained. Therefore the scaled normal force F'_n can be written as

$$F'_n = \alpha^2 F_n. \tag{6.14}$$

Following this argument it can be shown that the tangential force follows the same scaling law. For verification the normal and tangential interaction between an solid and a soft particle was measured. We performed

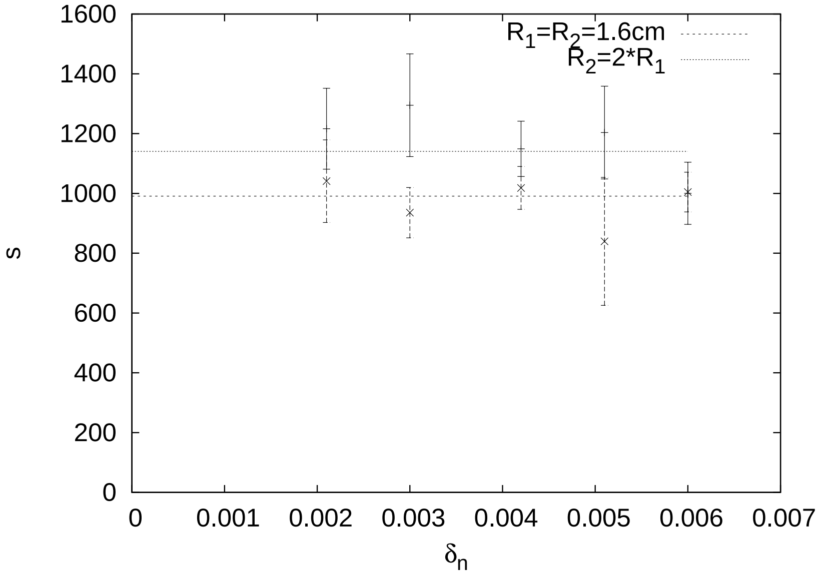

Fig. 6.12: The parameter $F_{t_{max}}$ for the solid-soft interaction as a function of the normal deformation δ_n. The upper curve shows the measurement for a size ratio $\frac{1}{10}$, the lower plot for a size ratio $\frac{1}{1}$.

two measurements: One with $R_1 = R_2 = 1.6\text{cm}$, the second one with $R_1 = R_2 = 3.2\text{cm}$ corresponding to a scaling factor $\alpha = 2$.

Figure 6.15 shows the resulting force law for the normal and the tangential interaction. Here the measured force is divided by R_{12}^2 and plotted as a function of the relative normal deformation $\Delta n = \delta_n / R_{12}$. In both cases the curves exactly fall on top of each other proving the scaling behavior.

6.5 Velocity dependence of the force law

In the previous discussion a constant velocity $v = 1\text{mm/s}$ was used when deforming the soft-particles. In general such a soft-particle can experience different compression velocities in a MD. Therefore simulations with four different velocities were performed. As shown in Figure 6.16 the measured normal force lies within the error bars for all four velocities. In the plot the points for lower velocity are shifted to the right for a better visualization. The same behavior was found for the tangential measurement and thus any velocity dependence of the constitutive law is ignored.

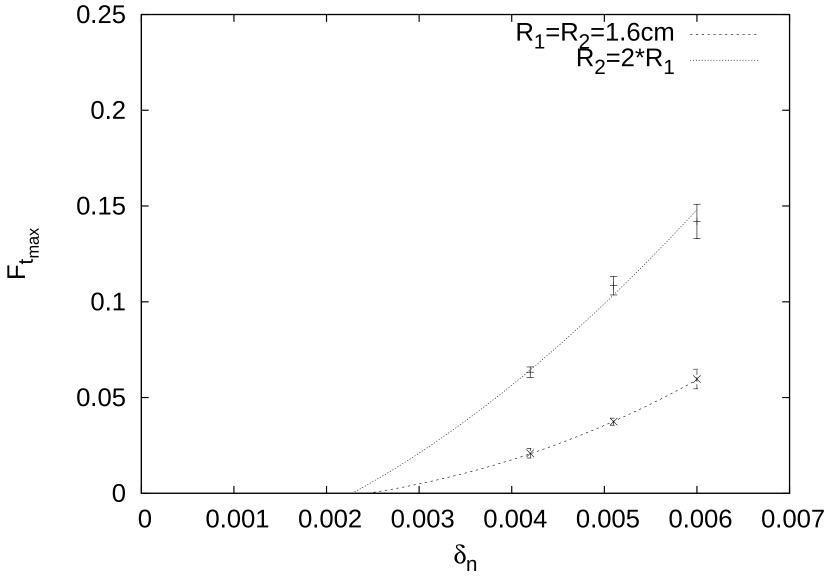

Fig. 6.13: The parameter Ft_{max} for the soft-soft interaction as a function of the normal deformation δ_n. The upper curve shows the measurement for the size ration $\frac{1}{2}$ the lower curve shows the size ration $\frac{1}{1}$.

6.6 Conclusion

In this chapter we introduced the concept of the soft-particles which allows a macroscopic description of the behavior of a polydisperse packing which is given by a normal and a tangential force law. The findings of the measurements for the solid-soft and soft-soft interaction can be summarized in the following equations.

The general normal force law is given by

$$F(\delta_n) = \begin{cases} 0, & 0 < \delta_n < \delta_n' \\ \alpha(a_n \delta_n^{b_n} + c_n), & \delta_n \geq \delta_n' \end{cases} . \tag{6.15}$$

Here δ_n is the imposed normal deformation, δ_n' is the threshold until which the soft-particle can be compressed before measuring any repulsive force and a_n, b_n and c_n are fit parameters which are different for the two contact types. As the measurement in general is not performed on the scale at which the force law is implemented, the prefactor

$$\alpha = \left(\frac{R_{12}'}{R_{12}} \right) \tag{6.16}$$

describes the scaling of the force-law. $R_{12} = \frac{R_1 R_2}{R_1 + R_2}$ is the reduced radius during the measurement and R_{12}' is the reduced radius of the scaled

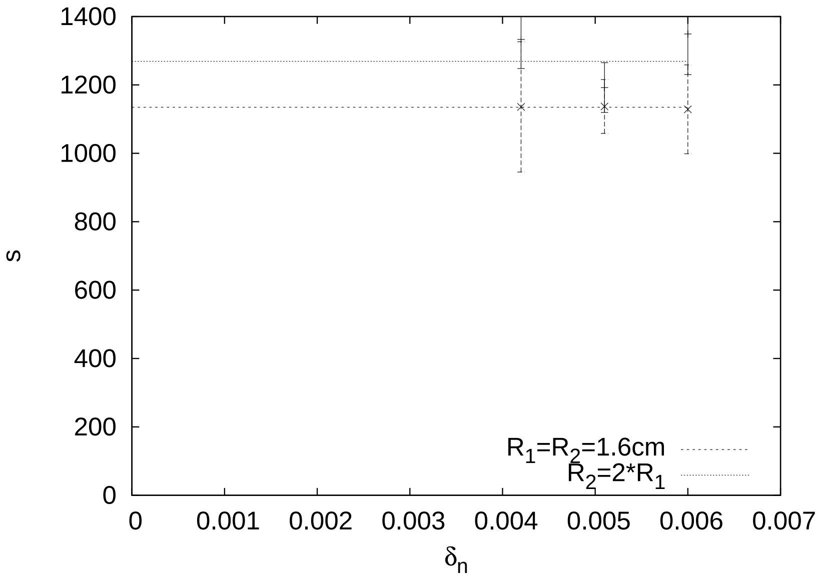

Fig. 6.14: The parameter s for the soft-soft interaction as a function of the normal deformation δ_n. The upper curve shows the measurement for a size ratio $\frac{1}{2}$, the lower plot for a size ratio $\frac{1}{1}$.

system.

The tangential force law

$$F_t(\delta_n, \delta_t) = F_{t_{max}}(\delta_n) \cdot \tanh(s\delta_t) \tag{6.17}$$

depends on the normal deformation δ_n and the tangential deformation δ_t. The parameter s is a constant and

$$F_{t_{max}}(\delta n) = \begin{cases} 0, & 0 < \delta n < \delta'_n \\ \alpha(a_t\delta_n^{b_t} + a_t\delta_n'^{b_t}), & \delta_n \geq \delta'_n \end{cases} \tag{6.18}$$

is the maximum tangential force the contact can sustain before sliding. The slope $F_{t_{max}}s$ at zero tangential deformation gives the stiffness of the tangential spring.

Using these force-laws to describe the smaller particles in a polydisperse packing the number of simulated particles decreases and the time step can be set to a larger value. For the shear experiment in the next chapter, this reduces the computing time by more than a factor 100.

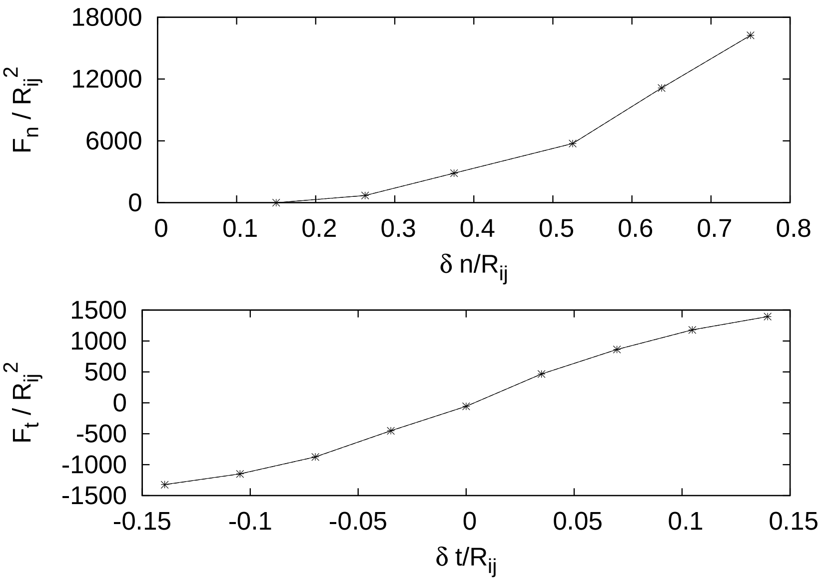

Fig. 6.15: Examples of normal and tangential measurement of the solid-soft interaction. Plotted is the measured force divided by R_{12}^2 versus the relative normal deformation $\Delta n = \delta_n / R_{12}$. One measurement was performed with $R_1 = R_2 = 1.6\text{cm}$ and a second one with $R_1 = R_2 = 3.2\text{cm}$ giving a scaling factor $\alpha = 2$. The measurements fall exactly on top of each other. The upper plot shows the normal force law while the lower plot shows the tangential measurement for a relative normal deformation $\delta_t = 6.25\text{mm}$.

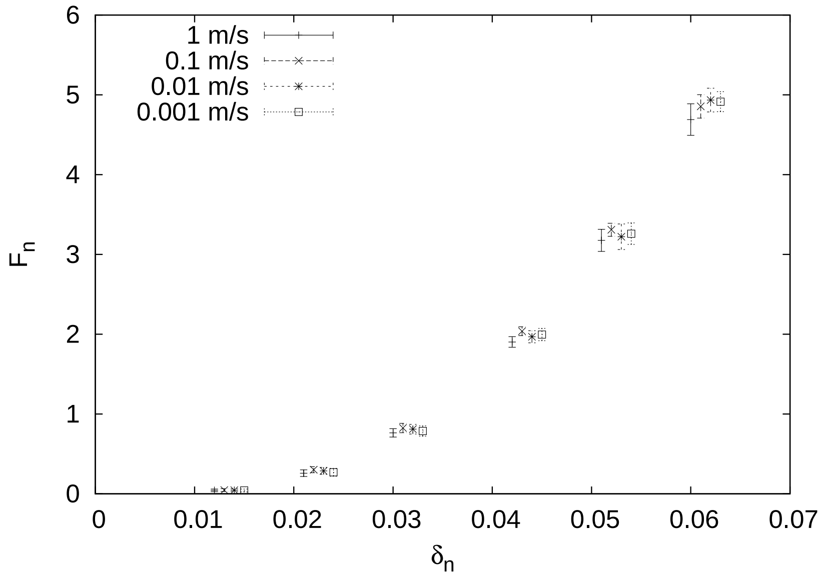

Fig. 6.16: Repulsive normal force versus the normal deformation for a solid-soft interaction. Four different velocities were used for the deformation. For all measurements the results lie within the error bars.

7 Shearing behavior of soft-particles

In this chapter we use the concept of soft-particles introduced in chapter 6 to investigate the shear behavior of three dimensional polydisperse packings. As we will see, this concept reduces the computation time by more than a factor of 100 when compared to a simulation without soft-particles. For comparison, systems without soft-particles and thus of smaller polydispersity are also analyzed.

Before discussing the results from the shear experiments the changes in the setup of the shear cell, compared with the two dimensional shear cell in chapter 5, are explained.

7.1 The shear cell

Figure 7.1 shows a snapshot of the three dimensional shear cell. Periodic boundary conditions are applied, therefore particles leaving the cell through one of the four open faces, will reenter the cell through the opposite face. For each of these particles there exists a copy at the opposite face. These shadow particles are colored blue while the particles glued to the lid are colored green; all other particles are red. For better visualization only half of the lid and half of the shadow particles are displayed. The length of the cell in all three directions is $l = 10$cm and its volume is

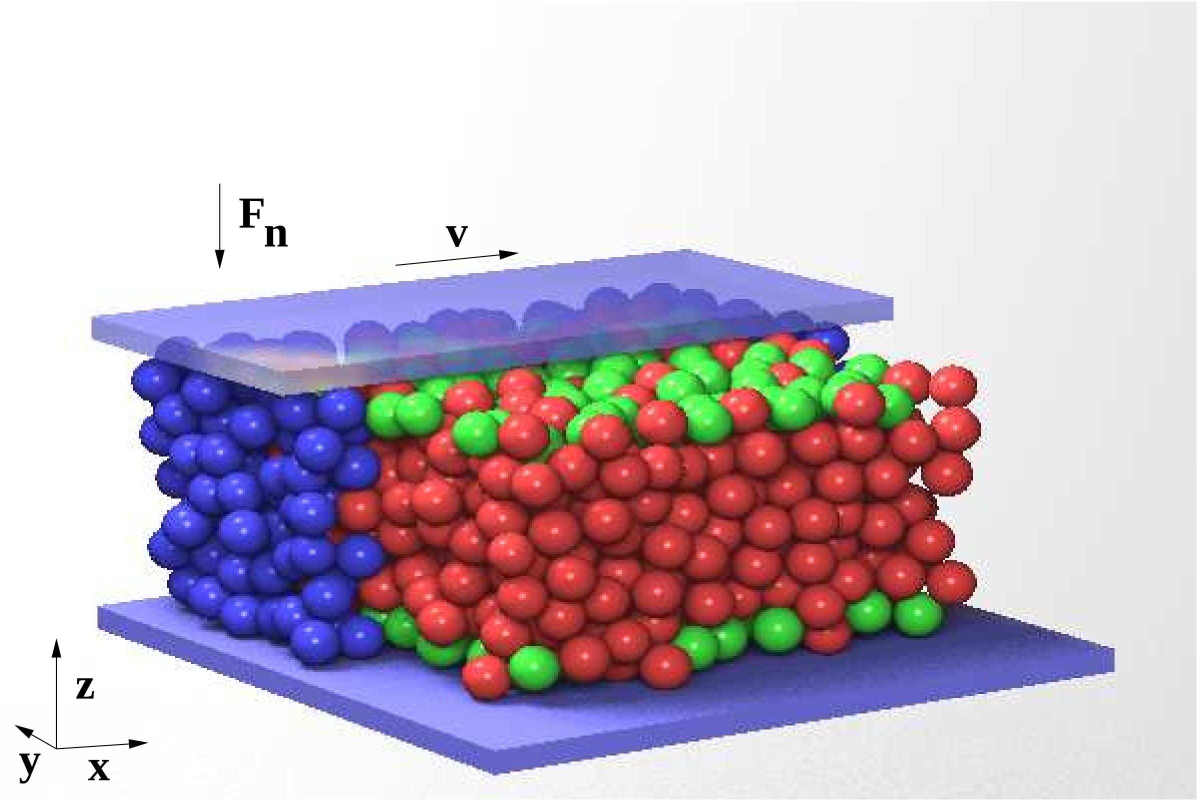

Fig. 7.1: The three dimensional shear cell with periodic boundary conditions. The shadow particles are colored blue while the particles glued to the lid are colored green. All other particles are red. For better visualization only half of the lid and half of the shadow particles are displayed. The length of the cell in all three directions is $l = 10$cm with a volume $V_c = l^3$ and the actual height of the lid is given by $h(t)$. While shearing the lid with the constant velocity v into the x-direction a constant normal force F_N is exerted onto the lid.

$V_c = l^3$ while the actual height of the lid is given by $h(t)$. While shearing the lid with the constant velocity v into the x-direction a constant normal force F_N is exerted onto the lid.

The bottom wall is fixed at all times as its mass is set to infinite. The mass of the top wall or lidïs set to 10^{-5} kg which is less or equal than 0.2 times the mass of all particles in the shear cell and allows it to move up and down. In all simulations gravity is turned off and the normal force is set to $F_N = 1N$, which corresponds to the force it would feel under gravity.

For all simulations discussed in this chapter a molecular dynamics with an elastic modulus $E = 5 \cdot 10^5 N/m^2$, the poisson-ratio $\nu = 0.3$ and the friction coefficient $\mu = 0.3$ was used. The material density is set to $10^3 kg/m^3$ and four different systems were simulated. System A with the polydispersity $P = 1.11$ and $r_{max} = 0.005$m, two polydisperse ($P = 10$) systems B and C with $r_{max} = 0.015$m and $r_{max} = 0.025$m respectively as well as a mixed system D of polydispersity $P = 100$ where the size of the "normal" particles range from $r_{max} = 0.025$m to $r_{max}/g = 0.0025$m and the soft-particle size ranges from $r_{s_{max}} = r_{max}/g$ to $r_{s_{min}} = r_{max}/(2g)$. As will be shown in the next section, the factor g determines the size of the particles replaced by soft-particles and is set to $g = 10$.

7.1.1 Initialization of the shear cell

For the initialization of a system without soft-particles the hierarchical method described in section 5.1.3.2 is used. The reservoir is filled with particles generated from the truncated power law in equation 3.1 and the filling stops when $V_R > \beta V_C$. Then, starting with the largest one each particle gets a maximum of I trials to randomly be inserted into the cell.

For a mixed system of solid and soft-particles this method is extended. Figure 7.2 schematically shows the size distribution of such a system. The factor g divides the size distribution ranging form r_{min} to r_{max} into two parts. The shaded grey area ranges from r_{min} to r_{max}/g and contains all particles which will be replaced by soft-particles. The second part from r_{max}/g to r_{max} contains the solid particles described by the Hertz-law.

The solid particles are hierarchically inserted but this method is too inefficient for the soft-particles as more trials I are needed to find a free spot if the system gets denser. Even if a free place is found, the void space between the particles, due to the randomness of the method, is not ideally filled. Therefore the following algorithm for the soft-particles is used.

One randomly picks an already inserted sphere and three of its neighbors. From the coordinates of these four spheres the position and size of a fifth sphere is calculated. This sphere touches the other four and thus ideally fills the intermediate space. To calculate the position $\vec{x}$ and radius r of the new particle the following set of equations needs to be solved.

$$|\vec{x_i} - \vec{x}| = r_i + r, \qquad i = 1..4 \tag{7.1}$$

Here $\vec{x_i}$ and r_i are the positions and radii of the four particles defining the fifth one. A detailed solution is given in the appendix.

The new particle is checked if it overlaps with an already existing one and it is made sure the calculated radius lies in the size range of the

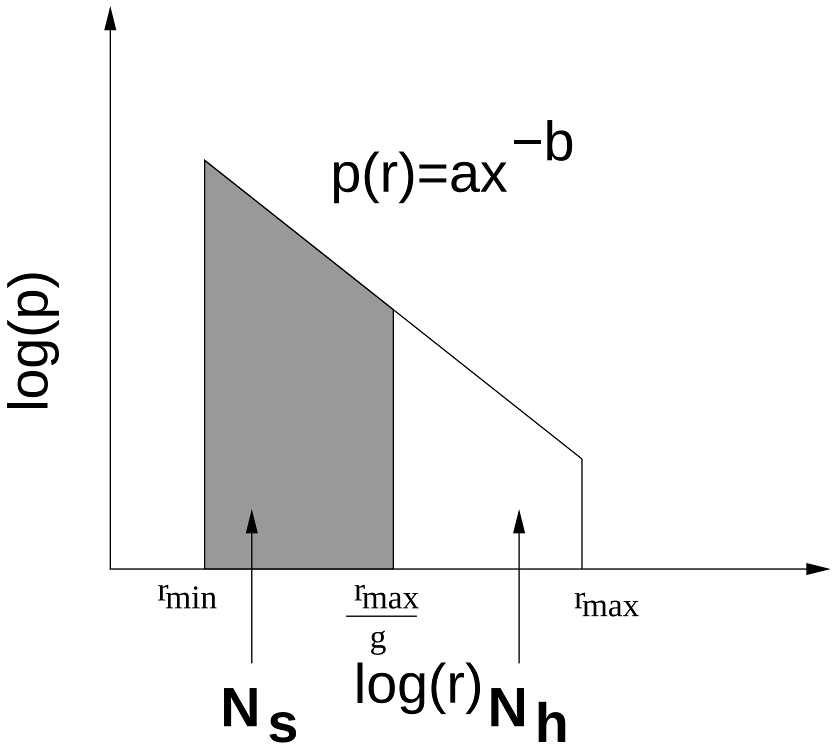

Fig. 7.2: Log-log plot of the truncated power law ranging from r_{min} to r_{max}. The number of particles of a polydisperse system is given by the area under the truncated power law. The factor g divides the interval $[r_{min} : r_{max}]$ into two parts. The first part ranging from r_{min} to r_{max}/g contains all particles which are described by the soft-particle. The second part is described by the grains.

soft-particles. As stated in chapter 6 the minimum size ratio for the soft-soft interaction is $\frac{1}{2}$. Therefore the maximum radius for a soft-particle is set to $\frac{r_{max}}{g}$ and the minimum radius to $\frac{r_{max}}{2g}$. If all these conditions are fulfilled the particle is inserted and marked as a soft-particle, otherwise it is discarded. During this process any combination of hard and soft particles can be chosen to be the four particles from which the position of the new particle is calculated.

This insertion continuous until the volume V_s of the inserted soft-particles correspond to the volume V of all particles in the grey shaded area of the power law in Figure 7.2. As the grains in the soft-particles do not completely fill space V_s is given by

$$V_s = \frac{V}{\rho_s}. \tag{7.2}$$

Here ρ_s is the initial volume fraction of the soft particles and V is calculated from our power law to

$$V = \int_{r_{min}}^{r_{max}/g} \left(\frac{4}{3}\pi r^3\right)\left(ar^{-b}\right) \quad dr = \frac{a4\pi}{3(4-b)}\left[r^{4-b}\right]_{r_{min}}^{r_{max}/g} . \qquad (7.3)$$

7.1.2 Compaction and shearing

After the initialization the normal force F_N is applied onto the lid which compactifies the system and comes to rest at the reference height h_0 from which the shearing starts. To reach high initial volume fractions the friction coefficient is set to $\mu = 0$ during the compaction. After the compaction it is reset to $\mu = 0.3$ and, as in chapter 5, a layer of particles is glued onto the lid and the bottom. These are the green particles in Figure 7.1. In system A all particles are of comparable size. Therefore all those particles touching lid or bottom are fixed while for the systems with a larger polydispersity only particles which are smaller than twice the smallest radius are fixed.

The lid is forced to shear at a constant velocity v in the x-direction while the movement in the y-direction is suppressed. In the vertical direction the lid is allowed to move freely and is only restricted by the normal force F_n.

7.2 Results

Table 7.1 shows the average number of particles and the volume fraction of the four systems after the initialization. The parameters of system C and D are chosen such that they have the same reference height h_0 and the same maximum radius $r_{max} = 0.025$m. For system B the maximum radius was set to $r_{max} = 0.015$m to analyze how the behavior is influenced if only the number of particles changes but other parameters like shear velocity and initial volume fraction stay the same. For all systems shearing experiments with velocities from $v = 0.1$m/s to $v = 1$m/s were performed where the shearing always started from the same initial configuration. Note that when simulating system D without soft-particles about $2 \cdot 10^5$ particles are needed.

Figure 7.3 shows the saturation dilatancy d_s as a function of the shear rate v/h_0. In all cases the dilatancy increases with the shear rate and, for

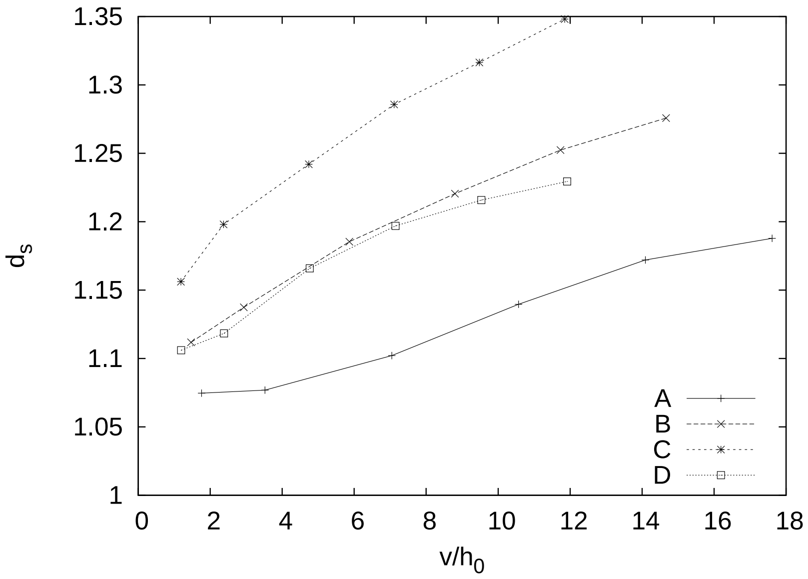

Fig. 7.3: Saturation dilatancy d_s as a function of the shear rate v/h_0. In all simulations the dilatancy increases with the shear rate and, for systems without point-like particles, is larger for more polydisperse systems.

Table 7.1: Initial values of the different simulated systems

System	P	average number of particles	volume fraction
A	$P = 1.11$	795	0.6275
B	$P = 10$	909	0.7333
C	$P = 10$	3481	0.7333
D	$P = 100$	7228	0.7788

systems without point-like particles, is larger for more polydisperse systems. System B and C show that an increase of the particle number for a constant polydispersity reduces the dilatancy as do the soft-particles.

Figure 7.4 shows the angle of dilatancy Ψ as a function of the shear rate v/h_0. The systems B and C show a larger angle of dilatancy than system A while, compared with B and C, the soft-particles reduce the value. Interesting is the decrease of the angle of dilatancy for larger shear rates. A small set of test runs was performed for a polydispersity $P = 1.11$ where the normal force and the E-modulus were increased by a factor of 100. Here a monotonic increase of Ψ with the shear rate was observed. We did not test this for the very polydisperse systems as the necessary time step reduction implied by the larger E-modulus results in to long computation times. Nevertheless, judging from the simulations for system

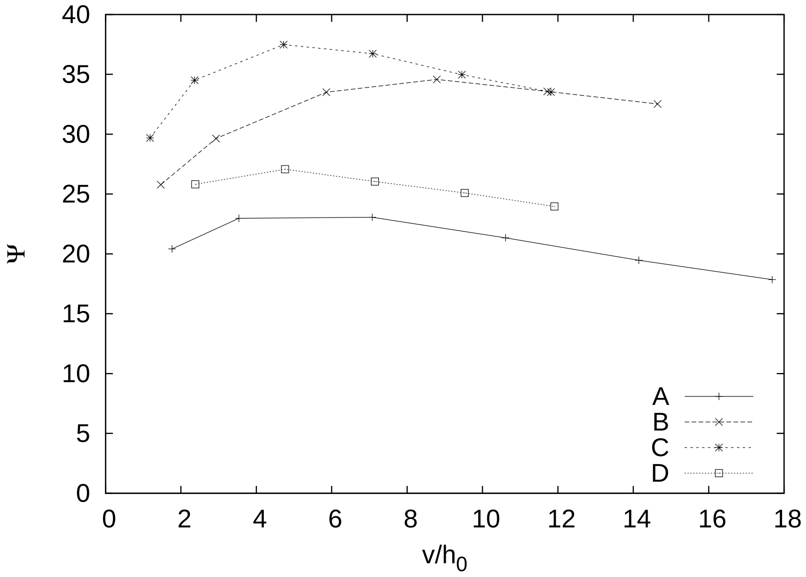

Fig. 7.4: The angle of dilatancy Ψ as a function of the shear rate v/h_0. The systems B and C show a larger angle of dilatancy than system A while, compared with B and C, the soft-particles reduce the value.

A, we expect this behavior to be related to the small value of E.

The last parameter is the ratio between the shear force F_s and the normal force F_n. This ratio is comparable to the friction coefficient which was set to $\mu = 0.3$. Figure 7.5 shows this ratio as a function of the shear rate v/h_0. All values differ at maximum 60% from the imposed friction coefficient and compared with the system A, the systems with a larger polydispersity shows a stronger ratio. Again the soft particles, due to their softer force law, reduce this ratio when compared it with the polydisperse system consisting of only solid particles. As for the dilatancy C and D show comparable results.

7.3 Summary

In this chapter we used the concept of the soft-particles to analyze the shear behavior of a system with polydispersity $P = 100$ and compared the measurements with the results for a system of polydispersity $P = 1.11$ which was simulated without soft-particles. We could show that for the more polydisperse system the dilatancy, the angle of dilation and the measured friction coefficient are larger while compared with a system of polydispersity $P = 10$ they are either of comparable size or smaller.

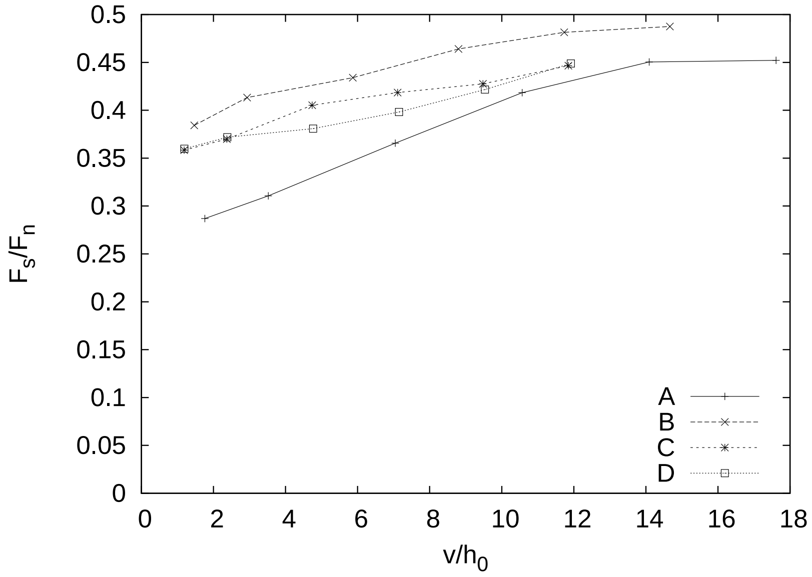

Fig. 7.5: The shearing force F_s divided by the normal force F_n as a function of the shear rate v/h_0. Compared with the system A all simulations with a larger polydispersity show a stronger shear resistance.

The great advantage of the concept of soft-particles is that, instead of directly simulating $2 \cdot 10^5$ particles it reduces this number to about 7000 particles. Additionally the time step could be chosen larger than without soft-particles.

As discussed in chapter 3, the time step decreases linearly with the particle size and in a simulation without soft-particles the smallest particle would have been five times smaller than the smallest particle used in this chapter. Thus, taking into account that the number of particles is reduced by a factor of $\frac{2 \cdot 10^5}{7000} \approx 28$ the computational effort was reduced by more than a factor of 100.

8

The self-consistent model

Simulating polydisperse systems with the model of the soft-particles, introduced in chapter 6, substantially reduces the computing time. For the system with a polydispersity of 100, discussed in chapter 7, the number of particles was reduced by a factor 28 while the time step could be chosen five times larger than without soft-particles. Thus, the computational costs was reduced by more than a factor of 100. Nevertheless the dependence of the computation time on the polydispersity, as described in chapter 3, remains when the polydispersity is increased.

In this chapter we extend the concept of the soft-particles to a self-consistent model which allows the simulation of granular media of any polydispersity. This is accomplished through an iterative measurement of the repulsive force-law while the number of particles in the system remains constant.

8.1 The model

As mentioned in chapter 3, the size distribution of extremely polydisperse materials ranges over several magnitudes and the smaller particles are contained in local packings between larger particles. Zooming into such a local packing one finds, due to the fractal nature of the polydisperse material, other, even smaller, local packings.

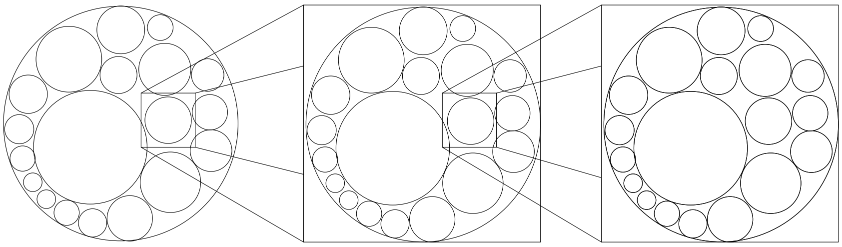

Fig. 8.1: Schematic picture of the self-consistent model. The soft-particle is filled with grains and small soft-particles. Inside such a small soft-particle a similar configuration consisting of grains and small soft-particles is found.

We want to capture this fractal nature with a self-consistent model shown in Figure 8.1. As in chapter 6, the soft-particle is filled with grains which follow a truncated power law. To extend the size range of the model, small soft-particles are inserted describing particles smaller than the smallest grain. Inside such a soft-particle a similar configuration consisting of grains and small soft-particles is found.

The constitutive law of these self-consistent soft-particles is determined in an iterative process of q steps. After the qth iteration the constitutive law describes a polydisperse system with the size distribution shown in Figure 8.2. The particle size ranges from r_{max}/g^q to r_{max} and the polydispersity is given by $P = g^q$. The factor g defines the binning of the power law and after each iteration the size distribution is extended by one bin. The iteration itself works like the following.

In the first step ($q = 1$) the soft-particle is only filled with grains such that the resulting packing has a polydispersity $P = g$. Thus the covered size distribution of the measurement corresponds to the grey area in Figure 8.2.

In the next step ($q = 2$) the previously measured force law is used to describe the interaction of the grains with small soft-particles. For the new measurement the grains are inserted at the same position as in the previous step and afterwards small soft-particles are inserted into the remaining voids. The polydispersity of the inserted soft-particles and the grains is $P = g$ and thus the measurement describes the behavior of a polydisperse packing with $P = g^2$. The size distribution corresponds to the grey and the adjacent white bin in the picture.

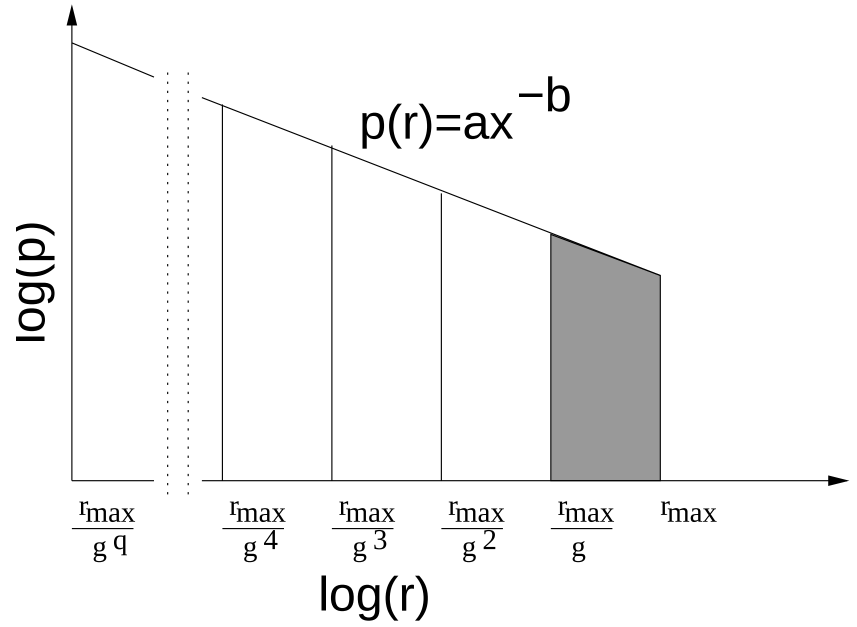

Fig. 8.2: The size distribution of the self-consistent soft-particle after q iterations follows a truncated power law. The factor g defines the binning of the power law and after each step of the iteration the size distribution covered by the measured force law is extended by one bin.

Repeating the second step until q iterations were performed gives a force law which describes the behavior of a packing of polydispersity $P = g^q$.

8.1.1 Initializing the self-consistent soft-particle

For the initialization of the self-consistent soft-particle the same method as in chapter 7 is used. The grains are inserted hierarchically and then, using the apollonian insertion (see section 10.1), the small soft-particles are inserted until their summed volume V_s fulfills the condition $V_s = V_S g^{b-4}$. Here V_S is the volume of the soft-particle into which the particles are inserted. A detailed description of the derivation of V_s is given in the appendix.

The condition above is very interesting as it tells us that in the self-consistent packing the volume occupied by soft-particles is independent of their density. It only depends on the volume of the enclosing soft-particle and the factor g defining the binning of the size distribution. Therefore the self-consistent model can describe a polydisperse packing of any desired volume fraction

To account for the mass added in each iteration the initial volume fraction of the soft-particles is chosen such that the mass of all soft-particles equals the mass of all particles smaller than r_{max}/g. This corresponds to the white area in the power law. For n inserted soft-particles, the initial volume fraction is calculated via

$$\rho_i = \frac{\int_{r_{max}/g^q}^{r_{max}/g} ar^{-b}\frac{4}{3}\pi r^3 dr}{\sum_{i=0}^{n}\frac{4}{3}\pi r_i^3} = \frac{\int_{r_{max}/g^q}^{r_{max}/g} ar^{-b}\frac{4}{3}\pi r^3 dr}{V_s}. \tag{8.1}$$

The nominator describes the mass of the added soft-particles while the denominator describes their summed up volume.

8.2 The force law of the soft-particles

In chapter 6 the repulsive force law was described as a function of the normal deformation δn with the normal force being zero when $\delta_n < \delta_n'$. This description is problematic for the self-consistent model as the threshold δ_n' depends on the density of the soft-particle. In the following a description of the force-law independent of the density is derived.

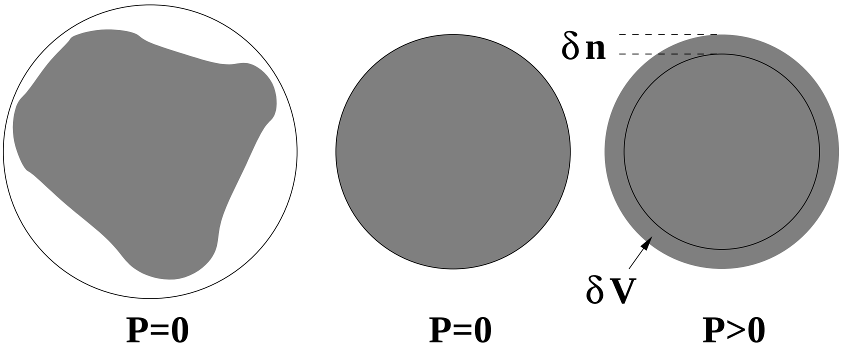

Fig. 8.3: The polydisperse material inserted into a soft-particle is displayed as the grey area. When the radius of the soft-particle shrinks this material adjusts its shape and when overlapping a pressure is exerted onto the shell.

For this description, a closer look at the behavior of the contents of the soft-particle is necessary. The density of the soft-particle is given by

$$\rho = M/V_a \tag{8.2}$$

where M is the mass of all inserted particles and V_a the available volume. For a non-overlapping soft-particle this is the volume of the soft-particle itself.

As shown in Figure 8.3, the inserted polydisperse packing can be envisioned somewhat like a fluid as it has a fixed volume and can adjust to any shape. The left picture displays a soft-particle partially filled with a polydisperse material which corresponds to the grey area and the enclosing shell, displayed as the solid line, does not feel any pressure. Reducing the radius such that the volume of the soft-particle is the same as the volume of the polydisperse material gives the middle picture. The pressure on the shell is still zero and the material perfectly adjusts to the shell. The density in this situation will be called the critical density ρ_c as the shell feels a pressure when the radius is reduced further. As shown in the right picture, this pressure is related to the normal deformation δ_n. We will see later, that the volume δV overlapping with the shell is better suited for the description of soft-particle interaction. In Figure 8.3, δV is the grey region outside the shell.

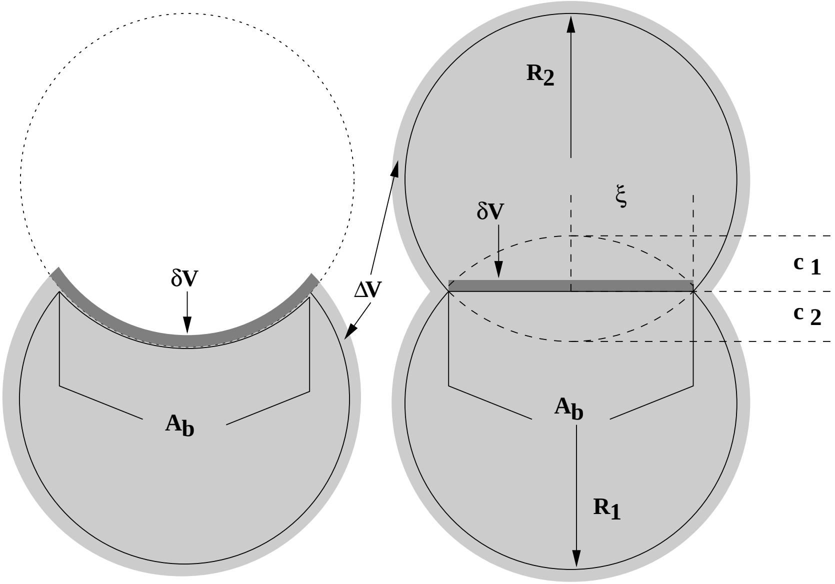

Fig. 8.4: The measurement for a normal deformation $\delta_n = c_1 + c_2$. The left picture shows the solid-soft interaction. A_b is the surface of the solid particle pushed into the soft-particle and the enclosing area, which corresponds to the solid line, is denoted A_{total}. The overlapping volume δ_V is the dark grey area and ΔV corresponds to the grey area outside A_{total}. The right picture shows the soft-soft interaction where A_b is given by the circular area of radius ξ between the two sphere caps.

For two interacting solid particles, δV corresponds to the volume of the two sphere caps defined by the overlap δ_n. For soft-particles the situation is more complicated. Due to the normal deformation, the available volume V_a for their contents is reduced and the volume fraction increases. At the critical volume fraction ρ_c, the soft-particle cannot be compacted anymore without measuring a repulsive force. The left picture in Figure 8.4 shows the solid-soft interaction with a normal deformation $\delta_n = c_1 + c_2$. A_b is the surface of the solid particle pushed into the soft-particle and the enclosing area, which corresponds to the solid line, is denoted A_{total}. The overlapping volume δ_V which gives rise to the repulsive normal force corresponds to the dark grey area. and is a fraction of the volume ΔV which corresponds to the grey area outside the boundary A_{total}.

The right picture shows the situation for the soft-soft interaction. Here the inserted grains can move freely inside the combined volume of both soft-particles and A_b is given by the circular area of radius ξ between the two sphere caps at which the two particles interact. Using the assumption of the fluid like behavior one can argue that the pressure onto this surface is the same as onto the shell. Thus for both contacts follows $\delta V = \Delta V A_b / A_{total}$. Using the derivation in the appendix, δV is given by

$$\delta V = \begin{cases} \Delta V \frac{R_1 c_1}{2R_1^2 - R_1 c_1 + R_2 c_2} & \text{solid-soft} \\ \Delta V \frac{2R_1 c_1 - c_1^2}{4(R_1^2 + R_2^2) + 2R_1 c_1 + 2R_2 c_2} & \text{soft-soft} \end{cases} \tag{8.3}$$

where $\Delta V = M(\frac{1}{\rho_c} - \frac{1}{\rho})$ is the volume overlapping with the boundary A_{total}.

8.2.1 Analysis of the force law

For the analysis of the measurements, the critical volume fraction ρ_c of the soft-particle needs to be determined. When plotting the normal force versus the actual volume fraction of the soft-particle ρ_c, is given by the intersection of the plot with the x-axis. For the measurement in chapter 6 this gives $\rho_c = 0.763$; a value only slightly higher than the initial volume fraction $\rho_i = 0.761$.

Using equation 8.3 to determine δV one gets the force law shown in Figure 8.5 where the normal force is plotted versus δV. The upper two curves show the solid-soft interaction for the size ratio $\frac{1}{1}$ and $\frac{1}{10}$ while the lower two curves show the soft-soft interaction for the size ratio $\frac{1}{1}$ and $\frac{1}{2}$. Unlike in Figure 6.8 which shows the normal force versus the normal deformation, there exists no threshold because as soon as there exists a volume of interaction δV, a repulsive force is measured

For the soft-soft interaction the force law is independent of the size ratio while for the elastic-soft interaction one needs to interpolate between the

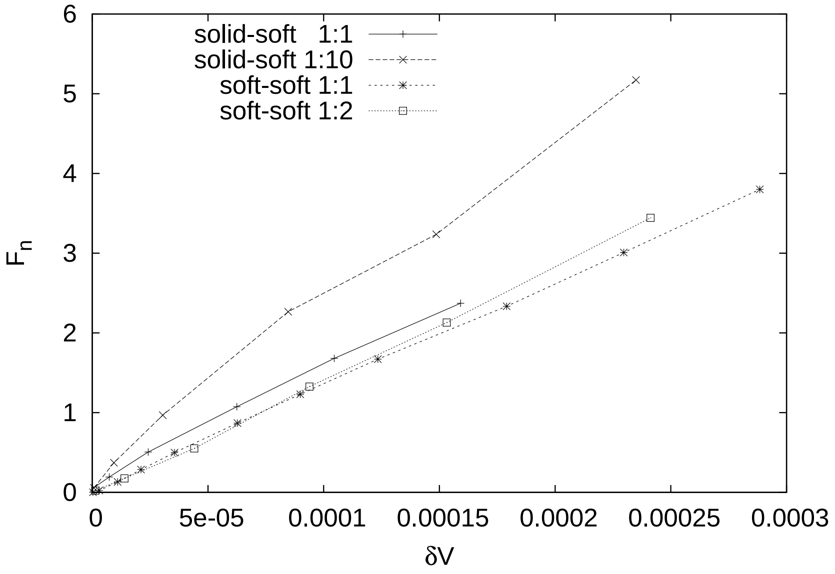

Fig. 8.5: Normal force as a function of the interacting volume δV. The lower two curves show the soft-soft interaction for the size ratios $\frac{1}{1}$ and $\frac{1}{2}$. The upper two show the solid-soft interaction for the size ratio $\frac{1}{1}$ and $\frac{1}{10}$.

two curves to obtain the force law for size ratios different from the measured ones. This can be simplified when δV is calculated only from the upper part in equation 8.3. This takes into account that in the solid-soft interaction a fraction of δV generates tangential forces which cancel out and do not contribute to the normal force. Therefore the bent area A_b can be replaced by the circular area between the two sphere caps. Figure 8.6 shows the resulting curves and in a first approximation one can set the curves for the solid-soft interaction to be identical. This allows an arbitrary shape for the soft-particles and reduces the number of simulations significantly as only two measurements are necessary to determine the force law. Namely the solid-soft and soft-soft interaction with a size ratio $\frac{1}{1}$.

8.3 Implementing the self-consistent soft-par–ticles

To implement the self-consistent soft particles, an algorithm is needed which determines the actual volume fraction and, if it is larger than ρ_c, gives the interaction volume δV.

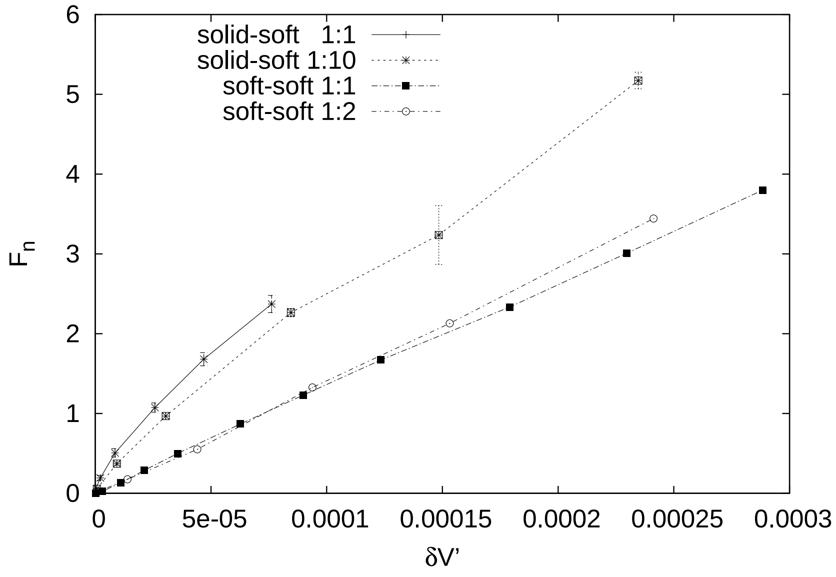

Fig. 8.6: Normal force as a function of the effective overlapping volume δV. The lower two curves, showing the soft-soft interaction are the same as in Figure 8.5.

For two overlapping soft-particles the available space for the polydisperse material is reduced by the volume V_{caps}. Thus the volume fraction of both particles increases. The goal of the following algorithm is to divide the subtracted volume V_{caps} between the two particles, such that the resulting volume fraction of both particles is identical.

As the molecular dynamics only works with particle pairs an iterative method, similar to the iterative solver in the contact dynamics, is used. For simplicity the following algorithm is given for spherical soft-particles, but it can be generalized to particles of arbitrary shape.

In each contact the available volume for the polydisperse media is reduced by the overlapping volume V_{caps}. Therefore each particle is assigned a variable V_{cut} which corresponds to the volume occupied by overlapping particles. For the first particle in the contact this is $V_{cut_1} = a_1 V_{caps}$ and similar for the second one $V_{cut_2} = a_2 V_{caps}$. The sum of the assigning factors a_1 and a_2 is unity and the algorithm works like the following:

1. Initialization

   For each contact the assigning factors are set to $a_1 = a_2 = 0.5$ and sweeping over all particles the volume cut from a given particle is calculated via

$$V_{cut} = \sum_{i=0}^{i=n} V_{caps_i} a_i. \tag{8.4}$$

Here n is the number of contacts of the chosen particle, V_{caps_i} is the overlapping volume of the ith contact and a_i the assigning factor.

2. Recalculation of the assigning factors

   Going over all contacts the two assigning factors a_1 and a_2 in every contact are recalculated via

   $$a_{i_{new}} = a_i + \Delta a_i = a_i + \frac{\frac{m_i}{\rho_a} - (V_i - V_{cut_i})}{V_{caps}}, \qquad i = 1, 2. \tag{8.5}$$

   Here V_i is the volume and m_i the mass of the ith particle in the contact while ρ_a is the average volume fraction in the contact and given by

   $$\rho_a = \frac{m_1 + m_2}{V_1 + V_2 - V_{cut_1} - V_{cut_2}}. \tag{8.6}$$

   Thus m_i/ρ_a is the target volume of the particle and $V_i - V_{cut}$ is the momentary available volume. The difference between these two gives the additionally needed volume which, for $\rho_a < \rho_c$, can also be negative and the assigning factor might become smaller than zero. In this case the negative factor is set to zero and the other one to unity.

   Using equation 8.5 the assigning factors might show changes from zero to unity in a single step. This is prevented by allowing a maximum change Δa_{max}. This step width is comparable to the time step in a molecular dynamics and set to $\Delta a_{max} = 0.001$.

   The recalculation is repeated until the assigning factors do not change anymore.

3. Determine δV

   Using the assigning factors determined above, the volume of interaction δV for a single contact is calculated via

   $$\delta V = \frac{V_{caps} a_1}{V_{cut_1}} \underbrace{\left(\frac{m_1}{\rho_c} - (V_1 - V_{cut_1})\right)}_{V_{e1}} + \frac{V_{caps} a_2}{V_{cut_2}} \underbrace{\left(\frac{m_2}{\rho_c} - (V_2 - V_{cut_2})\right)}_{V_{e2}} \tag{8.7}$$

> The underbraced terms are the excess volumes of the first and second particle respectively. This is the volume of the particle at critical volume fraction minus the available volume at its actual volume fraction. It corresponds to the mass overlapping with other particles and is distributed among all overlapping contacts of the particle.

In theory the second step of the iteration needs to be repeated several times per time step which is very time consuming. Comparing simulations with a different number of iterations shows that one iteration per time step is sufficient when the values of a_1 and a_2, calculated previously, are used during the initialization in the first step.

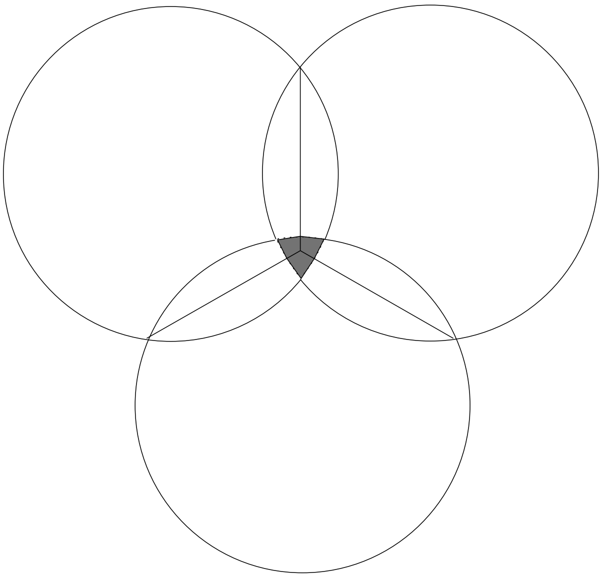

Fig. 8.7: Three interacting soft-particles. The flower like area corresponds to the overlapping volume between the three particles. For the calculation of the actual density only particle pairs are taken into account and the volume which corresponds to the grey area in the picture is subtracted more than once.

Implementing this algorithm an approximation for multi-body contacts is made. Figure 8.7 shows a simple example of three interacting soft-particles. The flower like area corresponds to the overlapping volume between the three particles. With the algorithm above only particle pairs are taken into account, which avoids this complexity but produces a small error when calculating the critical volume fraction as the volume which corresponds to the grey area in the picture is subtracted more than once. Therefore the resulting volume fraction might be larger than its actual value.

8.4 Iteration

Using the self-consistent soft-particles the first two iterations for the model described above were performed. The binning factor was set to $g = 10$ while the initial volume fraction of the inserted soft-particle was set to $\rho_i = 0.35$. Thus the force law of the second iteration corresponds to a system of polydispersity $P = 100$.

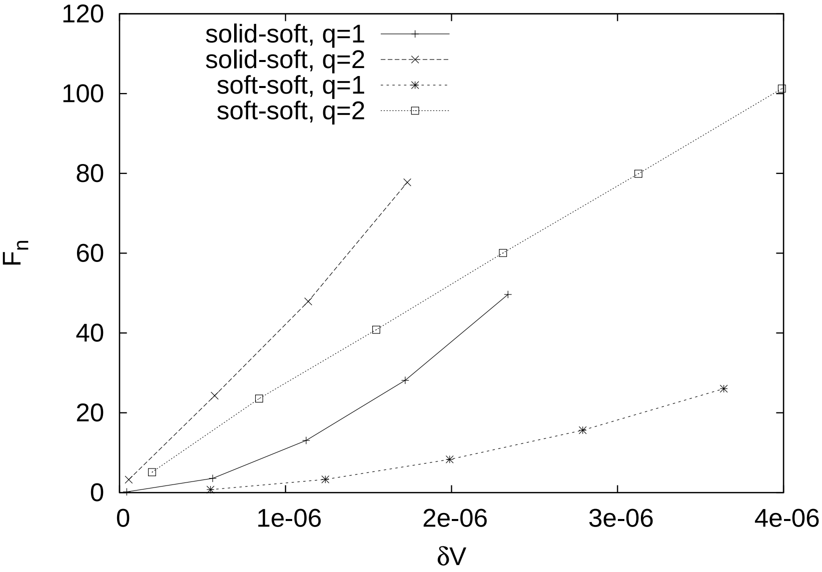

Fig. 8.8: Repulsive force as a function of the overlapping volume δV in the iterative measurement for the solid-soft and soft-soft interaction with a size ratio $\frac{1}{1}$. The measured force law of the second step is stronger than in the first step because, in the second iteration, the voids between the grains are filled with soft-particles which obey the force law of the first iteration.

The resulting force law for the solid-soft and soft-soft interaction with a size ratio $\frac{1}{1}$ is shown in Figure 8.8. The force law of the second step is stronger than in the first step because, in the second iteration, the voids between the grains are filled with soft-particles which obey the force law of the first iteration. The critical volume fraction is $\rho_c \approx 0.65$ in the first iteration and becomes $\rho_c \approx 0.75$.

A third iteration was also performed but due to the approximation during the calculation of δV the critical volume fraction decreases again. We expect that a non spherical implementation of the soft-particle, completely describing the void space between the grains would eliminate the approximation and thus the critical volume fraction will increase from iteration to iteration.

8.5 Conclusion

In this chapter we introduced a self-consistent model which allows the simulation of granular media of any given polydispersity. The force law is determined in an iterative process where each iteration extends the size distribution described by the measured force law. To obtain a force law which is independent of the geometry we introduced a new concept where the polydisperse material filled into the soft-particle is envisioned similar to a fluid; it has a fixed volume and can take arbitrary shape. With this concept the force-law of the soft-particles is described as a function of the volume of interaction δV. It follows that the implementation of the soft-particles is not restricted to a certain size ratio and the spherical shape. Thus only one measurement per contact type is necessary which significantly reduces the simulations during a single iteration. For simplicity the size ratio for the solid-soft and soft-soft interaction was chosen to be $\frac{1}{1}$.

To test the algorithm a simple version with spherical soft-particles was implemented. Performing two iterations we could show that the force law gets stiffer from one iteration to the next. This results from the additional material filled into the voids.

As a summary we can say that the self-consistent model allows to simulate systems of different polydispersity with the same number of particles. Thus it decouples the polydispersity from the number of particles in the simulation.

9

Conclusions

In this thesis we developed fast algorithms to simulate extremely polydisperse granular media where the size distribution is given by a truncated power law. We could show that the biggest constraint for the numerical study of extremely polydisperse systems is given by the non-linear dependence of the computing time on the polydispersity. This is caused by the increase of the number of particles compared with a monodisperse system covering the same volume and the fact that the time step linearly depends on the size of the smallest particle. Additionally the linked-cell algorithm is not suited to determine the interacting particle pairs because for polydisperse media each cell contains, additionally to the large particles, many small ones. Therefore a large number of unnecessary contacts are created which increase the computing time and memory consumption. A solution was given with the quad-tree which generates a finer grid in regions with many small particles while it is coarse around big particles.

In a two dimensional shear experiment and in collaboration with Dr. Distler from BASF the shear behavior of polydisperse media was analyzed. Of special interest was the influence of a lubricant which was modeled with point-like particles. It was shown that the dilatancy increases with the polydispersity and that point-like particles reduce the force necessary to shear the system while the angle of dilatancy and the dilatancy are almost unchanged.

For systems with a polydispersity greater than 10 the simulation of every individual particle becomes numerically too expensive. To reduce the computational costs the concept of the soft-particles was introduced. These soft-particles replace all grains smaller than a certain size with a macroscopically description of a polydisperse packing.

The general normal force law of these particles is, for the solid-soft and soft-soft contact, given by

$$F(\delta_n) = \left\{ \begin{array}{ll} 0, & 0 < \delta_n < \delta'_n \\ \alpha(a_n \delta_n^{b_n} + c_n), & \delta_n \geq \delta'_n \end{array} \right. . \tag{9.1}$$

Here δ_n is the imposed normal deformation, δ'_n is the threshold until which the soft-particle can be deformed before a repulsive force is measured. The variables a_n, b_n and c_n are fit parameters which are different for the two contact types and the factor α scales the measured force law to the scale on which the particles are implemented.

The tangential force law

$$F_t(\delta_n, \delta_t) = F_{t_{max}}(\delta_n) \cdot \tanh(s\delta_t) \tag{9.2}$$

depends on the normal deformation δ_n and the tangential deformation δ_t. Here the parameter s is a constant and

$$F_{t_{max}}(\delta n) = \left\{ \begin{array}{ll} 0, & 0 < \delta n < \delta'_n \\ \alpha(a_t \delta_n^{b_t} + a_t \delta_n'^{b_t}), & \delta_n \geq \delta'_n \end{array} \right. \tag{9.3}$$

is the maximum tangential force the contact can sustain before sliding. As in the normal force law, α is the scaling factor and a_t and b_t are fit parameters. The slope $F_{t_{max}} s$ at zero tangential deformation gives the stiffness of the tangential spring.

To fill the soft-particle with a dense random polydisperse packing the hierarchical algorithm introduced by Tomaso Aste [98] was extended. The size distribution of the generated packing follows a truncated power law and has an exponent $b = 3.5$ which is about the same value observed in real world polydisperse materials.

Using this macroscopic description for particles smaller than a certain size significantly reduces the particles in the simulation. In the shear experiment discussed in chapter 7 the polydispersity could be expanded by a factor of 10 while the number of particles, compared with the simulation without soft-particles, was reduced by a factor 28. Additionally the time step could be chosen five times larger which reduces the overall computation time by more than a factor 100. Still, the dependence of the computation time on the polydispersity remains when the polydispersity is increased.

With the self-consistent extension of the soft-particle the polydispersity of a granular material can be decoupled from the number of particles used in the simulation. The force law is determined in an iterative process where each iteration extends the described size distribution. This way systems of different polydispersity can be simulated while the number of particles in the simulation remains constant. Additionally, describing the force as a function of the interaction volume shows that the implementation of the self-consistent soft-particle is not restricted to a certain shape.

9.1 Outlook

The developed algorithms are an important step to improve the understanding of extremely polydisperse media and their applications. Of great importance is the possibility to simulate any polydisperse media with a finite number of particles which allows the numerical study of different mixing techniques.

This is important for the prediction of the maximal achievable density when mixing a material with a given size distribution. Up to now this is only solved for a monodisperse system. We believe that the proposed algorithm can give an answer to this question when the size distribution follows a truncated power law. As mentioned earlier the creation of high volume fractions is of great interest for the preparation of high performance concrete.

To further extend the capabilities of the self-consistent model we propose the following extensions. As the force-law of the soft-particles only depends on the volume of interaction they do not need to be spherical. Therefore it should be possible to use a meshing algorithm similar to the Voronoi-tessellation [100, 101] to divide the void space between the grains into segments. These segments then replace the small soft-particles which further reduces the number of particles as the number of cells is comparable to the number of grains in the system.

10

Appendix A

10.1 Apollonian insertion

Here we derive a solution for the Apollonian insertion used in section 7.1.1. Wanted is the position and radius of a fifth sphere inserted between four other spheres such that it touches all four. The set of equation to solve is:

$$|\vec{x_i} - \vec{x}| = r_i + r, \qquad i = 1..4 \tag{10.1}$$

Here $\vec{x}$ and r are the position and radius of the new sphere while $\vec{x}_i$ and r_i are the positions and radii of the four already existing spheres.

The upper equation is linearized by subtracting each of the last three equations from the first one:

$$2(\vec{x_i} - \vec{x_j})\vec{x} = r(r_i - r_j) - (\vec{x_j} - \vec{x_i})(\vec{x_j} + \vec{x_i}), \qquad i = 1..4, j = 2..4 \tag{10.2}$$

For all three equations this is:

$$2\underbrace{\begin{pmatrix} x_1-x_2 & y_1-y_2 & z_1-z_2 \\ x_1-x_3 & y_1-y_3 & z_1-z_3 \\ x_1-x_4 & y_1-y_4 & z_1-z_4 \end{pmatrix}}_{A}\begin{pmatrix} x \\ y \\ z \end{pmatrix} = r\begin{pmatrix} r_1-r_2 \\ r_1-r_3 \\ r_1-r_4 \end{pmatrix} - \begin{pmatrix} (\vec{x_2}-\vec{x_1})(\vec{x_2}+\vec{x_1}) \\ (\vec{x_3}-\vec{x_1})(\vec{x_3}+\vec{x_1}) \\ (\vec{x_4}-\vec{x_1})(\vec{x_4}+\vec{x_1}) \end{pmatrix}$$

Inverting the matrix A on the left hand side one gets the coordinate of the new sphere

$$\vec{x} = A^{-1}\begin{pmatrix} r_1-r_2 \\ r_1-r_3 \\ r_1-r_4 \end{pmatrix} r - A^{-1}\begin{pmatrix} (\vec{x_2}-\vec{x_1})(\vec{x_2}+\vec{x_1}) \\ (\vec{x_3}-\vec{x_1})(\vec{x_3}+\vec{x_1}) \\ (\vec{x_4}-\vec{x_1})(\vec{x_4}+\vec{x_1}) \end{pmatrix}. \tag{10.3}$$

Inserting this into equation 10.1 one gets a quadratic equation for the radius

$$r^2 + br + c = 0. \tag{10.4}$$

If one of the resulting radii is negative the positive radius is the wanted one. If both results are positive then the smaller one is the solution as the larger radius corresponds to the sphere enclosing the other four.

10.2 Calculating V_s

In this section we derive V_s used in section 8.1.1. It describes how much volume during the initialization must be filled with soft-particles to obtain a self-consistent packing following the size distribution in Figure 8.2. When the largest radius is set to $r_{max} = 1$ and, as in the infinite case, the smallest radius to $r_{min} = 0$, the ratio between the summed volume of the first interval and the summed volume of all particles in the size distribution is given by

$$\theta = \frac{\int_{1/g}^{1} \frac{4}{3}\pi r^3 p(r) dr}{\int_0^1 \frac{4}{3}\pi r^3 p(r) dr} = 1 - g^{b-4}. \tag{10.5}$$

For the following discussion one has to distinguish between the summed volume V_s of the soft-particles inserted into our self-consistent soft-particle and the volume V_S of the soft-particle itself. When the summed volume of the grains inserted into the soft-particles is called V_g one can write for the total mass inside the soft-particle:

$$M_t = V_g \rho_g + V_s \rho_s. \tag{10.6}$$

Here ρ_g and ρ_s are the volume fractions of the grains and the soft-particles respectively. Using the fact that self-consistency implies that ρ_s is the same for all soft-particles and defining the total occupied volume inside a soft-particles by $V_t = V_g + V_s$ we can write:

$$\rho_s = \frac{M_t}{V_S} = \frac{V_g \rho_g + (V_t - V_g)\rho_s}{V_S} \tag{10.7}$$

As $\rho_g = 1$ we get

$$\rho_s = \frac{V_g}{V_S - (V_t - V_g)} \tag{10.8}$$

Using the ratio $\theta = 1 - g^{b-4}$ calculated in equation 10.5 the volume of the grains is

$$V_g = \theta V_S \rho_s. \tag{10.9}$$

Subtracting the volume of the grains from the total volume one gets

$$V_s = V_t - V_g = V_S(1 - \theta) = V_S g^{b-4}. \tag{10.10}$$

10.3 Calculating δV

Here the derivation of the interaction volume δV between two particles, as it is used in section 8.3, is explained. Figure 10.1 shows the setup of these two particles.

The intersecting volume V_{caps} of the two spheres is the sum of the two sphere caps defined by the overlap $\delta_n = c_1 + c_2$ and is given by [102]

$$V_{caps} = \frac{\pi(R_1 + R_2 - d)^2(d^2 + 2dR_1 - 3R_1^2 + 2dR_2 + 6rR_2 - 3R_2^2)}{12d}. \tag{10.11}$$

R_1 is the radius of the first particle, R_2 the radius of the second one and $d = R_1 + R_1 - \delta_n$ is the distance between the sphere centers. Thus, for $\delta_n > 0$ the volume ΔV, which is the difference between the volume of the soft-particle at critical volume fraction and the available volume at the present overlap, is given by

$$\Delta V = \frac{M}{\rho_c} - (\frac{4}{3}\pi R_1^3 - V_{caps}). \tag{10.12}$$

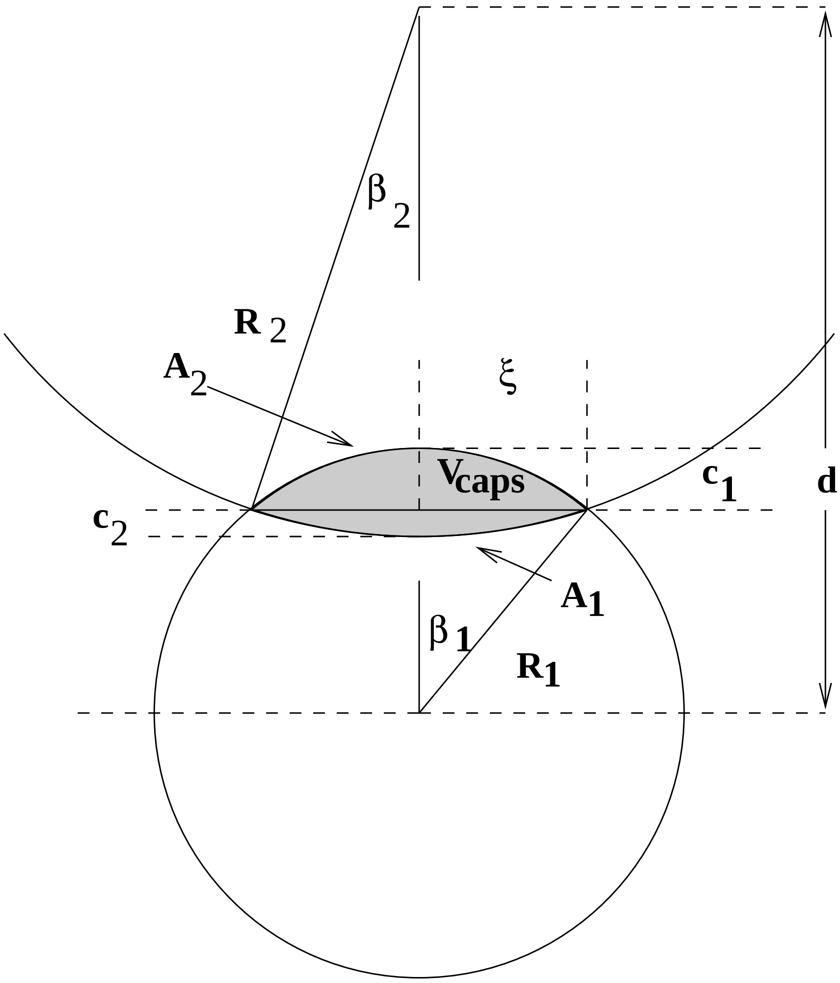

Fig. 10.1: Geometrical sketch of the measurement. Here R_1 is the radius of the first particle, c_1 the height of its sphere cap and ξ the radius of the circular area between the two sphere caps defined by the normal deformation $\delta_n = c_1 + c_2$. The area of the first sphere inside the second sphere is denoted A_1.

Here M is the mass of all particles inserted into the soft-particle and ρ_c is the critical volume fraction. The boundary A_{total} for the solid-soft and the soft-soft interaction is given by

$$A_{total} = \begin{cases} 4\pi R_1^2 - A_1 + A_2 = 2\pi(2R_1^2 - R_1 c_1 + R_2 c_2) & \text{solid-soft} \\ 4\pi(R_1^2 + R_2^2) - (A_1 + A_2) = 2\pi(2(R_1^2 + R_2^2) + R_1 c_1 + R_2 c_2)) & \text{soft-soft} \end{cases}, \tag{10.13}$$

where A_1 and A_2 are given by

$$A_i = 2\pi R_i^2(1 - \cos(\beta_i)) = 2\pi R_i^2(1 - \frac{R_i - c_i}{R_i}) = 2\pi R_i c_i, \qquad i = 1, 2. \tag{10.14}$$

The surface of interaction A_b in the solid-soft contact is $A_1 = 2\pi R_1 c_1$

while for the soft-soft interaction it is the circular area $\pi\xi^2$ between the two sphere caps with $\xi^2 = R_i^2 - (R_i - c_i)^2$.

Thus the overlapping volume is given by

$$\delta V = \begin{cases} \Delta V \frac{R_1 c_1}{2R_1^2 - R_1 c_1 + R_2 c_2} & \text{solid-soft} \\ \Delta V \frac{2R_1 c_1 - c_1^2}{4(R_1^2 + R_2^2) + 2R_1 c_1 + 2R_2 c_2} & \text{soft-soft} \end{cases} \tag{10.15}$$

Bibliography

[1] G. Sauermann, P. Rognon, A. Poliakov, and H.J. Herrmann. The shape of the barchan dunes of Southern Morocco. *Geomorphology*, 36:47–62, 2000.

[2] K. Kroy, G. Sauermann, and H.J. Herrmann. Minimal Model for Sand Dunes. *Physical Review Letters*, 88(5):54301, 2002.

[3] V. Schwämmle and H.J. Herrmann. A Model of Barchan Dunes Including Lateral Shear Stress. *The European Physical Journal E*, 16:57–65, 2005.

[4] O. Durán, V. Schwämmle, and H.J. Herrmann. Breeding and Solitary Wave Behavior of Dunes. *Physical Review E*, 72:21308, 2005.

[5] A.R. Lima, G. Sauermann, H.J. Herrmann, and K. Kroy. Modelling a dune field. *Physica A*, 310:487–500, 2002.

[6] G.D. Scott and D.M. Kilgour. The density of random close packings of spheres. *Brit. J. Appl. Phys. (J. Phys. D)*, 2:863, 1969.

[7] T. Aste and D. Weaire. *The Pursuit Of Perfect Packing*. IoP:Bristol, 2000.

[8] R. Mahmoodi Baram and H.J. Herrmann. Self-Similar Space-Filling Packings in three dimensions. *Fractals*, 12(3):293–301, 2004.

[9] H.J. Herrmann, G. Mantica, and D. Bessis. Space-filling bearings. *Physical Review Letters*, 65(26):3223–3226.

[10] G. Oron and H.J. Herrmann. Generalization of space-filling bearings to arbitrary loop size. *J. Phys. A*, 33:1417–1434.

[11] M. Borkovec, W. de Paris, and R. Peikert. The fractal dimension of the apollonian sphere packing. *Fractals*, 2(4):521–526, 1994.

[12] J.J. Moreau. *Lecture Notes in Applied and Computational Mechanics*. 2004.

[13] F. Radjai and L. Brendel. Nonsmoothness, indeterminacy, and friction in two-dimensional arrays of rigid particles. *Physical Review E*, 54(1):861–873, 1996.

[14] F. Radjai, M. Jean, J.-J. Moreau, and S. Roux. Force Distribution in Dense Two-Dimensional Granular Systems. *Physical Review Letters*, 77(2):274–277, 1996.

[15] T. Unger and J. Kertész. The Contact Dynamics Method for Granular Media. *AIP Conference Proceedings*, 661(1):116–138, 2003.

[16] J. J. Moreau. *Eur. J. Mech. A-Solids*, 13:93–114.

[17] M. Jean. *Comput. Methods Appl. Mech. Engrg.*, 177:235–257.

[18] D.C. Rapaport. *The art of molecular dynamics simulation*. Oxford University Press, 1989.

[19] M.P.Allen and D.J.Tildesley. *Computer Simulation of Liquids*. Oxford University Press, 1987.

[20] J.A. McCammon and S.C. Harvey. *Dynamics of proteins and nucleic acids*. Cambridge University Press, 1987.

[21] P.A. Cundall and O.D.L. Strack. A discrete numerical model for granular assemblies. *Geotechnique*, 29(1):47–65, 1979.

[22] S.Luding. Stress distribution in static two-dimensional granular model media in the absence of friction. *Physical Review E*, 55(4):4720–4729, 1997.

[23] B.J. Ennis, J. Green, and R. Davis. *Particle Technology*, 90:32.

[24] T.M. Knowlton, J.W. Carson, G.E. Klinzing, and W.-C. Yang. *Particle technology*, 90:44.

[25] O. Reynolds. On the dilatancy of media composed of rigid particles in contact. *Philo. Mag.*, 20:469, 1885.

[26] J.S. Chong, E. B. Christiansen, and A. D. Baer. Rheology of Concentrated Suspensions. *Journal of Applied Polymerical Science*, 15:2007–2021, 1971.

[27] Philippe Gondert and Luc Petit. Dynamic viscosity of macroscopic suspensions of bimodal sized solid spheres. *Journal of Rheology*, 41(6):1261–1274, 1997.

[28] Richard L. Hoffman. Factors affecting the viscosity of unimodal and multimodal colloidal dispersions. *Journal of Rheology*, 36(5):947–965, 1992.

[29] R. J. Farris. Prediction of the Viscosity of Multimodal Suspensions from Unimodal Viscosity Data. *Transactions of the society of Rheology*, 12(2):281–301, 1968.

[30] M. Z. Sengun and R. F. Probstein. Bimodal Model of Slurry Viscosity with Application to Coal-Slurries. Part 1. Theory and Experiment. *Rheol. Acta*, 28:382–393, 1989.

[31] C.A. Coulomb. Essai sur une application des regles de maximis et minimis a quelques problemes de statique, relatifs a l'architecture. volume 7 of *Memoires de Mathematique &de Pyhsique*, page 343. 1776.

[32] J. Krim. Surface science and the atomic scale origins of friction: what once was old is new again. *Surface science*, 500:741–758, 2002.

[33] J. Krim. Friction at the atomic scale. *Scientific American*, 275:74–80, 1996.

[34] H. M. Jaeger and Sidney R. Nagel. Physics of the Granlar State. *Science*, 255(5051):1523–1531.

[35] H.M. Jaeger, S.R. Nagel, and R.P. Behringer. Granular solids, liquids, and gases. *Reviews of Modern Physics*, 68(4):1259–1273.

[36] H.J. Herrmann. Die wunderbare Welt der Schüttgüter. *Physikalische Blaetter*, 51(11):1083.

[37] In T. Pöschel and S. Luding, editors, *Granular Gases*, volume 564 of *Lectures Notes in Physics*. Springer-Verlag, Berlin, 2001.

[38] In T. Pöschel and N.V. Brilliantov, editors, *Granular Gas Dynamics*, volume 624 of *Lectures Notes in Physics*. Springer-Verlag, Berlin, 2003.

[39] A. Kudrolli, M. Wolpert, and J.P. Gollub. Cluster Formation due to Collisions in Granular Material. *Physical Review Letters*, 78(7):1383–1386.

[40] É. Falcon, R. Wunenburger, P. Évesque, S. Fauve, C. Chabot, Y. Garrabos, and D. Beysens. Cluster Formation in a Granular Medium Fluidized by Vibrations in Low Gravity. *Physical Review Letters*, 83(2):440–443.

[41] F. Rouyer and N. Menon. Velocity Fluctuations in a Homogeneous 2D Granular Gas in Steady State. *Physical Review Letters*, 85(17):3676–3679.

[42] W. Losert, D.G.W. Cooper, J. Delour, A. Kudrolli, and J.P. Gollub. Velocity statistics in excited granular media. *Chaos*, 9(3):682–690.

[43] S. Luding, E. Clément, J. Rajchenbach, and J. Duran. Simulations of pattern formation in vibrated granular media. *Europhys. Lett.*, 36(4):247.252.

[44] C. Bizon, M.D. Shattuck, J.B. Swift, W.D. McCormick, and H.L. Swinney. Patterns in 3D Vertically Oscillated Granular Layers: Simulation and Experiment. *Physical Review Letters*, 80(1):57–60.

[45] D.C. Hong, P.V. Quinn, and S. Luding. Reverse Brazil Nut Problem: Competition between Percolation and Condensation. *Physical Review Letters*, 86(15):3423–3426, 2000.

[46] A. Rosato, K.J. Strandburg, F. Prinz, and R.H. Swendsen. Why the Brazil Nuts are on Top: Size Segregation of Particlate Matter by Shaking. *Physical Review Letters*, 58(10):1038–1041.

[47] J.A.C. Gallas, H.J. Herrmann, T. Pöschel, and S. Sokolowski. Molecular dynamics simulation of size segregation in three dimensions. *J. Stat. Phys.*, 82(1-2):443–450.

[48] H. A. Janssen. Versuche über Getreidedruck in Silozellen. *Zeitschrift des Vereins deutscher Ingenieure*, pages 1045–1049.

[49] R. Bagnold. Experiments on a gravity-free dispersion of large solid spheres in a newtonian fluid under shear. *Proc. Royal Soc. London A*, 225:49–63, 1954.

[50] Y. Grasselli and H.J. Herrmann. On the angles of dry granular heaps. *Physica A*, 246:301–312, 1997.

[51] H.M. Jaeger, C. Liu, and S.R. Nagel. Relaxation at the Angle of Repose. *Physical Review Letters*, 62:40, 1989.

[52] J.J. Alonso, J.-P. Hovi, and H.J. Herrmann. Model for the calculation of the angle of repose from the microscopic grain properies. *Physical Review E*, 58:672, 1998.

[53] V. Buchholtz and T. Pöschel. Numerical investigations of the evolution of sandpiles. *Physica A*, 202:390, 1994.

[54] J. Gasterstädt. *Die experimentelle Untersuchung des pneumatischen Fördervorgangs*, volume 265. VDI Verlag, 1924.

[55] W. Cramp and A. Priestley. Pneumatic grain elevators. *Engineer*, 137:34–36,64–65,89–90, 1924.

[56] M. Strauß. *Untersuchung der Pfropfendynamik und -stabilität bei der vertikalen und horizontalen Pfropfenförderung*. PhD thesis, 2005.

[57] S. Roux, A. Hansen, H.J. Herrmann, and J.-P. Vilotte. A model for gouge deformation: Implications for remanent magnetization. *Geophys. Res. Letters*, 20(14):1499–1502.

[58] C. Lomnitz. *Bull. Seismol. Soc. Am.*, 72:1441.

[59] L. Sykes, W. McCann, S. Nishenko, and J. Krause. *Pure Appl. Geophys.*, 117:1082.

[60] J.A. Åström, H.J. Herrmann, and J. Timonen. Granular Packings and Fault Zones. *Physical Review Letters*, 84(4):638–641.

[61] R. Mahmoodi Baram, H.J. Herrmann, and N. Rivier. Space-Filling Bearings in Three Dimensions. *Physical Review Letters*, 92:44301–1, 2004.

[62] R. Mahmoodi Baram and H.J. Herrmann. Random Bearings and Their Stability. *Physical Review Letters*, 95:224303, 2005.

[63] H.J. Herrmann, J.A. Åström, and R. Mahmoodi Baram. Rotations in Shear Bands and Polydisperse Packings. *Physica A*, 344:516–522, 2004.

[64] H.J. Herrmann, R. Mahmoodi Baram, and M. Wackenhut. Searching for The Perfect Packing. *Physica A*, 330:77–82, 2003.

[65] H.J. Herrmann, R. Mahmoodi Baram, and M. Wackenhut. Polydisperse packings. *Brazilian Journal of Physics*, 33:591, 2003.

[66] R. Mahmoodi Baram, M. Wackenhut, and H.J. Herrmann. The art of packing densely. In *Proceedings of the International Conference on Statistical Physics of Complex Fluids*.

[67] D.E. Wolf. Modeling and computer simulation of granular media. In K.H. Hoffmann and M. Schreiber, editors, *Computational Physics*, pages 64–94. Springer, Berlin, 1996.

[68] S. McNamara and W. R. Young. Inelastic collapse in two dimensions. *Physical Review E*, 50(1):R28–R31.

[69] A. Rényi. On an one-dimensional random space-filling problem. *Publ. Math. Res. Inst. Hung. Acad. Sci.*, 3:109–127, 1958.

[70] I. Palásti. On some random space filling problems. *Publ. Math. Res. Inst. Hung. Acad. Sci.*, 5:353–360, 1960.

[71] P.L. Krapivsky and E. Ben-Naim. Collective properties of adsorption-desorption processes. *J. Chem. Phys.*, 100(9):6778–6782, 1993.

[72] Mathew D. Penrose. Random Parking, Sequential Adsorption, and the Jamming Limit. *Communications in Mathematical Physics*, 218(1):153–176, 2001.

[73] E. G. Coffmann Jr., L. Flatto, P. Jelenković, and B. Poonen. Packing Random Intervals On-Line. *Algorithmica*, 22(4):448–476, 1998.

[74] A. J. Kolan, E. R. Nowak, and A. V. Tkachenko. Glassy Behavior of the Parking Lot Model. *Physical Review E*, 59(3):3094–3099, 1999.

[75] E. Ben-Naim, J. B. Knight, R. R. Nowak, H. M. Jaeger, and S. R. Nagel. *Physica D*, 123:3094, 1998.

[76] J. Talbot, G. Tarjus, and P. Viot. *J. Phys. A*, 32:2997, 1999.

[77] J. Talbot, G. Tarjus, and P. Viot. Adsorption-desorption model and its application to vibrated granular materials. *Physical Review E*, 61(5):5429–5438, 2000.

[78] M. Wackenhut and H.J. Herrmann. The Reversible polydisperse parking lot model. *Physical Review E*, 68:041303 1–7, 2003.

[79] M. Wackenhut. Modeling of compaction of polydisperse particles. Master's thesis, 2002.

[80] H. Hertz. Über die Berührung fester elastischer Körper. *J. reine angewandte Mathematik*, 92:156–171, 1882.

[81] L.D. Landau and E.M. Lifschitz. *Elastizitätstheorie*, volume 265. Akademie Verlag Dresden, Berlin, 1989.

[82] Stefan Luding. *Die Physik kohäsionsloser granularer Medien*. Logos Verlag, Berlin, 1997.

[83] Y. Tsuji, T. Tanaka, and T. Ishida. Lagrangian numerical simulation of plug flow of cohesionless particles in a horizontal pipe. *Powder Technology*, 71:239–250, 1992.

[84] R.D. Mindlin. *Appl. Mech. Trans. ASME*, 16:259, 1949.

[85] R.D. Mindlin and H. Deresiewicz. *Appl. Mech. Trans. ASME*, 20:327, 1953.

[86] W.C. Swope and H.C. Andersen. A computer simulation method for the calculation of equilibrium constants for the formation of physical clusters of molecules: application to small water clusters. *J. Chem. Phys.*, 76(1):637–649, 1982.

[87] J. Moreau and P. Panagiotopoulos. *Nonsmooth Mechanis and Applications*. Springer, Vienna, 1988.

[88] B. Miller, C. O'Hern, and R. P. Behringer. Stress Fluctuations for Continuously Sheared Granular Materials. *Physical Review Letters*, 77(15):3110–3113, 1996.

[89] D.W. Howell and R.P. Behringer. Fluctuations in granular media. *Chaos*, 9(3):559–572, 1999.

[90] M. Wackenhut, S. McNamara, and H.J. Herrmann. Shearing behavior of polydisperse media. *The European Physical Journal E - Soft Matter*, 17:237–246, 2005.

[91] G.C. Barker and M.J. Grimson. Sequential random close packing of binary disc mixtures. *J. Phys. Condens. Matter*, 1:2779–2789.

[92] W.M. Visscher and M. Bolsterli. Random packing of equal and unequal spheres in two and three dimensions. *Nature*, 239:540.

[93] N.V. Brilliantov, Y.A. Andrienko, and P.L. Krapivsky. Pattern-Formation by growing droplets: The touch and stop model of growth. *J. Stat. Phys.*, 75(3-4):507–523.

[94] N.V. Brilliantov, P.L. Krapivsky, and Yu. A. Andrienko. Random space-filling-tiling: fractal properties and kinetics. *J. Phys. A*, 27:L381–L386.

[95] P.S. Dodds and J.S. Weitz. Packing-limited growth. *Physical Review E*, 65(5):56108– 1–6.

[96] E.L. Hinrichsen, J. Feder, and T. Jøssang. Geometry of random sequential adsorption. *J. Stat. Phys.*, 44(5-6):793–827.

[97] Z.P. Zhang, A.B. Yu, and R.B.S. Oakeshott. Effect of packing method on the randomness of disc packings. *J. Phys. A*, 29:2671–2685, 1996.

[98] T. Aste. Circle, sphere and drop packings. *Physical Review E*, 53(3):2571–2580, 1996.

[99] HJ Tillemans and H.J. Herrmann. Simulation deformations of granular solids under shear. *Physica A*, 217:261–288, 1995.

[100] G.L. Dirichlet. Über die Reduktion der positiven quadratischen Formen mit drei unbestimmten ganzen Zahlen. *Journal für die Reine und Angewandte Mathematik*, 40:209–227, 1850.

[101] G. Voronoi. Nouvelles applications des paramètres continus à la théorie des formes quadratiques. *Journal für die Reine und Angewandte Mathematik*, 133:97–178, 1908.

[102] Eric W. Weisstein. Sphere-sphere intersection. *From MathWorld–A Wolfram Web Resource*.

Acknowledgment

I thank Prof. Herrmann for giving me the opportunity to work on this challenging subject at his institute and Prof. Trebin for being the secondary supervisor.

Special thanks goes to my girlfriend Jessica who always supported me in the last years.

I am also very grateful to my colleagues and I especially thank Sean with whom I worked on the BASF project and Jens for very helpful discussions and the right questions at the right time. I also thank Martin Strauß and Reza Mahmoodi for their company and the good times we had throughout our time at the institute.

I also want to thank all my room mates in the Bauhäusle for all the good times.